

# **Ultrafast spectroscopy and control of correlated quantum materials**

By

Bryan T. Fichera

B.S., University of Pennsylvania (2017)

Submitted to the Department of Physics  
in partial fulfillment of the requirements for the degree of

Doctor of Philosophy

at the

MASSACHUSETTS INSTITUTE OF TECHNOLOGY

May 2024

©Bryan Thomas Fichera, 2024. All rights reserved.

The author hereby grants to MIT a nonexclusive, worldwide, irrevocable, royalty-free license to exercise any and all rights under copyright, including to reproduce, preserve, distribute and publicly display copies of the thesis, or release the thesis under an open-access license.

Authored by: Bryan T. Fichera  
Department of Physics  
May 10, 2024

Certified by: Nuh Gedik  
Donner Professor of Physics, Thesis supervisor

Accepted by: Lindley Winslow  
Associate Department Head of Physics



# **Ultrafast spectroscopy and control of correlated quantum materials**

By

Bryan T. Fichera

Submitted to the Department of Physics  
on May 10, 2024 in Partial Fulfillment of the Requirements for the Degree  
of Doctor of Philosophy

## **Abstract**

In this thesis, I describe research completed during my Ph.D. on correlated condensed matter systems using ultrafast optics. I begin with a broad overview of this field, focusing specifically on the essential physics involved in ultrafast processes and how that physics may be utilized, in the sense of either spectroscopy or control, to understand correlated systems. I then give a pedagogical introduction to second harmonic generation, both in theory and in practice, before describing results from four projects I completed in my Ph.D.—(i) a technical project concerned with automating polarization rotation in second harmonic generation, (ii), a demonstration that second harmonic generation may be used to differentiate charge density wave domains with opposite planar chirality, (iii) our discovery of an ultrafast reorientation transition in the antiferromagnetic semiconductor  $\text{CaMn}_2\text{Bi}_2$ , and (iv) second harmonic generation evidence for an amplitude-mode electromagnon in  $\text{CuBr}_2$ . I conclude by reflecting on the progress achieved in correlated electron physics as a result of this work, and by giving my own perspective on the future of this field.

Thesis supervisor: Nuh Gedik

Title: Donner Professor of Physics

## Acknowledgements

I owe a huge debt to my advisor, Nuh Gedik, for all of his support throughout my Ph.D. Not only is Nuh a brilliant scientist, he is also extremely kind to his students, demonstrating a level of compassion far beyond, I think, what is typical for Ph.D. advisors in Physics. None of the research in this thesis would have been possible without that.

I would also like to thank my undergraduate advisor, Jay Kikkawa, as well as Sebastian Hurtado Parra and Mehmet Noyan, who were graduate students in his group when I was there. These were the one of the first people in my career who decided to believe in me (based on what, I don't know), and for that I am extremely grateful. They are also all excellent experimentalists; almost everything I know about doing research came from them.

Many thanks also to Joe Checkelsky and Liang Fu, who served on my committee and who I enjoyed chatting with during my Ph.D. I am also grateful for the support of my academic advisor, Pablo Jarillo-Herrero.

Anshul Kogar was a postdoc in the Gedik group when I joined in 2017, and took me under his wing when as I was building the initial experimental setup. Anshul worked with me to tackle the many, many bugs in the setup—something that I think many postdocs would have left me to do on my own—and somehow kept an extremely chill disposition throughout the whole process. He was also very kind to me when I was facing some health issues during my first and second years, which I am very grateful for.

Baiqing Lv joined the Gedik group a few years later, and was my officemate and mentor from then until he left in 2022. Baiqing and I worked jointly on almost all of the projects in this thesis, and he and I spent many hours discussing different interpretations for our results before we landed on the ones presented here. More importantly, though, Baiqing was and is an excellent friend.

Karna Morey and Zongqi Shen, two very perspicacious young people, joined the Gedik group at different times when I was a senior Ph.D. student and, like Anshul and Baiqing, helped me a lot with all of the projects presented in this thesis. Without Karna, we would not have had the ability to automate the polarizers in the experimental setup, which

was indisputably necessary for the  $\text{CaMn}_2\text{Bi}_2$  and  $\text{CuBr}_2$  projects. He and Zongqi were also responsible for taking much of the data for these projects when I was travelling or otherwise away from the lab. After Karna graduated, Zongqi joined the lab as a graduate student and has been working closely with me since then; in that time, he has not only learned all of the ins and outs of the experimental setup, but also launched a number of new projects which I am very excited to see pan out. I am grateful to both of them not only for their help completing this research, but also for the opportunity to be their mentors, and for their patience as I learned how to do that.

I am also grateful to the rest of the Gedik group for all of their support during my Ph.D; it was truly a pleasure to come to an office every day that was filled with such amazing people, and to be able to enjoy their company throughout the day. At many times they showed me kindness that they didn't need to—from helping me with experiments to taking me to the hospital when I broke my foot—which had a much greater impact than I think they know.

Thanks also to Monica Wolf, Gerry Miller, and Lars Llorente, who were essential in keeping CMX functional at MIT, and to Mike Maikowsky, for fixing our Spitfire many more times than should have been necessary.

To Mom, Dad, Alison, Dylan, Gladys, and Jytte, thank you for instilling in me a love for science, supporting my dreams, and for encouraging me to be the best version of myself that I can be. Thanks also to Antonella, Ari, Bernie, Julius, Lisa, and Marc for all of your support and for welcoming me into your family.

No amount of thanks is adequate for all of my friends, especially Will, Cliff, Kalina, Hope, Abe, Jeff, and Rachel; I have no right to have so many amazing people in my life, but I do, and I'm very grateful for you.

Thank you to all of the workers who make life in Boston possible, especially the employees at Chipotle, Life Alive, and all the other killer lunch spots near the office, the custodial and facilities staffs at MIT, the employees at MIT Medical, and the workers and delivery drivers at the various restaurants around town that I would often get dinner from.

Finally, to Cami: thank you for coming with me on this wonderful adventure, for celebrating all of the smallest achievements with me, and for carrying me at times when I couldn't go any further on my own. It has meant the world to me, and I only hope I can look out for you the same way you have for me.



---

## *Contents*

<b>Contents</b>	vii
<b>List of Figures</b>	xi
<b>List of Tables</b>	xiii
<b>1 Ultrafast optics in correlated electron systems</b>	15
1.1 Spectroscopy . . . . .	17
1.1.1 Collective modes . . . . .	17
1.1.2 Coherent oscillations . . . . .	18
1.1.3 Excitation mechanisms . . . . .	20
1.1.3.1 In absorption . . . . .	20
1.1.3.2 In transparency . . . . .	21
1.1.4 Collective modes in correlated materials . . . . .	24
1.1.4.1 Phase transitions and Goldstone's theorem	24
1.1.4.2 Example: electromagnons in multiferroics	26
1.2 Control . . . . .	29
1.2.1 Incoherent control . . . . .	30
1.2.1.1 Heating across a phase transition . . . . .	30
1.2.1.2 Nonthermal melting . . . . .	30
1.2.1.3 Formal model: time-dependent Ginzburg-Landau theory . . . . .	31
1.2.1.4 Dynamics following an ultrafast quench . . . . .	32
1.2.2 Coherent control . . . . .	34
1.2.2.1 Via coherent oscillations . . . . .	34
1.2.2.2 Via Floquet engineering . . . . .	35
1.2.3 Control as spectroscopy . . . . .	36
<b>2 Second harmonic generation: theory</b>	39

2.1	Space groups, point groups, and Neumann's principle . . . . .	39
2.2	A classical understanding of SHG . . . . .	43
2.3	SHG in quantum mechanics . . . . .	45
2.4	SHG in the Ginzburg-Landau paradigm . . . . .	48
<b>3</b>	<b>Second harmonic generation: practical</b> . . . . .	<b>51</b>
3.1	Description of the setup . . . . .	51
3.2	Before you build . . . . .	54
3.2.1	Spot size . . . . .	54
3.2.2	Oblique vs. normal incidence . . . . .	55
3.2.3	Choice of detector . . . . .	56
3.3	tr-SHG: methodology . . . . .	57
3.3.0.1	Polarization control . . . . .	57
3.3.0.2	The pump beam path . . . . .	57
3.4	Data analysis . . . . .	58
3.4.1	Static RA-SHG patterns . . . . .	59
3.4.2	Modeling $\chi_{ijk}$ : the simplified bond hyperpolarizability model . . . . .	62
3.4.3	Fitting time traces in tr-SHG . . . . .	63
<b>4</b>	<b>Automated polarization rotation for multi-axis RA-SHG experiments</b> . . . . .	<b>67</b>
4.1	Preface . . . . .	67
4.2	Abstract . . . . .	67
4.3	Introduction . . . . .	68
4.4	Design . . . . .	72
4.4.1	Slip Ring . . . . .	73
4.4.2	Miniature Stepper Motor . . . . .	73
4.5	Validation and Discussion . . . . .	76
<b>5</b>	<b>Second harmonic generation as a probe of broken mirror symmetry in 1T-TaS<sub>2</sub></b> . . . . .	<b>79</b>
5.1	Preface . . . . .	79
5.2	Abstract . . . . .	79
5.3	Introduction . . . . .	80
5.4	Results and discussion . . . . .	83
5.5	Conclusion . . . . .	88
5.6	Acknowledgments . . . . .	90

5.7	Supplemental material . . . . .	90
5.7.1	Probing broken mirror symmetry with RA-SHG . . . . .	90
5.7.1.1	Complete RA-SHG data . . . . .	90
5.7.1.2	$\mathcal{I}_{PS}^{(3)}$ as an indicator of broken mirror symmetry . . . . .	91
5.7.2	Physical importance of the $P_{in}$ - $S_{out}$ channel . . . . .	95
5.7.3	Generalization to other mirror symmetry-breaking transitions . . . . .	98
5.7.4	Probing the sense of planar chirality with RA-SHG . . . . .	99
5.7.4.1	Complete RA-SHG data . . . . .	99
5.7.4.2	Electron diffraction confirming the sample is single domain . . . . .	99
5.7.4.3	Fitting RA-SHG data in the $\alpha$ and $\beta$ configurations . . . . .	99
5.7.5	Bulk broken mirror symmetry in 1T-TaS <sub>2</sub> . . . . .	101
5.7.5.1	Complete RA-SHG data at $T = 295K$ . . . . .	101
5.7.5.2	Symmetry analysis of RA-SHG data . . . . .	101
5.7.6	Methods . . . . .	105
6	Light-induced reorientation transition in the antiferromagnetic semiconductor CaMn <sub>2</sub> Bi <sub>2</sub> . . . . .	107
6.1	Preface . . . . .	107
6.2	Abstract . . . . .	107
6.3	Introduction . . . . .	108
6.4	Results . . . . .	109
6.4.1	Equilibrium . . . . .	109
6.4.2	Nonequilibrium . . . . .	114
6.5	Discussion . . . . .	116
6.6	Conclusion . . . . .	119
6.7	Methods . . . . .	119
6.7.1	Material growth . . . . .	119
6.7.2	Tr-SHG measurements . . . . .	119
6.7.3	PTMB measurements . . . . .	120
6.7.4	XRD measurements . . . . .	121
6.7.5	Data availability . . . . .	121
6.8	Acknowledgments . . . . .	121
6.9	Author contributions . . . . .	122
6.10	Supplementary Material . . . . .	122

6.10.1	Supporting theoretical discussion . . . . .	122
6.10.1.1	Equilibrium strain-spin coupling . . . . .	122
6.10.1.2	Laser-induced dynamics of competing magnetic domains: “incoherent” scenario . . . . .	124
6.10.1.3	Laser-induced dynamics of competing magnetic domains: “coherent” scenario . . . . .	125
6.10.2	Nonviability of secondary order parameter in describing the rotational anisotropy second harmonic generation (RA-SHG) data . . . . .	128
6.10.3	Fits to susceptibility tensors . . . . .	130
6.10.4	Error bar estimation for Fig. 6.11 . . . . .	133
7	Amplitude-mode electromagnon in the spin-spiral multiferroic CuBr <sub>2</sub>	145
7.1	Preface . . . . .	145
7.2	Abstract . . . . .	145
7.3	Introduction . . . . .	146
7.4	Results . . . . .	148
7.4.1	Equilibrium . . . . .	148
7.4.2	Nonequilibrium . . . . .	150
7.5	Discussion . . . . .	154
7.6	Conclusion . . . . .	155
7.7	Methods . . . . .	155
7.8	Supplementary material . . . . .	156
7.8.1	Electromagnons in CuBr <sub>2</sub> . . . . .	156
7.8.2	Energy of the pseudo-Goldstone mode . . . . .	157
7.8.3	Fits of time domain signals . . . . .	157
7.8.4	Error bars in Fig. 7.4 . . . . .	158
7.8.5	Fits to static RASHG data . . . . .	160
7.8.6	Excluded possibilities for observed results . . . . .	160
7.8.6.1	$\delta\vec{P}  \hat{x}$ oscillation . . . . .	160
7.8.6.2	Zone-folded acoustic phonons . . . . .	161
7.8.6.3	Magnetic SHG . . . . .	162
7.8.6.4	Multi-phason excitation . . . . .	163
8	Concluding remarks	165
	Bibliography	169

---

## *List of Figures*

1.1 Schematic free energy density in the GL model. . . . .	24
3.1 Schematic drawing of the SHG setup used in this research. . . . .	52
3.2 Photograph of the SHG setup. . . . .	53
4.1 A demonstration of RA-SHG in the test sample GaAs . . . . .	70
4.2 A diagram of the full second harmonic generation setup . . . . .	72
4.3 Exploded-view diagram of one of the automated polarization rotators . . . . .	74
4.4 A 3-dimensional rendering of the automated polarization rotators	76
4.5 Demonstration of the automatic polarization rotators . . . . .	77
5.1 Structure of 1T-TaS <sub>2</sub> and schematic of the SHG setup . . . . .	82
5.2 SHG in 1T-TaS <sub>2</sub> above and below $T_{\text{IC-NC}}$ . . . . .	84
5.3 SHG in NC-TaS <sub>2</sub> . . . . .	85
5.4 RA-SHG in the $S_{\text{in}}S_{\text{out}}$ polarization channel in 1T-TaS <sub>2</sub> . . . . .	89
5.5 RA-SHG of 1T-TaS <sub>2</sub> : all polarization channels . . . . .	91
5.6 Intuition for mirror symmetry breaking in SHG . . . . .	96
5.7 RA-SHG in the $\alpha$ and $\beta$ phases of 1T-TaS <sub>2</sub> . . . . .	100
5.8 Electron diffraction of 1T-TaS <sub>2</sub> . . . . .	103
5.9 Electric quadrupole RA-SHG in 1T-TaS <sub>2</sub> ( $T = 295$ K) . . . . .	104
5.10 Electric quadrupole RA-SHG in 1T-TaS <sub>2</sub> ( $T = 356$ K) . . . . .	104
6.1 Crystal structure of CaMn <sub>2</sub> Bi <sub>2</sub> and temperature dependence of SHG . . . . .	110
6.2 Equilibrium domain distribution in CaMn <sub>2</sub> Bi <sub>2</sub> . . . . .	112
6.3 Tr-SHG of CaMn <sub>2</sub> Bi <sub>2</sub> . . . . .	115
6.4 Illustration of our theoretical understanding of CaMn <sub>2</sub> Bi <sub>2</sub> . . . . .	117
6.5 Energy difference between $x$ and $y$ -directions with respect to the easy axis . . . . .	123

---

6.6 Phonon mode and AFM order parameter following photo-excitation with coupling $(L_1^2 + L_2^2)(Q + Q^2)$ . . . . .	127
6.7 Phonon mode and AFM order parameter following photo-excitation with coupling $L_1 L_2 e_2 Q$ . . . . .	128
6.8 Fits to the RA-SHG pattern in the four domains of Fig. 6.2 2.0 ps before ( $A, B, C, D$ ) and $\sim 40$ ps after ( $A', B', C', D'$ ) zero delay . . . . .	132
6.9 RA-SHG results of Fig. 6.11 depicted with estimated errorbars (see text). . . . .	133
6.10 Comparison of quench times in different domains . . . . .	135
6.11 Fluence dependence of $\text{CaMn}_2\text{Bi}_2$ . . . . .	136
6.12 Pump-probe spectroscopy of $\text{CaMn}_2\text{Bi}_2$ . . . . .	137
6.13 X-ray diffraction of $\text{CaMn}_2\text{Bi}_2$ . . . . .	138
6.14 RA-SHG results of Fig. 6.1 depicted in all four polarization channels ( $P_{\text{in}}P_{\text{out}}, P_{\text{in}}S_{\text{out}}, S_{\text{in}}P_{\text{out}}$ , and $S_{\text{in}}S_{\text{out}}$ ) . . . . .	138
6.15 Full equilibrium RA-SHG results in $\text{CaMn}_2\text{Bi}_2$ . . . . .	139
6.16 Full nonequilibrium tr-SHG results in $\text{CaMn}_2\text{Bi}_2$ . . . . .	140
6.17 Polarization dependence of tr-SHG results . . . . .	141
6.18 Transition of $\text{CaMn}_2\text{Bi}_2$ to the state opposite of that presented in the main text . . . . .	142
6.19 Transition of $\text{CaMn}_2\text{Bi}_2$ to state opposite of that presented in the main text, at long times . . . . .	143
6.20 SHG intensity in the same domain as Fig. 6.2(f) as a function of temperature . . . . .	144
7.1 Electromagnons in $\text{CuBr}_2$ . . . . .	147
7.2 SHG in $\text{CuBr}_2$ : temperature dependence . . . . .	149
7.3 tr-SHG in $\text{CuBr}_2$ . . . . .	150
7.4 Frequency of coherent oscillations in $\text{CuBr}_2$ . . . . .	152
7.5 Time-domain signals for temperature dependence of collective oscillation frequencies in $\text{CuBr}_2$ . . . . .	158
7.6 Rescaled time-domain signals in $\text{CuBr}_2$ . . . . .	159
7.7 Time-domain signals in $\text{CuBr}_2$ fit without mode softening . . . . .	160
7.8 Fits to static SHG signal in $\text{CuBr}_2$ . . . . .	161
7.9 DFT calculation of acoustic phonons in $\text{CuBr}_2$ . . . . .	162

---

*List of Tables*

3.1	Vector definition of polarization channels. . . . .	60
5.1	Indicators of broken mirror symmetry in RA-SHG . . . . .	97
6.1	Subgroups obtained by the onset of magnetic order of a given irreducible representation . . . . .	126



# Chapter 1

---

## *Ultrafast optics in correlated electron systems*

Interactions between electrons in solids can be treated broadly in two different ways, depending on the strength of the interaction. Let us start with the case where the interactions are weak compared to their kinetic energy. In this case, interactions may be treated as a perturbation

$$V = \sum_{\vec{p}\vec{p}'\vec{q},\sigma\sigma'} V(\vec{q}) c_{\vec{p}+\vec{q},\sigma}^\dagger c_{\vec{p}'-\vec{q},\sigma'}^\dagger c_{\vec{p}',\sigma'} c_{\vec{p},\sigma} \quad (1.1)$$

on top of the usual hamiltonian

$$H_0 = \epsilon_{\vec{p}} c_{\vec{p},\sigma}^\dagger c_{\vec{p},\sigma} \quad (1.2)$$

for the noninteracting electrons. The key insight, due conceptually to [? ] and later formalized by [? ], is that, as long as the interactions are sufficiently weak, this problem can be adiabatically connected to a similar problem with non-interacting quasiparticles. Since these quasiparticles are fermions, they obey the Pauli exclusion principle, and the phase space available for scattering low-energy excitations thus goes to zero at small energies. By Fermi's golden rule, the lifetime of such particles thus approaches infinity as we get closer and closer to the Fermi surface; i.e., there are still well-defined quasiparticles there. Such a system is hence referred as a “Fermi liquid,” to signify the fact that we have made only a slight departure from the nominal model of a Fermi gas where the particles are treated as noninteracting.

Fermi liquid theory is unreasonably successful in describing the ground state of correlated electron systems. Truly *most* metals can be very adequately described as a simple Fermi gas with renormalized effective mass, specific heat, etc.; while these modifications may be large (e.g.  $m^*/m \approx 10^3$  in CeAl<sub>3</sub>), they otherwise look like normal metals. Nevertheless, we can discuss circumstances in which the theory fails. Clearly various electronic

instabilities may gap out the Fermi surface, resulting in an insulator; this happens for arbitrarily weak interactions in quasi-1D systems due to the Peierls mechanism, and in higher dimensions due to, e.g., Fermi surface nesting. Whether the interaction is attractive or repulsive determines whether the instability occurs in the charge or the spin channel. In the other limit, where the kinetic energy hamiltonian 1.2 is treated as a perturbation to the interaction term 1.1, the Fermi liquid state gives way to an (Mott, or Wigner) insulating state where the electrons become localized so as to minimize the coulomb repulsion  $U$ .

Studying such departures from Fermi liquid theory has become one of the most important fields in condensed matter physics. It is usually referred to as “strongly correlated electron physics”, but many of the instabilities mentioned above are present even in the limit of weak interactions. Much of this interest was spurred by the discovery in 1986 by [? ] of high- $T_c$  superconductivity in  $\text{Ba}_x\text{La}_{5-x}\text{Cu}_5\text{O}_{5(3-y)}$ , although the field has grown to include many other phenomena which occur in the strongly interacting limit that may or may not be related to superconductivity. Despite nearly four decades of research, however, there still exists no universal theory for strongly correlated electron systems, in the sense that, if someone hands you a random strongly correlated material, it is impossible from the outset to *predict* its ground state or its low-energy excitations. In fact, it is not even clear such a theory ought to exist[? ].

The *field* of strongly correlated physics is thus, in some sense, still very much in its infancy, although that’s not to say there haven’t been huge advances, both theoretically and experimentally, especially since the discovery by [? ]. A lot of the effort experimentally has been focused on cataloguing the huge number of different exotic ordered phases—charge density wave, spin density wave, superconducting, strange metals, spin liquids, pseudogap, etc.—that are realized in these systems. Usually this is done by mapping out a *phase diagram* for each given material, which indicates which phases are present at various values of external parameters (magnetic field, pressure, strain, etc). Ultrafast optics has played an important role in this respect, as it allows one to add a *nonequilibrium* axis to such phase diagrams. Such experiments, for example, have not only helped illustrate the extent to which different phases compete with one another in the cuprate phase diagram, but also the extent to which the action of the light pulse in strongly correlated materials can be used to tune the properties of those materials for practical purposes. This is

paradigm is referred to as “ultrafast control,” and I will discuss it in more detail in Section 1.2.

A parallel effort in the field of ultrafast optics is to use the pump not to control the state of the material, but rather to excite coherent oscillations of the low-energy collective modes and study these oscillations in the time domain. This approach is advantageous for two reasons. For one, the frequencies accessible with this technique are bounded from below only by the length of one’s delay stage, in contrast to conventional spectrometer-based methods which involve finite-frequency filters and gratings. Second of all, the ability to select both the excitation mechanism (the pump) and the measurement apparatus (the probe) allows one to design experiments that target specific degrees of freedom of interest. Thus, for example, in multiferroics, one can use second harmonic generation (SHG) to selectively probe the collective modes which modulate the macroscopic polarization. This direction is referred to as “ultrafast spectroscopy,” which I will explain in detail in Section 1.1.

This chapter may thus be regarded as an introduction to ultrafast optics, with special emphasis on how we can use ultrafast experiments to understand correlated materials without having to consider the interaction terms explicitly. A complete review of this material is beyond the scope of this thesis; instead, I will focus on a few seminal works that I think tell this story most pedagogically. Where appropriate, I point to pedagogical references that may be more useful than this thesis for these and other concepts.

## 1.1 Spectroscopy

### 1.1.1 Collective modes

The low-energy excitations of any many-body system are typically *collective*, in the sense that they involve motion of all of the particles in the system rather than just one. Let us consider, for example, the classical model consisting of two identical coupled harmonic oscillators

$$H = \sum_{i=1}^2 \left( \frac{p_i^2}{2m} + \frac{m\omega_0^2}{2} x_i^2 \right) + gx_1x_2, \quad (1.3)$$

with mass  $m$ , natural frequency  $\omega_0$ , and coupling constant  $g$ . When  $g = 0$ , the normal modes of this system are simply the independent oscillation modes of the two oscillators. However, for any nonzero  $g$ , the normal modes involve either symmetric or antisymmetric linear combinations of the two oscillator coordinates; that is, they involve collective motion of the two oscillators. The extension to an ensemble of harmonic oscillators is straightforward; there, too, the normal modes of the Hamiltonian involve collective motion of all of the coordinates at once.

Of course the solids that we are interested in are more complicated than a simple ensemble of harmonic oscillators. Usually, though, more complicated systems can be broken down into a small number of *subsystems* which may, as a first approximation, be treated separately. Thus, for example, it makes sense to refer to the phonon subsystem independently from the electronic subsystem, with different and independent collective mode spectra in the limit where the inter-subsystem coupling goes to zero.

When this coupling is nonzero, however, many interesting phenomena may occur. For example, spin-orbit coupling—which implies a coupling between spin and orbital degrees of freedom of the electron—can, in the right circumstances, cause the statically ordered state of the spin subsystem to also induce a ferroelectric distortion of the electron orbitals. The normal modes of the system in the presence of this coupling are no longer pure magnon or orbital modes, but rather collective modes of the spin and orbital degrees of freedom together. Let us look at this phenomenon from a different perspective. Suppose we didn't know the ground state of the system, but we did know that the relevant low-energy excitations involved both spin and orbital degrees of freedom (for example, we might see a response in both the time-resolved Kerr rotation as well as the time-resolved SHG (tr-SHG)). This is good evidence that the ground state of the system involves this coupling to some extent. Thus, we have learned something quite important about our system without doing anything but look at the low-energy collective excitations.

### **1.1.2 Coherent oscillations**

Clearly understanding the low-energy excitations corresponding to a given ground state is a useful way to understand its properties. So far, however, we have made no mention of how to *probe* these excitations in

pump-probe spectroscopy. Let us consider the following Hamiltonian consisting of electrons  $c_{\vec{k}\sigma}$  (with dispersion  $\epsilon_{\vec{k}\sigma}$ ) and bosons  $b_{\vec{q}}$  (with dispersion  $\omega_{\vec{q}}$ ) interacting via some potential  $V_{\vec{k}\vec{q}}^{\sigma}$

$$H = \sum_{\vec{k}\sigma} \epsilon_{\vec{k}\sigma} c_{\vec{k}\sigma}^\dagger c_{\vec{k}\sigma} + \sum_{\vec{q}} \hbar\omega_{\vec{q}} b_{\vec{q}}^\dagger b_{\vec{q}} + \sum_{\sigma \vec{k}\vec{q}} V_{\vec{k}\vec{q}}^{\sigma} \left( b_{\vec{q}} + b_{-\vec{q}}^\dagger \right) c_{\vec{k}\sigma}^\dagger c_{\vec{k}+\vec{q}\sigma}. \quad (1.4)$$

The average lattice displacement is given by

$$\langle u(\vec{r}) \rangle \propto \sum_{\vec{q}} \left( \langle b_{\vec{q}} \rangle e^{i\vec{q} \cdot \vec{r}} + \langle b_{\vec{q}}^\dagger \rangle e^{-i\vec{q} \cdot \vec{r}} \right). \quad (1.5)$$

Clearly, in order for us to have a macroscopic lattice displacement, we need to have a finite value for  $\langle b_{\vec{q}} \rangle$  and  $\langle b_{\vec{q}}^\dagger \rangle$ , which is impossible if there are a definite number of phonons in the mode  $\vec{q}$  (since  $\langle n | b_{\vec{q}} | m \rangle = 0$  for  $n = m$ ). In contrast, if the wavefunction of the system consists of a coherent superposition of different phonon occupation numbers,  $\langle u(\vec{r}) \rangle$  may acquire a finite value. One thematic example of such a wavefunction is the so-called “coherent state” of the quantum harmonic oscillator

$$|\alpha_{\vec{q}}\rangle = \sum_n \frac{\alpha^n e^{-z^2/2}}{n!} (b_{\vec{q}}^\dagger)^n |0\rangle, \quad (1.6)$$

although the real wavefunction need not be fully coherent to have a nonzero average lattice displacement.

One can show (see [1]) that the equation of motion for the operator  $D_{\vec{q}} \equiv \langle b_{\vec{q}} \rangle + \langle b_{-\vec{q}}^\dagger \rangle$  due to Eq. 1.4 is

$$\frac{\partial^2}{\partial t^2} D_{\vec{q}} + \omega_{\vec{q}}^2 D_{\vec{q}} = -2\omega_{\vec{q}} \sum_{\vec{k}\sigma} V_{\vec{k}\vec{q}}^{\sigma} \langle c_{\vec{k}\sigma}^\dagger c_{\vec{k}+\vec{q}\sigma} \rangle, \quad (1.7)$$

i.e.,  $D_{\vec{q}}$  obeys a second-order differential equation with an inhomogeneous part related (in this case) to the electronic subsystem.<sup>1</sup> Thus, if we manage to initialize a wavefunction with a finite  $D_{\vec{q}}$ , the frequency with which  $D_{\vec{q}}$  oscillates in time is the frequency  $\omega_{\vec{q}}$  of the boson  $b_{\vec{q}}$ .

---

<sup>1</sup>There will also be a damping term, which may be added phenomenologically but is otherwise not considered in this treatment.

The central idea in ultrafast spectroscopy is therefore to excite coherent modes like Eq. 1.6, and then measure the frequency, damping, etc. of these modes by measuring  $D_{\vec{q}}$ . This is in contrast to equilibrium spectroscopies, which measure, for example, the transfer of energy from the light field to states with a definite number of bosons (i.e.,  $|n\rangle \rightarrow |n+1\rangle$ ). In theory, of course, the information obtained is the same—the frequency and damping coefficient of the collective modes in question may readily be obtained in the equilibrium spectroscopies as well as in the pump-probe scheme. However, as I argued at the start of this chapter, the pump-probe techniques offer a number of advantages, most notably (i) the ability to design the pump and the probe to specify exactly which excitations we would like to measure, and (ii) the ability to measure much lower frequencies than in conventional spectroscopy due to the energy being measured in the time domain, rather than the frequency domain.

### 1.1.3 Excitation mechanisms

The next question is: how do we intend to excite these coherent oscillations in real materials? The truth is there are many such mechanisms; however, we can start by placing them into two generic categories. *Impulsive* mechanisms involve using the light pulse to apply an effective force to the relevant degrees of freedom in the material, which lasts for the duration of the light pulse; i.e., it is a delta function in time. *Displacive* mechanisms are, in contrast, typically a step function; i.e., the equilibrium position of the oscillator is different before and after the light pulse. One important experimental difference is that impulsive excitation results in a coordinate  $D_{\vec{q}}(t) \propto \sin(\omega t)$ , whereas displacive excitation results in  $D_{\vec{q}}(t) \propto \cos(\omega t)$ ; this can be seen simply by solving

$$\frac{\partial^2}{\partial t^2} D_{\vec{q}} + \omega_{\vec{q}}^2 D_{\vec{q}} = f(t) \quad (1.8)$$

for  $f(t) \propto \delta(t)$  or  $f(t) \propto \theta(t)$ , respectively.

#### 1.1.3.1 In absorption

Let us consider the Hamiltonian in Eq. 1.4. We saw that this Hamiltonian resulted in an equation of motion given by Eq. 1.7, which is a differential

equation for  $D_{\vec{q}}$  with an inhomogenous part

$$f(t) = -2\omega_{\vec{q}} \sum_{\vec{k}\sigma} V_{\vec{k}\vec{q}}^\sigma \langle c_{\vec{k}\sigma}^\dagger c_{\vec{k}+\vec{q}\sigma} \rangle, \quad (1.9)$$

where the time-dependence of the right hand side is complicated but may be phonemnologically modeled. For example, let us suppose that we are in a semiconductor and that photon energy of our pump pulse is greater than the band gap of the material. Thus, the action of the pump is to excite electrons from the valence band into the conduction band. On a very fast timescale (0.1–10 fs) these electrons thermalize with themselves via electron-electron scattering, resulting in a quasi-equilibrium carrier distribution in which electrons and holes have settled at the bottom of the conduction band and the top of the valence band, respectively. Since further decay of these excitations is gapped, the relaxation of this state back to equilibrium may be much longer than the pulse width, especially if the gap is indirect; thus, together with the assumption that the lattice dynamics happen on much longer timescales than the electron thermalization time, it is appropriate to model the force term in Eq. 1.9 as a step function in time

$$f(t) \propto \begin{cases} 0 & t < 0 \\ 1 & t \geq 0 \end{cases}. \quad (1.10)$$

Thus we have the generic result that above-gap excitation typically excites coherent oscillations *displacively*. In the case that the bosons of Eq. 1.4 are phonons, this is known as displacive excitation of coherent phonons (DECP), and was studied by many authors, notably [?]. An important insight which follows from Eq. 1.9 is that, in the limit where the quasi-equilibrium electron distribution doesn't break any symmetries of the original hamiltonian, the applied force also does not break any symmetries. Thus only totally-symmetric phonons may be excited via DECP.

### 1.1.3.2 In transparency

While the DECP-like mechanisms tend to dominate when the photon energy is above the band gap, they are forbidden in transparency. In this case, the dominant excitation mechanism is usually impulsive. To see this, let us consider the case of a collective mode with energy  $\hbar\omega_0$  which we

wish to excite coherently with a below-gap ultrafast laser pulse. If the central frequency of the light pulse is resonant with the collective mode (i.e., we have  $\nu_{\text{photon}} = \hbar\omega_0$ ), then we may drive the coherent oscillation directly; i.e., the mode coordinate  $Q$  simply follows the electric field. This is of course only possible if the mode carries a finite dipole moment (i.e. it is odd under parity). Alternatively, we will see that, under the right conditions, we can also excite coherent oscillation of low-energy collective modes even if the photon energy is far away from any direct resonance.

To see this, recall that ultrafast laser pulses always have a nonzero bandwidth, proportional to the inverse of the pulse width. In a nonlinear optical effect known as difference frequency generation (DFG), pairs of these frequencies may *interfere* to produce electric field components at the difference frequency between the two members of the pair. Thus, as long as the collective mode in question has a frequency less than approximately the bandwidth  $\delta\nu_{\text{photon}}$  of the incident light pulse, there will exist pairs of frequencies  $(\omega_1, \omega_2)$  in that light pulse such that  $|\omega_1 - \omega_2| \approx \omega_0$ . This electric field will last for the duration of the light pulse, which may be treated as a delta function in time. This phenomenon is referred to as impulsive stimulated raman scattering (ISRS).

Since the force is a delta function in time, the result indeed is an impulsive excitation where the coordinate  $D_Q(t) \sim \sin(\omega_0 t)$ . Unlike the direct excitation mechanism mentioned above, ISRS requires two photons and the force is thus even under parity; i.e., we can only excite even-parity bosons.

It is instructive at this point to consider ISRS in a phenomenological Ginzburg-Landau (GL) model. We start by writing down an effective free energy[?]

$$F = -\chi_{ij} E_i(t) E_j(t) Q \quad (1.11)$$

where  $\vec{E}(t)$  is the incident electric field,  $Q$  the mode coordinate,<sup>2</sup> and  $\chi_{ij}$  is some tensor of coefficients (see Chapter 2). The effective force  $f$  due to Eq. 1.11 is

$$f = -\frac{\partial F}{\partial Q} \quad (1.12)$$

$$= \chi_{ij} E_i(t) E_j(t) \quad (1.13)$$

---

<sup>2</sup>Here we treat the mode  $Q$  as nondegenerate, although the generalization to the degenerate case is straightforward.

which appears on the right hand side of Eq. 1.8. Clearly, if the  $\vec{E}(t)$  has Fourier components  $\omega_1$  and  $\omega_2$  such that  $|\omega_1 - \omega_2| \approx \omega_0$ , then the force will be *resonant* with the oscillator frequency.

Some interesting insights may be made in light of Eq. 1.11. Let us consider for example the limit where the “mode”  $Q$  is a static magnetization  $M_k$ . The free energy reads[? ]

$$F = -\chi_{ijk} E_i(t) E_j(t) M_k, \quad (1.14)$$

where we have expanded  $\chi_{ij}$  to linear order in  $\vec{M}$ . Then, there is an *effective magnetic field*

$$H_k^{\text{eff}} = \frac{\partial F}{\partial M_k} \quad (1.15)$$

$$= \chi_{ijk} E_i(t) E_j(t) \quad (1.16)$$

which exists for the duration of the pump pulse. This is the inverse Faraday effect (IFE), which may thus be thought of as a particular limit of ISRS.<sup>3</sup> A similar effect (known as the inverse Cotton-Mouton effect (ICME)) is also present; expanding  $\chi_{ij}$  to second order in  $\vec{M}$ , we have

$$F = -\chi_{ijkl} E_i(t) E_j(t) M_k M_l \quad (1.17)$$

and

$$H_l^{\text{eff}} = \frac{\partial F}{\partial M_l} \quad (1.18)$$

$$= \chi_{ijkl} E_i(t) E_j(t) M_k, \quad (1.19)$$

which, in contrast to the IFE, may occur when the pump is linearly polarized. The ICME is also available in antiferromagnetics (AFMs); writing

$$F = -\chi_{ijkl} E_i(t) E_j(t) L_k L_l, \quad (1.20)$$

where  $\vec{L}$  is the Néel vector (defined as the difference in sublattice magnetizations), we have

$$H_l^{\text{eff}} = \frac{\partial F}{\partial L_l} \quad (1.21)$$

$$= \chi_{ijkl} E_i(t) E_j(t) L_k. \quad (1.22)$$

---

<sup>3</sup>Despite the similarities presented here, the two effects are actually quite different. For example, the spectral content of the pump pulse in the IFE does not change before and after interacting with the sample[? ].

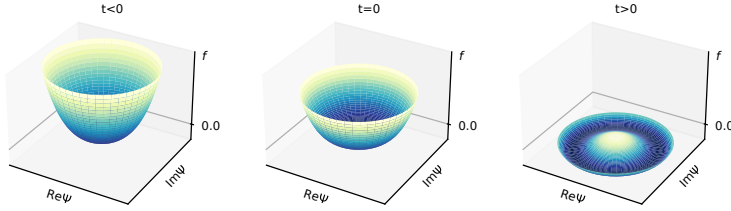


Figure 1.1: Schematic free energy density in the GL model.

A full treatment of these and related effects is beyond the scope of this work;<sup>4</sup> the point is just to draw a connection between the various impulsive excitation mechanisms available to us in ultrafast spectroscopy.

### 1.1.4 Collective modes in correlated materials

#### 1.1.4.1 Phase transitions and Goldstone's theorem

In this section we illustrate one way we can understand the low-energy collective modes of a given material system without knowing precisely the form of the interaction Hamiltonian in Eq. 1.1. The important insight is that we can simply write down all of the *symmetry-allowed* terms in the Hamiltonian (or, at nonzero temperature, the free energy), and examine fluctuations near a phase transition where some order parameter takes on a nonzero value. In doing so, we find quite generally Goldstone's result that there is a gapless collective mode at the  $\Gamma$  point for each spontaneously broken symmetry. We also see that, in addition to the gapless Goldstone bosons, we also get a gapped *amplitude* mode which may be measurable in certain circumstances. The goal of this section is not to give a rigorous proof of Goldstone's theorem, but to illustrate how it comes about in a very simple model.

Let us consider the GL free energy density in the case of superfluidity, which is a functional of the coarse-grained order parameter  $\Psi(\vec{x}) \equiv \psi(\vec{x})e^{i\theta(\vec{x})}$  and whose lowest-order terms are

$$f[\Psi(\vec{x})] = -\frac{t}{2}|\Psi(\vec{x})|^2 + \frac{u}{4}|\Psi(\vec{x})|^4 + \frac{K}{2}|\nabla\Psi(\vec{x})|^2, \quad (1.23)$$

where  $u, K > 0$  and  $t = (T_c - T)/T_c$ . Clearly at all temperatures the minimum of Eq. 1.23 is spatially uniform, but for  $T < T_c$  it occurs at a

---

<sup>4</sup>See [ ] for a comprehensive review.

finite value of  $\psi(\vec{x})$  (see Fig. 1.1)

$$\Psi(\vec{x}) = \bar{\psi} \equiv \sqrt{\frac{t}{u}}, \quad (1.24)$$

where we have (without loss of generality) set  $\bar{\theta} = 0$ . Now consider fluctuations  $\delta\theta(\vec{x})$  in the phase of the order parameter  $\Psi$ . We have

$$f[\bar{\psi}e^{i\delta\theta}] = f[\bar{\psi}] + \frac{K\bar{\psi}^2}{2}|\nabla\delta\theta(\vec{x})|^2, \quad (1.25)$$

where we have used that  $-t + u\bar{\psi}^2 = 0$ . Let us write the fluctuation  $\delta\theta(\vec{x})$  in terms of its Fourier transform

$$\delta\theta(\vec{x}) = \sum_{\vec{q}} e^{i\vec{q}\cdot\vec{x}}\delta\theta_{\vec{q}}. \quad (1.26)$$

Then we have

$$F[\bar{\psi}e^{i\delta\theta(\vec{x})}] \equiv \int f[\bar{\psi}e^{i\delta\theta(\vec{x})}] d^3x = F[\bar{\psi}] + \frac{KV\bar{\psi}^2}{2} \sum_{\vec{q}} q^2 |\delta\theta_{\vec{q}}|^2. \quad (1.27)$$

Thus, uniform ( $\vec{q} = 0$ ) fluctuations in the phase of  $\Psi$  cost zero energy, and long-wavelength ( $\vec{q} \approx 0$ ) fluctuations in the phase of  $\Psi$  cost very little energy. The collective modes corresponding to these long-wavelength fluctuations are exactly our Goldstone modes.

Let us also examine the energy cost of fluctuations in the amplitude of  $\Psi$ , i.e.  $\delta\psi(\vec{x}) \equiv \psi(\vec{x}) - \bar{\psi}$ . To order  $\delta\psi^2$ , we have

$$f[\bar{\psi} + \delta\psi(\vec{x})] = f[\bar{\psi}] - \frac{t}{2}\delta\psi(\vec{x})^2 + \frac{3u\bar{\psi}^2}{2}\delta\psi(\vec{x})^2 + \frac{K}{2}(\nabla\delta\psi(\vec{x}))^2, \quad (1.28)$$

and, inserting  $\bar{\psi} = \sqrt{\frac{t}{u}}$ ,

$$f[\bar{\psi} + \delta\psi(\vec{x})] = f[\bar{\psi}] + \frac{t}{2}\delta\psi(\vec{x})^2 + \frac{K}{2}(\nabla\delta\psi(\vec{x}))^2, \quad (1.29)$$

so that (for  $T < T_c$ ), even *uniform* fluctuations in the amplitude of  $\Psi$  cost nonzero energy. The collective mode associated with such uniform fluctuations is the so-called “amplitude” or “Higgs” mode of our ordered

superfluid, with the important result that the energy of this mode approaches zero for  $T \rightarrow T_c$ .

Observing the amplitude mode in real systems is challenging because its decay into the lower-energy Goldstone modes is not typically forbidden, and so its lifetime is usually too low to observe it as a true quasiparticle[? ]. Nevertheless, amplitude modes have been observed in a number of different circumstances; mainly, of course, in superconductors, where the amplitude mode may appear as a Raman peak in the  $A_{1g}$  channel[? ], but also in charge density wave[? ] and magnetic[? ? ] systems (see [? ] for a good review).

#### 1.1.4.2 Example: electromagnons in multiferroics

In the above we have described how coherent oscillations of collective modes in solids may be excited with an ultrafast laser, and we have explored how we can understand what those modes are without having to solve the full many-body Hamiltonian. Let us start to apply this machinery to a relevant physical system. A full accounting of the different collective modes in correlated systems is beyond the scope of this work; instead, let us focus on a particular class of physical system—multiferroics—which encompasses a lot of the physics of correlated materials and may also be described well in terms of the GL theory we outlined above. Chapter 7 is concerned with one member of this class ( $\text{CuBr}_2$ ); in this material, we have evidence that the amplitude mode of the magnetic Hamiltonian is imprinted on the charge degrees of freedom in the form of an electromagnon. The understanding developed here will thus be quite helpful when we encounter that chapter.

Multiferroics are materials in which magnetic order exists in the same phase as ferroelectric order. They may typically be classified into two types. In the so-called type-II multiferroics, the transition to the ferroelectric state appears at the same temperature as a concomitant magnetic transition. This is because the ferroelectricity is *due to* some inversion symmetry breaking of the magnetic order, for instance by a helical spin density wave.<sup>5</sup> The microscopic mechanism will be discussed shortly, but let us contrast this with the case of type-I multiferroics—in type-I multiferroics, the magnetic and ferroelectric transition temperatures are

---

<sup>5</sup>The ferroelectricity is thus considered of the “improper” type.

different, and neither is “due” to the other; they just happen to exist in the same material. Intuitively this may happen when magnetic ions exist alongside different ions which participate in the ferroelectricity; this is the case in  $\text{BiFeO}_3$ [? ]. Here we will focus on type-II multiferroics, not only because they tend to be more interesting but also because they usually have larger magnetoelectric effects (since the ferroelectric order is due to the magnetic order) and have thus been the central focus of the modern research on multiferroics.

The central question is then: can we describe (microscopically) how ferroelectricity may appear as a *result* of long-range magnetic order? A critical insight due to [?] is that type-II multiferroicity can happen in quasi-1D Mott insulators when spin-orbit coupling is strong and the spins are ordered in a *magnetic spiral*. [?] consider a 3-site 1D cluster model in which two transition metal ions with local spin-orbit coupled  $d$  electron orbitals interact via superexchange across an intermediate ligand atom (with an associated set of  $p$  orbitals). The tendency towards magnetic ordering is put in by hand, by placing a local spin at each transition metal site  $j$  in the direction  $\hat{e}_j = (\cos \phi_j \sin \theta_j, \sin \phi_j \sin \theta_j, \cos \theta_j)$ , and letting the  $d$  spins  $\vec{S}_j$  interact with these local spins via a Hamiltonian  $H_U = -U \sum_j \hat{e}_j \cdot \vec{S}_j$ . They find quite generally the following geometrical relation between the spin directions  $\hat{e}_j$  and an *induced* polarization  $\vec{P}$ :

$$\vec{P} \propto \hat{e}_{12} \times (\hat{e}_1 \times \hat{e}_2) \quad (1.30)$$

where  $\hat{e}_{12}$  is the unit vector parallel to the bond connecting the two transition metal sites.

Clearly if  $\hat{e}_1$  and  $\hat{e}_2$  are either parallel or anti-parallel to one another, there is no induced polarization. However, if the magnetic order is *non-collinear*, and the spin plane is not perpendicular the chain direction, an induced polarization appears via Eq. 1.30. This explains very generally the multiferroicity of many noncollinear magnets. The multiferroic state thus described is also clearly “type-II”, since the polarization is zero absent the magnetic ordering. Heuristically, such a spiral magnetic order may occur due to competition between a ferromagnetic nearest neighbor exchange interaction  $J_1$  and an antiferromagnetic next-nearest neighbor interaction  $J_2$  in a 1D spin chain; for  $|J_2/J_1| < 4$  one can show that the ground state is such a noncollinear spiral.

Let us now consider the low-energy excitations of such a 1D chain. The Hamiltonian may be written as

$$H = H_1 + H_2 + H_3 + H_4, \quad (1.31)$$

where

$$H_1 = \sum_i J_1 \vec{S}_i \cdot \vec{S}_{i+1} + J_2 \vec{S}_i \cdot \vec{S}_{i+2}, \quad (1.32)$$

$$H_2 = -\lambda \sum_i \vec{u}_i \cdot [\hat{x} \times (\vec{S}_i \times \vec{S}_{i+1})], \quad (1.33)$$

$$H_3 = \sum_i \frac{\kappa}{2} \vec{u}_i^2 + \frac{1}{2m} \vec{P}_i^2, \quad (1.34)$$

and

$$H_4 = \sum_i D(S_i^z)^2. \quad (1.35)$$

This Hamiltonian describes a 1D spin chain along  $\hat{x}$  interacting with a charge coordinate  $u_i$  (with conjugate momentum  $P_i$ ) via Eq. 1.30. The anisotropy  $D > 0$  pins the magnetic order to the  $xy$  plane. As discussed above, for  $|J_2/J_1| < 4$  the ground state is a noncollinear spin spiral with spins lying in the  $xy$  plane, and the relative angle between adjacent spins is defined by some quantity  $\phi \neq 0, \pi$  which is chosen to minimize the competition between  $J_1$  and  $J_2$ .

[ ] discuss the low-lying excitations of this ground state in light of Eq. 1.31. First of all, clearly uniform rotations of all of the spins in the chain cost zero energy; this is the *Goldstone mode* of Eq. 1.31, and is in direct analogy with the Goldstone mode of the superfluid discussed in Section 1.1.4.1.

If we temporarily set  $D \rightarrow 0^+$  in Eq. 1.35, we may also observe that, in this limit, uniform rotations of the spin spiral *about the chain axis* also cost zero energy. This mode is also a Goldstone mode, although in this case it is due to the spontaneous breaking of the  $\hat{x}$  rotational symmetry rather than the  $\hat{z}$  rotational symmetry. For nonzero  $D$ , this mode of course acquires a finite energy; it is thus referred to as the *pseudo-Goldstone mode*, to highlight the fact that the symmetry is explicitly broken by the Hamiltonian rather than spontaneously broken.

The pseudo-Goldstone mode, however, is still quite interesting—note that, due to Eq. 1.33 and Eq. 1.30, a rotation of the spins about the chain

axis *also* rotates the induced polarization about that axis. This mode is thus our first encounter with an electromagnon, which is any spin boson that acquires a finite electric dipole moment due to coupling to the charge degrees of freedom.

Electromagnons are in fact an intrinsic feature of multiferroics, and what we have discussed above is by no means the only mechanism by which such modes may be achieved.<sup>6</sup> While a complete description of electromagnons and multiferroics is beyond the scope of this work (see [? ] and [? ] for review), I hope to have nevertheless motivated the idea that elementary excitations in correlated systems may still be understood in the context of broken symmetries and the GL paradigm—a notion that we will encounter frequently in the course of this thesis.

## 1.2 Control

From a technological perspective, ultrafast spectroscopy is useful because it helps us understand the physics of materials in equilibrium and how those materials might function in practical applications. Ultrafast control is different in the sense that it seeks to understand the different ways we can *manipulate* materials, with the idea that the knowledge thus gained may be used as a control scheme in some future technology, whether that involves using light or some other stimulus. The material of study is thus of a different kind of importance in ultrafast control—we are more interested in the phenomenology of the light-matter interaction rather than the phenomenology of the material itself. Usually the phenomenology of interest is, for example, being able to control the *state* of the material (like the direction of a magnetization, or the presence of a charge density wave) using light.

In my view, ultrafast control schemes may be divided into two categories. In one case, the dynamics following the light pulse are *coherent*; that is, the light field, for instance, excites coherent oscillations (see Section 1.1.2), and those coherent oscillations drive the system to a new state.<sup>7</sup>

---

<sup>6</sup>For example, in cases where magnetoelastic coupling is strong, a multi-particle excitation in which a spin boson couples to a phonon, and a phonon then couples to the electric polarization, is possible and common[? ].

<sup>7</sup>Here I take the view that simply exciting coherent oscillations (i.e. without a dynamical phase transition) is *not* coherent control, but some may disagree with this

In contrast, *incoherent* dynamics do not involve coherent oscillations of any degrees of freedom; instead, the light is used to, for example, heat the material, or excite quasiparticles away from the Fermi surface. This can also drive the material into a different (nonequilibrium) state, for example by quenching some long-range order (LRO) of the electrons near the Fermi surface, but the mechanism is qualitatively different from the coherent case. We will discuss both cases below.

### **1.2.1 Incoherent control**

#### **1.2.1.1 Heating across a phase transition**

The most basic level of ultrafast control is to use the light pulse simply to heat the material; if the initial and final temperatures lie below and above an equilibrium phase transition, then ultrafast control has been achieved. This is a somewhat trivial mechanism, but it played an important part in early research on ultrafast control, especially in materials where dynamical phase control *not* based on heating was rare or difficult (such as antiferromagnets[? ]). In addition, interactions between the sample area melted by the pump pulse and the surrounding unpumped area may cause interesting effects, such as magnetization reversal in ferromagnetic thin films due to the stray field of the unpumped sample volume[? ]. We are more interested, however, in *nonthermal* ultrafast phenomena—that is, dynamical phenomena which cannot be replicated quasi-adiabatically.

#### **1.2.1.2 Nonthermal melting**

One example of such a phonemonon is the ultrafast quench (or “nonthermal melting”) of some equilibrium order parameter via photoexcitation of electrons by the pump pulse. Let us consider, for example, the case discussed briefly in the beginning of this chapter of a quasi-1D Fermi liquid which becomes gapped by a periodic lattice distortion (i.e. via the Peierls mechanism). The basis for this mechanism is that quasiparticles near the Fermi vector in the undistorted Fermi liquid decrease their energy when the gap is opened (via hybridization of folded bands), which happens at the expense of some energy gain associated with distorting the lattice away from its equilibrium configuration. When light is incident on this

---

point perspective, especially when the amplitude of such oscillations are large.

system in the distorted phase,<sup>8</sup> quasiparticles are excited *away* from the top of the valence band, and the energy savings we gained by distorting the lattice disappears. The system thus relaxes back to its previous configuration and we lose our periodic lattice distortion—the light pulse destroyed the LRO.

Note that this is referred to as a *nonthermal* effect, even though for typical metals the quasiparticles experience an effective temperature change on the order of  $10^3$  K[? ]. Nevertheless, the dynamical phase transition we just described proceeds, by construction, via the creation of a *nonequilibrium* distribution of photoexcited electrons, and in this sense it is nonthermal. There is often difficulty encountered in *proving* that the action of the pump is truly nonthermal. Indeed, the existence of an ordered phase implies some finite temperature  $T_c$  where that order is destroyed by equilibrium thermal fluctuations—it is the job of the experimenter to show that the laser pulse is not simply heating the material above this critical temperature. This is obvious if the phenomenology following the quench (see the next section) is in any case not reproduced in equilibrium, but may also be shown (heuristically) by dividing the energy absorbed by the material from the pulse by the heat capacity.

### 1.2.1.3 Formal model: time-dependent Ginzburg-Landau theory

In describing many-body systems in the static limit, we have seen that it is useful to define a phenomenological model which captures the important physics (via a free energy density, an order parameter, etc.), rather than attempting to treat the inter-particle interactions explicitly. An important concept justifying this practice is the idea of *universality*, which states that, since the correlation length  $\xi$  diverges as we approach the critical point, the physics near the critical point is governed not by the microscopic details of the system but rather by a small set of characteristic quantities like the spatial dimensionality of the system and the symmetry of the order parameter[? ]. This means that to understand any *complicated* system of a particular universality class, it suffices to study the *simplest* system in that universality class, as long as we are close to the critical point.<sup>9</sup>

---

<sup>8</sup>Let us say that the pump photon energy is above the Peierls gap.

<sup>9</sup>The validity of the universality hypothesis away from criticality is not obvious, but is often heuristically assumed to be the case.

In the dynamic limit, the idea of universality is still thought to apply (thus, for example, the wavevector- and frequency-dependent susceptibility  $\chi(\vec{k}, \omega)$  is a homogenous function near the critical point), but the relevant parameters now include not just the spatial dimensionality and symmetry of the order parameter but also new characteristics, like the presence of conserved quantities, and Poisson-bracket relationships between those conserved quantities and the order parameter[? ]. We are thus motivated, as in the static case, to consider *simple models* for each universality class to derive the important limiting behavior—this is the time-dependent Ginzburg-Landau (TDGL) theory. One such model, which is valid when there are no conserved quantities, is the so-called “Model A” equation of motion

$$\frac{\partial\psi(\vec{x}, t)}{\partial t} = -\Gamma \frac{\delta F}{\delta\psi(\vec{x}, t)} + \eta(\vec{x}, t), \quad (1.36)$$

where

$$F = \int \left[ -\frac{t}{2}\psi^2 + \frac{u}{4}\psi^4 + \frac{K}{2}|\nabla\psi|^2 \right] d^d\vec{x} \quad (1.37)$$

and  $\eta$  is a Gaussian white noise source with zero mean and two-point correlation function

$$\langle \eta(\vec{x}, t)\eta(\vec{x}', t') \rangle = 2\Gamma\delta(\vec{x} - \vec{x}')\delta(t - t') \quad (1.38)$$

chosen to satisfy the fluctuation-dissipation theorem.

Different models are appropriate for systems with different conserved quantities. For example, the system which otherwise looks like the above but with where the order parameter is a conserved quantity may be modeled using what is referred to as “Model B”[? ]; the equation of motion is

$$\frac{\partial\psi(\vec{x}, t)}{\partial t} = \lambda\nabla^2 \frac{\delta F}{\delta\psi(\vec{x}, t)} + \eta(\vec{x}, t). \quad (1.39)$$

A comprehensive review of all such models is given by ? ].

#### 1.2.1.4 Dynamics following an ultrafast quench

TDGL is thus used widely to study dynamical phase transitions in many physical systems. An interesting case, which we will treat in detail here due to its applicability to CaMn<sub>2</sub>Bi<sub>2</sub> (see Chapter 6), is when two order

parameters compete with each other in the equilibrium free energy density, and we consider the TDGL dynamics after an *ultrafast quench* of the equilibrium order.<sup>10</sup> The free energy density is

$$f = f_1 + f_2 + f_c, \quad (1.40)$$

where

$$f_i = -\frac{t_i}{2}\psi_i^2 + \frac{u_i}{4}\psi_i^4 + \frac{K_i}{2}(\nabla\psi_i)^2 \quad (1.41)$$

and

$$f_c = c\psi_1^2\psi_2^2. \quad (1.42)$$

Eq. 1.40 describes a system with two single-component order parameters  $\psi_1$  and  $\psi_2$  with a coupling term  $f_c$ . Without loss of generality, let us consider the case where  $t_2 > 0$  and  $t_1 < 0$ , so that  $\psi_2$  is favored in equilibrium, but let  $c$  take some value so that there is an additional local minimum for  $\psi_1 \neq 0$ .

We consider an ultrafast quench of the equilibrium order parameter  $\psi_2$  which corresponds to a free energy density (Eq. 1.40) with  $t_1, t_2 < 0$ . Since neither of the order parameters are conserved quantities, nor are there any other conserved quantities in the system, we are free to use Model A (Eq. 1.36) to describe the dynamics. Using Eq. 1.36, ? ] showed that, as the relaxation proceeds towards (meta)stability, there is a probability

$$p \sim 1 - \zeta^\delta \quad (1.43)$$

that the final state of the system has  $\psi_1 \neq 0$  and  $\psi_2 = 0$ ; i.e., that the order has switched from  $\psi_2$  to  $\psi_1$ . Here,  $\zeta$  is the Ginzburg parameter which is small when the mean-field theory is valid, and  $\delta$  is related to the relaxation rates  $\gamma_1$  and  $\gamma_2$  (see Eq. 1.36) of the two order parameters.<sup>11</sup>

$$\delta \sim \left| \frac{\gamma_1 t_1}{\gamma_2 t_2} \right|. \quad (1.44)$$

Thus, as long as mean-field theory holds and  $\delta > 1$ , the final state after the quench is the metastable state with  $\psi_1 \neq 0$ .

---

<sup>10</sup>This discussion closely follows that of ? ].

<sup>11</sup>This is the value of  $\delta$  when  $\gamma_1 \gg \gamma_2$ , but the same conclusions apply when  $\gamma_1 \gtrsim \gamma_2$ ; see ? ] for details.

The intuition associated with this result is that, following the ultrafast quench, the dynamics are dominated not by whichever state has the lowest free energy in equilibrium, but by the exponential amplification of long-wavelength spatial fluctuations which occurs for *both* order parameters. Thus, even a small relative difference in growth rates of these fluctuations becomes exponentially amplified as the system relaxes. In light of Eq. 1.36, this means that the dynamics are determined not by the minima of the free energy, but by its gradient. At long times the equilibrium state of course recovers, although this recovery involves slower processes like domain nucleation so that the metastable state survives for long timescales.

Many examples of ultrafast trapping into metastable states following an ultrafast quench can be understood in this paradigm. [? ] consider, for instance, the enhancement of superconductivity that occurs in  $\text{La}_{1.675}\text{Eu}_{0.2}\text{Sr}_{0.125}\text{CuO}_4$  upon transient melting of the equilibrium charge density wave (CDW) state in that compound[? ]. Since the CDW state—in contrast to the superconducting state—involves collective motion of electrons and the (heavy) lattice at the same time, recovery of this state after photoexcitation is much slower than recovery of the superconducting state. The superconducting state is thus favored after the quench.

The framework has also been applied to the case of  $\text{LaTe}_3$ , in which an *a*-axis CDW appears in nonequilibrium following a quench of the equilibrium *c*-axis CDW order.<sup>12</sup> In this case, both states are CDWs so the relaxation rates  $\gamma_1$  and  $\gamma_2$  should be roughly equal. Eq. 1.44 should thus be replaced by a more stringent condition which also includes the fact that, if the cooling rate following the quench is too slow, the exponential amplification described above may not be effective in switching to the metastable state[? ].

## 1.2.2 Coherent control

### 1.2.2.1 Via coherent oscillations

In the previous section we described how ultrafast phenomena may be understood phenomenologically using the GL or TDGL paradigm, where the important physics is captured by a generic free energy density whose minima, gradients, etc. determine the relevant phases. In describing the action of the pump pulse, we treated the case where the light only

---

<sup>12</sup>Strictly speaking the induced *a*-axis order is not truly long-ranged, see [? ].

quenches the equilibrium order via excitation of electrons from near the Fermi level, but of course, we know from Section 1.1 that this is hardly the only thing the pump can do. For example, we studied in detail in Section 1.1 that the pump may indeed excite coherent oscillations, and if these oscillations are strong, it turns out that they may also allow us to control the nonequilibrium or metastable phases of materials.

Let us consider for example the free energy density of Eq. 1.40, and let us imagine that the constant  $c$  has some dependence on the coordinate  $Q$  of some collective mode, i.e.

$$f_c = \left( c(0) + \frac{\partial c(Q)}{\partial Q} \Big|_{Q=0} Q + \dots \right) \psi_1^2 \psi_2^2. \quad (1.45)$$

Clearly if the pump pulse brings  $Q$  to some finite value, the free energy landscape may look quite different from equilibrium.

One example of this phenomenon occurs on intense resonant excitation of the 17 THz phonon mode in DyFeO<sub>3</sub>, which is a magnetic material with a thermal metamagnetic transition at 51 K between a low-temperature AFM state and a high-temperature canted-AFM state (with a small magnetic moment). [? ] showed the appearance of a long-lived offset in the Faraday effect signal following excitation which disappeared above 51 K, signaling that the pump pulse triggers an ultrafast phase transition between the two magnetic states in this material. They claim that anharmonic phonon interactions rectify the coherent oscillation of the 17 THz phonon mode and transfer a finite, time-independent amplitude to a *different* phonon mode associated with the displacement of Dy<sup>3+</sup> ions. This displacement causes a long-lived change in the magnetic exchange interaction which modifies the free energy density and triggers a phase transition in a manner resembling Eq. 1.45. This is just one example of a whole field of research referred to as *nonlinear phononics*[? ], which seeks to use anharmonic interactions like these to effect control over the crystal lattice with light.

### 1.2.2.2 Via Floquet engineering

A related scenario occurs when the light couples not to the constants  $t$ ,  $u$ ,  $c$ , etc. of the free energy, but rather acts as a *field*  $h$  for one of the order parameters, i.e. by the IFE (see Section 1.1.3.2). Then we have, for

example,

$$f(t) = f(0) + h(t)\psi_1(t). \quad (1.46)$$

and the field may thus provide an ultrafast “kick” to push the material into a new state.<sup>13</sup> In this case, the purpose of the pump is *not* to excite coherent oscillations—which go on to modify the free energy landscape—but rather to control the free energy landscape via the light-matter interaction *itself*. The study of mechanisms which fall under this umbrella is known as “Floquet engineering”[?], referring to the Floquet theorem[?] which gives the energy eigenstates of a Hamiltonian which is periodic in time.

The fact that an ultrafast light pulse may produce Floquet bands in solids and that those bands may hybridize with the eigenstates of the time-independent Hamiltonian was established by [?] and later [?] using time-resolved photoemission spectroscopy. Multiple control strategies using this effect, like the manipulation of band topologies[?], observation of a large optical stark effect[?], and manipulation of the magnetic exchange energy[?], were shown to occur as a result of this effect. A complete accounting of the progress experimentally and theoretically in this field is beyond the present scope, but the literature has been reviewed extensively by, e.g. [?] and [?].

### 1.2.3 Control as spectroscopy

The above treatment of ultrafast control was motivated by a desire to manipulate quantum materials with light for some practical benefit, such as, for example, being able to control the direction of the spins in a magnetic memory device. However, there is an additional, related motivation which is quite important to note. Clearly, the mechanism by which the light manipulates the phases of materials depends quite sensitively on the material characteristics; for example, the discussion in Section 1.2.1.4 depended critically on the fact that the two order parameters  $\psi_1$  and  $\psi_2$  compete in equilibrium—a which may not be obvious otherwise! Indeed, the fact that light may be used to suppress some phases and enhance others is sometimes the only information we have about how and whether

---

<sup>13</sup>This is especially relevant in the case of magnets, where the magnetic field from the IFE can couple directly to the magnetic moment, although one needs inertial terms in the Lagrangian which are not present in the Landau-Lifshitz equation for a simple ferromagnet[?].

those different phases interact with each other. The fact that CDW order competes with superconductivity in cuprates is, for example, strongly evidenced by the enhancement of superconductivity that occurs upon a photoinduced quench of the CDW order[? ]. A similar observation about CDWs in  $\text{CsV}_3\text{Sb}_5$  was recently reported by ? ]. The line between ultrafast spectroscopy and ultrafast control should not, then, be considered particularly sharp, and both of the motivations described here—to learn about materials, and to manipulate materials—are deeply related to one another.



## Chapter 2

---

### *Second harmonic generation: theory*

## 2.1 Space groups, point groups, and Neumann's principle

The utility of SHG in studying condensed matter systems is derived from the following simple statement, attributed to Franz Neumann[?] and later Pierre Curie[?]:

**Theorem 2.1.1 (Neumann's principle)** *Let  $P_G$  be the symmetry group of a crystal structure and  $P_H$  the symmetry group of some physical property of that crystal. Then,  $P_G$  is a subgroup of  $P_H$ .*

There are a few things to digest here. Let us start by understanding the meaning of the phrase “symmetry group”. For any given crystal, there exists some infinitely large set of operations  $G$  under which the crystal structure is symmetric. Each of these operations may be decomposed into two parts: a “point-preserving operation”  $R$ , corresponding to either the identity, rotation, inversion, mirror, or the product of mirror and rotation, followed by a translation by some vector  $\tau$ :

$$G = \{(R|\tau)\} \quad (2.1)$$

where  $(R|\tau)$  means “Perform  $R$ , then translate by  $\tau$ ”. Clearly, the set  $G$  forms a group, since if both  $g_1$  and  $g_2 \in G$  leave the crystal structure invariant, so does the product  $g_1g_2$ , and so  $g_1g_2 \in G$ . Thus,  $G$  is called the *space group* of the crystal. In three dimensions, there are 230 crystallographic space groups, which are tabulated in a number of places, most usefully Wikipedia[?].

For 73 of these groups, the translation parts of the  $\tau$ 's in Eq. 2.1 are only ever linear combinations of integer multiples of the lattice vectors

*a*, *b*, and *c*; these are called *symmorphic* space groups. The remaining 157 groups involve translations that are not integer multiples of the lattice vectors; these are one's screw axes and glide planes, and so these groups are called *asymmorphic*.

Importantly, the “physical properties” of theorem 2.1.1 refer to the truly macroscopic properties of the crystal, like its conductivity, dielectric, or pyroelectric tensors. Consider, for example, that in SHG, we are typically studying the sample at optical wavelengths, where the wavelength of light is three or four orders of magnitude larger than the lattice spacing. Clearly, then, these properties do not care whether the correct symmetry is  $(R|\tau)$  or  $(R|\tau + a/2)$ . A more useful group, then, is the *point group* of the crystal

$$P_G = \{R \text{ s.t. } \exists \tau \text{ s.t. } (R|\tau) \in G\} \quad (2.2)$$

i.e., the point group is the set of point-preserving operations  $R$  for which  $R$  appears in  $G$ , regardless of whether you need to perform a translation with it. Once can show that  $P_G$  is also a group, and thus it is  $P_G$  which is involved in Neumann’s principle for all intents and purposes<sup>1</sup>.

The last ingredient that we need to understand theorem 2.1.1 is the concept of what is meant by “physical property”. The idea is that the response of the crystal  $J_{i_1 i_2 \dots i_n}$  (i.e., the current  $J_i$ , or the quadrupole moment  $Q_{ij}$ ) is proportional to some field  $F_{i'_1 i'_2 \dots i'_m}$  via some tensor  $\chi$ :

$$J_{i_1 i_2 \dots i_n} = \chi_{i_1 i_2 \dots i_n i'_1 i'_2 \dots i'_m} F_{i'_1 i'_2 \dots i'_m}. \quad (2.3)$$

For example, the conductivity  $\sigma_{ij}$  relates a current density  $J_i$  to an applied electric field  $E_j$ :

$$J_i = \sigma_{ij} E_j. \quad (2.4)$$

Likewise, the polarization  $P_i$  due to the pyroelectric effect is related to the a temperature difference  $\Delta T$  by a tensor  $p_i$ :

$$P_i = p_i \Delta T. \quad (2.5)$$

The tensors  $\sigma_{ij}$ ,  $p_i$ , and generally,  $\chi_{i_1 i_2 \dots i_n i'_1 i'_2 \dots i'_m}$  are commonly referred to as *matter tensors*[?], to emphasize the fact that they are the only part of

---

<sup>1</sup>Of course this breaks down when the wavelength of light is comparable to the lattice spacing; in that case you need to consider the full space group.

the response equations that depend on the material. It should be noted that matter tensors generically come in two types: those that transform like a vector under inversion and those that transform like a pseudovector under inversion. You can tell which is which by applying inversion to either side of the response equation. For example, the tensor  $\epsilon_{ij}$  relating the displacement field to the electric field

$$D_i = \epsilon_{ij} E_j \quad (2.6)$$

is a polar tensor, whereas the tensor  $\chi_{ij}^{me}$  describing the magnetoelectric effect

$$M_i = \chi_{ij}^{me} E_j \quad (2.7)$$

is an axial tensor.

We are now ready to restate theorem 2.1.1 in a slightly more useful form, using the terminology we have developed about point groups and matter tensors:

**Theorem 2.1.2 (Neumann's principle, restated)** *Let  $P_G$  be the point group of a given crystal, and let  $\chi$  be a matter tensor describing some response function of that crystal. Then, for all  $g \in P_G$ , we have*

$$g(\chi) = \chi. \quad (2.8)$$

Eq. 2.8 can be more usefully expressed if we know the matrix  $R_{ij}^g$  corresponding to  $g$ . For example, if  $g$  is “threefold rotation about the  $z$  axis”, we have

$$R_{ij}^g = \begin{pmatrix} -\frac{1}{2} & -\frac{\sqrt{3}}{2} & 0 \\ \frac{\sqrt{3}}{2} & -\frac{1}{2} & 0 \\ 0 & 0 & 1 \end{pmatrix}, \quad (2.9)$$

in which case one can show that Eq. 2.8 reads

$$(\det R^g)^t R_{i_1 i'_1}^g R_{i_2 i'_2}^g \cdots R_{i_n i'_n}^g \chi_{i'_1 i'_2 \cdots i'_n} = \chi_{i_1 i_2 \cdots i_n}, \quad (2.10)$$

where  $t$  is 0 if  $\chi$  is a polar tensor and 1 if  $\chi$  is an axial tensor. Theorem 2.1.2 tells us that there is one copy of Eq. 2.10 for each  $g \in P_G$ .

Apparently, each element  $g \in P_G$  gives us a *constraint* on the numbers  $\chi_{i_1 i_2 \cdots i_n}$ , in that they have to satisfy Eq. 2.10. This is a remarkably useful fact. Since different point groups enforce different constraints on  $\chi$ , that

means the *form* of  $\chi$  (e.g. when written as a list of numbers) depends quite sensitively on the point group of the crystal we are studying. As an example, here is the dielectric permittivity tensor for crystals with the point group (in Schoenflies notation)  $C_2$ :

$$\epsilon_{ij} = \begin{pmatrix} a & 0 & e \\ 0 & b & 0 \\ e & 0 & c \end{pmatrix}_{ij} \quad (2.11)$$

versus in the point group  $D_{3d}$ :

$$\epsilon_{ij} = \begin{pmatrix} a & 0 & 0 \\ 0 & a & 0 \\ 0 & 0 & c \end{pmatrix}_{ij}. \quad (2.12)$$

Clearly, any *measurement* of  $\epsilon_{ij}$  will be able to easily differentiate a crystal with point group  $C_2$  from one with point group  $D_{3d}$ . This is the fundamental basis, then, for SHG. In SHG, we measure the tensor  $\chi_{ijk}$  corresponding to the response equation<sup>2</sup>

$$P_i(2\omega) = \chi_{ijk} E_j(\omega) E_k(\omega); \quad (2.13)$$

the numbers  $\chi_{ijk}$  thus tell us about the crystallographic point group we are measuring from.

There are a couple of advantages to measuring  $\chi_{ijk}$  over any other matter tensor in a given system. For one thing,  $\chi_{ijk}$  is a third rank tensor, which means it has a few more degrees of freedom to work with compared to  $\epsilon_{ij}$ , and thus does a better job at uniquely specifying each point group. It also doesn't have *too many* degrees of freedom, so that most of the time your experiment will be able to tell you all of your tensor elements<sup>3</sup>. In addition, since we are typically doing SHG at optical wavelengths, the form of  $\chi_{ijk}$  reflects the symmetry of the *charge distribution*  $\rho(\mathbf{x})$ , in contrast to e.g. x-ray diffraction, where the relevant tensors will tell instead you about the electron distribution,  $n(\mathbf{x})$ . This can be advantageous in cases where the long range order you are trying to study involves an ordering of the valence electrons but not the electrons in the cores of atoms. This is

---

<sup>2</sup>This discussion is a bit simplified in the sense that there are actually *many* response functions which will give you light at  $2\omega$ ; for a more detailed discussion, see Section 2.2.

<sup>3</sup>Quadrupole SHG has this problem, see Section 2.2.

entirely the result of the fact that Neumann's principle, as expressed both in theorem 2.1.1 and theorem 2.1.2, tells us that the point group of our crystal is a *subgroup* of the point group we get from our measurement—the measurement can always be more symmetric than the crystal!

As another example of this fact, let us note that the response equation given by Eq. 2.13 clearly has an additional symmetry  $j \leftrightarrow k$ , since the two copies of the electric field on the right hand side are equivalent. Obviously this is not a result of the material we are studying, it is simply a fact of doing SHG. Thus, in addition to the constraints given by Neumann's principle and Eq. 2.10, we have the additional constraint

$$\chi_{ijk} = \chi_{ikj} \forall i, j, k. \quad (2.14)$$

This is known as *particularization*[? ].

## 2.2 A classical understanding of SHG

In the last section we considered the SHG response function given by Eq. 2.13. Where does this relationship come from, and how is  $P(2\omega)$  eventually measured? Our starting point in the classical treatment will be the inhomogenous electromagnetic wave equation

$$\left( \nabla^2 - \frac{1}{c^2} \frac{\partial^2}{\partial t^2} \right) E_i(\mathbf{x}, t) = S_i(\mathbf{x}, t), \quad (2.15)$$

which we understand as defining the field  $E_i(\mathbf{x}, t)$  radiated by the source term  $S_i(\mathbf{x}, t)$ , which is induced by the incident field. To lowest order in a multipole expansion,  $S_i(\mathbf{x}, t)$  is given by[? ? ]

$$\mu_0 \frac{\partial^2 P_i(\mathbf{x}, t)}{\partial t^2} + \mu_0 \left( \epsilon_{ijk} \nabla_j \frac{\partial M_k(\mathbf{x}, t)}{\partial t} \right) - \mu_0 \left( \nabla_j \frac{\partial^2 Q_{ij}(\mathbf{x}, t)}{\partial t^2} \right) \quad (2.16)$$

where  $P_i(\mathbf{x}, t)$ ,  $M_i(\mathbf{x}, t)$ , and  $Q_{ij}(\mathbf{x}, t)$  are the induced electric dipole, magnetic dipole, and electric quadrupole densities, and  $\epsilon_{ijk}$  is the Levi-Civita tensor.

If the incident electric field is small, then the terms  $P_i(\mathbf{x}, t)$ ,  $M_i(\mathbf{x}, t)$ , and  $Q_{ij}(\mathbf{x}, t)$  are linear functions of that electric field. However, for larger

incident fields (such as those generated by pulsed lasers), they may be more generally written as a taylor series:

$$P_i = \chi_{ij}^{ee} E_j + \chi_{ij}^{em} H_j + \chi_{ijk}^{eee} E_j E_k + \chi_{ijk}^{eem} E_j H_k + \dots \quad (2.17)$$

$$M_i = \chi_{ij}^{me} E_j + \chi_{ij}^{mm} H_j + \chi_{ijk}^{mee} E_j E_k + \chi_{ijk}^{mem} E_j H_k + \dots \quad (2.18)$$

$$Q_{ij} = \chi_{ijk}^{qe} E_k + \chi_{ijk}^{qm} H_k + \chi_{ijkl}^{qee} E_k E_l + \chi_{ijkl}^{qem} E_k H_l + \dots \quad (2.19)$$

where we have suppressed the arguments  $\mathbf{x}$  and  $t$  for brevity.

Assuming the incident field is monochromatic,

$$E_i(\mathbf{x}, t) = E_i(\omega) e^{i(\mathbf{k} \cdot \mathbf{x} - \omega t)} + \text{c.c.} \quad (2.20)$$

$$H_i(\mathbf{x}, t) = H_i(\omega) e^{i(\mathbf{k} \cdot \mathbf{x} - \omega t)} + \text{c.c.} \quad (2.21)$$

the induced sources are also monochromatic, and (keeping only terms proportional to  $e^{i2\omega t}$ ) we thus get

$$P_i(2\omega) = \chi_{ijk}^{eee} E_j(\omega) E_k(\omega) + \chi_{ijk}^{eem} E_j(\omega) H_k(\omega) \quad (2.22)$$

$$M_i(2\omega) = \chi_{ijk}^{mee} E_j(\omega) E_k(\omega) + \chi_{ijk}^{mem} E_j(\omega) H_k(\omega) \quad (2.23)$$

$$Q_{ij}(2\omega) = \chi_{ijkl}^{qee} E_k(\omega) E_l(\omega) + \chi_{ijkl}^{qem} E_k(\omega) H_l(\omega). \quad (2.24)$$

Since Eq. 2.15 is linear, the electric field radiated by  $S_i(\mathbf{x}, t)$  is simply proportional to it. In the limit where the first term of Eq. 2.22 dominates, the intensity measured at our detector thus satisfies

$$I(2\omega) \propto |\hat{e}_i^{\text{out}} \chi_{ijk}^{eee} \hat{e}_j^{\text{in}} \hat{e}_k^{\text{in}}|^2, \quad (2.25)$$

where  $\hat{e}^{\text{in}}$  and  $\hat{e}^{\text{out}}$  are unit vectors in the direction of the incoming and measured electric fields<sup>4</sup>.  $\chi_{ijk}^{eee}$  does typically dominate when inversion symmetry is broken, but if not, you have to consider all of the terms in Eqs. 2.22–2.24. Actually, each of these terms needs to be considered twice, since there is both a surface contribution and a bulk contribution<sup>5</sup>. In my experience, the heirarchy of contributions (from most to least important, and assuming everything is allowed by symmetry) is typically:

1. Bulk electric dipole

---

<sup>4</sup>Usually there are polarizers in the experiment which define these directions.

<sup>5</sup>The space group which constrains the surface contributions is the bulk space group less the operations which involve some change in the  $z$  coordinate.

2. Surface electric dipole, bulk electric quadrupole, and bulk magnetic dipole, at the same order<sup>6</sup>
3. Everything else

I've never seen anything outside of items 1 and 2, but in rare cases an electronic resonance may cause an enhancement in one of the other contributions[? ].

Let us take a moment now to emphasize the following extremely common misconception about SHG: just because you see SHG in your experiment, that does not mean that inversion symmetry is broken in your material! It also does not mean that your material is a ferroelectric, or really that there's anything special at all about your material, at least before you've done any further analysis. Similarly, if you *don't* see SHG, that doesn't mean inversion symmetry is preserved, either. I have repeatedly seen large electric quadrupole SHG show up in materials with inversion symmetry, while materials which definitely break inversion symmetry have absolutely zero SHG observable in the experiment. The reason for this is ultimately due to resonance, a topic which I will discuss in Section 2.3, but I mention it here because it is truly quite common in the literature and it is surely a mistake worth avoiding. You are "allowed" to say your material breaks inversion symmetry only if there is no other contribution in Eqs. 2.22–2.24 which fits your data, and you are basically never allowed to say that your material preserves inversion symmetry when there is no SHG (a fact that should be obvious on a careful reading of theorem 2.1.1).

## 2.3 SHG in quantum mechanics

The description of SHG in the previous section is probably the most useful for understanding SHG from an "optics" perspective, but it gives little insight into the true microscopic origin of the SHG intensity. The quantum description, on the other hand, will tell you exactly where the SHG is coming from microscopically, but only if you have access to

---

<sup>6</sup>Somehow the bulk electric quadrupole and magnetic dipole contributions have been labelled "exotic" by some in the community, but that has not been my experience. If I had to guess, almost half of the materials I have measured with inversion symmetry show electric quadrupole SHG.

the eigenfunctions  $|\psi\rangle$  of your hamiltonian—it is of little use otherwise. Nevertheless, we can still gain intuition about the dependence of our SHG intensity on the frequency of the light in the quantum picture, which will be useful for clearing up a whole other slew of misconceptions that have somehow made their way into the SHG literature. This treatment closely follows that of [?].

The starting point is to describe the system under study as a statistical ensemble specified by a Hamiltonian

$$H = H_0 + \lambda V \quad (2.26)$$

and a density matrix

$$\rho(t) = \sum_i p_i(t) |\psi_i(t)\rangle \langle \psi_i(t)| \quad (2.27)$$

where the  $p_i(t)$ 's specify the classical probability of the system being in state  $i$  at time  $t$ , and the  $|\psi_i\rangle$ 's are wavefunctions given by

$$|\psi_i(t)\rangle = \sum_n c_n^i(t) |n\rangle \quad (2.28)$$

for some  $\{c_n^i(t)\}$ , where

$$H_0 |n\rangle = E_n |n\rangle \quad (2.29)$$

for all  $n$ . In the presence of damping, the elements

$$\rho_{nm} = \langle \psi_n | \rho | \psi_m \rangle \quad (2.30)$$

of  $\rho$  satisfy the differential equation

$$\dot{\rho}_{nm} = \frac{1}{i\hbar} [H, \rho]_{nm} - \gamma_{nm} (\rho_{nm} - \rho_{nm}^{(eq)}), \quad (2.31)$$

where  $\gamma_{nm}$  is a matrix of (phenomenological) damping parameters<sup>7</sup>, and  $\rho_{nm}^{(eq)}$  is the density matrix corresponding to the equilibrium steady state of the system.

We consider the case where  $V$  may be treated as a perturbation on top of  $H_0$ , i.e. where  $\lambda$  is small. In this case, Eq. 2.31 can be written

$$\dot{\rho}_{nm} = -i\omega_{nm}\rho_{nm} + \frac{1}{i\hbar} \sum_k \lambda (V_{nk}\rho_{km} - \rho_{nk}V_{km}) - \gamma_{nm}(\rho_{nm} - \rho_{nm}^{(eq)}), \quad (2.32)$$

---

<sup>7</sup>This is just one choice of  $p_i(t)$ .

where  $\omega_{nm} = E_{nm}/\hbar$ , and we seek a solution

$$\rho_{nm} = \rho_{nm}^{(0)} + \lambda \rho_{nm}^{(1)} + \lambda^2 \rho_{nm}^{(2)} + \dots . \quad (2.33)$$

Turning the crank (see [? ] for details) gives us the solution

$$\rho_{nm}^{(N)}(t) = \int_{-\infty}^t \frac{1}{i\hbar} [\lambda V(t'), \rho_{nm}^{(N-1)}(t')] e^{(i\omega_{nm} + \gamma_{nm})(t' - t)} dt'. \quad (2.34)$$

Carrying out this series to second order in  $\lambda$  with the perturbation  $V(t) = -\boldsymbol{\mu} \cdot \mathbf{E}(t)$ , where  $\boldsymbol{\mu}$  is the dipole moment and  $\mathbf{E}(t) = \sum_q \mathbf{E}(\omega_q) e^{-i\omega_q t}$  is the incident electric field, we get an expression for the density matrix  $\rho_{nm}^{(2)}(t)$  as a function of the dipole matrix elements

$$\boldsymbol{\mu}_{nm} = \langle n | \boldsymbol{\mu} | m \rangle, \quad (2.35)$$

the frequencies  $\omega_q$ , the damping constants  $\gamma_{nm}$ , and  $\rho_{nm}^{(0)}$ .

Once we have  $\rho_{nm}^{(2)}(t)$ , we can compute the expectation value

$$\langle \boldsymbol{\mu}(t) \rangle = \sum_{nm} \rho_{nm}(t) \boldsymbol{\mu}_{nm}, \quad (2.36)$$

from which the susceptibility can be computed by taking two derivatives with respect to the electric field amplitudes<sup>8</sup>. Reproducing the final answer here (again, from [? ]):

$$\begin{aligned} \chi_{ijk}^{(2)}(\omega_p + \omega_q, \omega_q, \omega_p) &= \frac{1}{2\epsilon_0 \hbar^2} \sum_{lmn} (\rho_{ll}^{(0)} - \rho_{mm}^{(0)}) \times \Big\{ \\ &\quad \frac{\mu_{ln}^i \mu_{nm}^j \mu_{ml}^k}{[(\omega_{nl} - \omega_p - \omega_q) - i\gamma_{nl}][(\omega_{ml} - \omega_p) - i\gamma_{ml}]} \\ &\quad + \frac{\mu_{ln}^i \mu_{nm}^k \mu_{ml}^j}{[(\omega_{nl} - \omega_p - \omega_q) - i\gamma_{nl}][(\omega_{ml} - \omega_q) - i\gamma_{ml}]} \\ &\quad + \frac{\mu_{ln}^j \mu_{nm}^i \mu_{ml}^k}{[(\omega_{nm} + \omega_p + \omega_q) + i\gamma_{nm}][(\omega_{ml} - \omega_p) - i\gamma_{ml}]} \\ &\quad + \frac{\mu_{ln}^k \mu_{nm}^i \mu_{ml}^j}{[(\omega_{nm} + \omega_p + \omega_q) + i\gamma_{nm}][(\omega_{ml} - \omega_q) - i\gamma_{ml}]} \Big\}, \end{aligned} \quad (2.37)$$

---

<sup>8</sup>We are specializing here to the case of electric dipole SHG, although the calculation proceeds similarly for magnetic dipole and electric quadrupole.

where  $\omega_{nm} = \omega_n - \omega_m$ . The SHG susceptibility tensor is then obtained by taking the limit  $\omega_p = \omega_q$ .

We learned two things by doing the quantum calculation. First of all, clearly if we know all of the eigenfunctions  $|n\rangle$  of our unperturbed Hamiltonian, we can calculate the susceptibility tensor *a priori*, although this is obviously difficult except in the simplest of cases. Secondly, we notice that there are two types of denominators in Eq. 2.37: those occurring at  $2\omega$  (remember we have set  $\omega_q = \omega_p$ ) and those occurring at  $\omega$ . Both can cause resonances in the SHG intensity and are observed abundantly in experiment[? ]. The existence of resonances in the SHG spectrum makes comparison between different materials quite difficult if reference is made only to the SHG intensity at a single color. In one infamous example, [?] incorrectly attributed the large SHG amplitude at optical wavelengths in TaAs to the presence of Weyl nodes near the Fermi level; later SHG spectroscopy measurements demonstrated that the enhancement was due to a simple band resonance at the excitation frequency used in that paper[? ]. The emerging consensus is that the SHG intensity at optical frequencies has more or less nothing to do with the low-energy excitation spectrum or its topology.

## 2.4 SHG in the Ginzburg-Landau paradigm

While Eq. 2.37 is quite general and completely correct microscopically, it obviously lends very little intuition into what kind of phenomenology we can expect to find in the SHG signal, say, across a phase transition, where the dipole matrix elements which determine Eq. 2.37 certainly change but may not do so in a simple or straightforward way. An alternative approach is to treat SHG in a generalized Ginzburg-Landau paradigm, in which all of the physics of the system is cast in terms of an order parameter  $\mathcal{O}_{i_1 i_2 \dots i_r}$ . This approach was mainly developed by [? ], based off of early work by [? ] in the 1960s.

The key insight of Pershan is that one can define a “time-averaged free energy” in nonlinear optics by considering the term (assuming the incident field  $E^{\text{in}}(t)$  is monochromatic with frequency  $\omega$ )

$$F_{\text{SHG}} = -P_i(2\omega)E_i^{*\text{out}}(2\omega) + \text{c.c.} \quad (2.38)$$

$$= -[\chi_{ijk}E_i^{*\text{out}}(2\omega)E_j^{\text{in}}(\omega)E_k^{\text{in}}(\omega) + \text{c.c.}] \quad (2.39)$$

Since  $F$  is a free energy, it must be a real, totally symmetric scalar, and Eq. 2.39 thus gives us a way to *derive* the form of the tensor  $\chi_{ijk}$  in a particular point group using similar arguments as in Section 2.1.

In the context of a (spontaneous) symmetry-breaking transition at  $T_c$ , the Ginzburg Landau paradigm asserts that the free energy of Eq. 2.39 still obeys the symmetry group of the high temperature phase, even though the low temperature phase explicitly breaks some of those symmetries. This is because the spontaneous symmetry breaking is considered a property of the *solution* of the free energy minimization problem, rather than a property of the minimization problem itself. Thus, a valid expression for the free energy in the low temperature phase is given by

$$F = -[\chi_{ijkl_1l_2\dots l_r}(T > T_c)E_i^{*\text{out}}(2\omega)E_j^{\text{in}}(\omega)E_k^{\text{in}}(\omega) + \text{c.c.}] \mathcal{O}_{l_1l_2\dots l_r}. \quad (2.40)$$

Comparing Eqs. 2.39 and 2.40, we have an equation for the SHG susceptibility tensor in the low temperature phase

$$\chi_{ijk}(T < T_c) = \chi_{ijkl_1l_2\dots l_r}(T > T_c) \mathcal{O}_{l_1l_2\dots l_r}. \quad (2.41)$$

In light of Eq. 2.41, let us consider the consequences of the symmetry of  $\mathcal{O}$  on the SHG signal. For simplicity, let us consider a situation that resembles a ferroelectric phase transition; i.e., the high temperature phase preserves inversion symmetry, but the low temperature phase involves the emergence of a rank-1 order parameter  $\mathcal{O}_l$  which is odd under inversion. In that case, we have

$$\chi_{ijk}(T < T_c) = \chi_{ijkl}(T > T_c) \mathcal{O}_l(T), \quad (2.42)$$

i.e. the SHG at low temperature is simply a product of a high-temperature tensor and the order parameter  $\mathcal{O}$ . We of course need to check that  $\chi_{ijkl}$  is allowed in the high temperature phase; here, we need  $\chi_{ijkl}$  to be an even rank polar tensor, which is allowed in the presence of inversion symmetry (see Eq. 2.10).

Let us now imagine that the polarization  $\mathcal{O}_l$  is known to be directed along the  $y$  axis, i.e.

$$\mathcal{O}_l = (0, P_0, 0)_l, \quad (2.43)$$

for some  $P_0$ . Then, by Eq. 2.42, we have

$$\chi_{ijk}(T < T_c) = \chi_{ikjy}(T > T_c)P_0. \quad (2.44)$$

Besides telling us that the susceptibility tensor is linear in the polarization magnitude  $P_0$ , what this formulation gets us is also that the elements of  $\chi_{ijk}$  are just the elements of  $\chi_{ijkl}$  with  $l = y$ . In many cases this is more information than you would have if you only knew the point group of the low temperature phase!

Eq. 2.41 is also quite useful in the case where the low temperature phase is heterogenous; i.e. the order parameter  $\mathcal{O}$  varies spatially from one point to another. This is commonly the case in magnets, for example, where rotational symmetry is spontaneously broken at  $T_c$  and the low temperature free energy thus consists of multiple energetically degenerate states related to each other by elements  $R$  of the high temperature point group which are broken at low temperature. These states have the same free energy since, again, the symmetry-breaking is due to the order parameter, not due to the free energy itself. The order parameter in the different domains are thus related to each other via

$$\mathcal{O}_{i_1 i_2 \dots i_r}(\mathbf{x}_1) = R[\mathcal{O}_{i_1 i_2 \dots i_r}(\mathbf{x}_2)], \quad (2.45)$$

where the right hand side is given by Eq. 2.10. Combining Eq. 2.41 and Eq. 2.45, the SHG tensor thus satisfies

$$\chi_{ijk}(\mathbf{x}_1) = R[\chi_{ijk}(\mathbf{x}_2)]. \quad (2.46)$$

Eq. 2.46 is the fundamental basis for our SHG works on 1T-TaS<sub>2</sub> and CaMn<sub>2</sub>Bi<sub>2</sub>, discussed in chapters Chapter 5 and Chapter 6.

## Chapter 3

---

### *Second harmonic generation: practical*

#### 3.1 Description of the setup

In the last chapter we saw that the SHG intensity in a given crystal is related to the point group, order parameter, band structure, etc. of that crystal via the susceptibility tensor  $\chi_{ijk}$ . It is also obvious from Section 2.1 that the ideal scenario is to be able to measure as many of the numbers  $\chi_{ijk}$  as possible; after all, if you only measured the  $xx$  component of Eqs. 2.11 and 2.12, you would have obtained essentially no information about your crystal whatsoever. The SHG setup that we built (whose design is mostly credited to Torchinsky and Hsieh[?], with some improvements by us which I will discuss below) was designed with exactly this goal in mind. There are two key insights which make this design work: one, the light is obliquely incident on the sample so there is some component of  $E^{\text{in}}$  directed along the sample normal, and two, we rotate the plane of incidence so that the in-plane field direction sweeps an entire  $360^\circ$ . The first point allows us to measure elements of  $\chi_{ijk}$  with  $z$  indices<sup>1</sup>, and the second point makes sure we get all of the  $x$  and  $y$  elements of  $\chi_{ijk}$  too. All of the tensor elements are thus given a chance to contribute to the SHG intensity in a given experiment.

With those considerations in mind, let me proceed to give a schematic description of our SHG setup (see Figs. 3.1 and 3.2). Some of the choices we made may seem arbitrary right now, but I will go over them in detail in Section 3.2. The starting point is our regenerative amplifier (Spectra-Physics Spitfire Sptf-100f-5k-xp), which produces 100 fs 800 nm pulses at a 5 kHz repetition rate from an 86 MHz seed laser (Spectra-Physics Tsunami 3941-M1S). 90% of the beam is split off to power an optical parametric amplifier (OPA), and the remaining 10% is used for the SHG probe beam.

---

<sup>1</sup>Here and unless otherwise noted I define the sample normal to be the  $z$  axis.

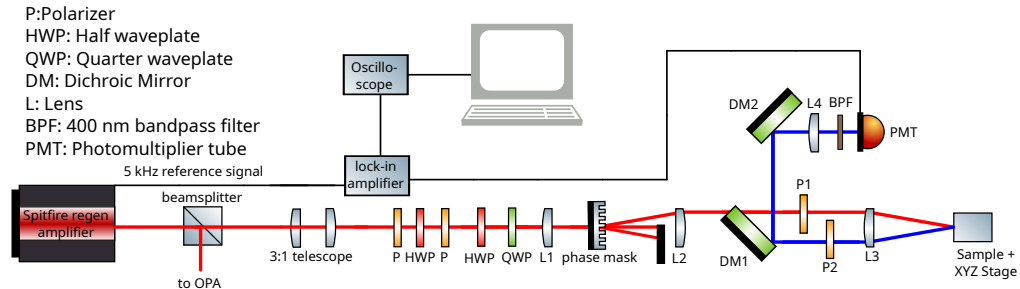


Figure 3.1: Schematic drawing of the SHG setup used in this research. After ? ].

After passing through an optical telescope, which creates a collimated beam of width 1 – 2 mm, this beam is attenuated with a polarizer - half-wave plate - polarizer triplet, and then elliptically polarized with a quarter-wave plate and half-wave plate in series. The ellipticity at this stage is set so the light is perfectly circularly polarized following transmission through a phase mask, as described below.

After passing through these polarization optics, the beam is focused with a lens onto the aforementioned phase mask, which acts as a transmissive diffraction grating and separates the beam into multiple different diffraction orders. The +1 order diffraction comes off at an angle of roughly 7°, while the other orders are blocked with anodized aluminum foil. This (diverging) beam then propagates at 7° to the optical axis before meeting a lens set at the appropriate distance so as to both collimate the beam and rectify the 7° propagation angle. Then, the light passes through a dichroic mirror (which transmits 800 nm and reflects 400 nm), becomes linearly polarized by a wire-grid polarizer, and is then focused onto the sample at a 10° angle of incidence by passing through the edge of a 1 in-diameter 50 mm achromatic focusing lens. The interaction between the light and the sample causes SHG to be radiated in reflection at the same 10° angle of incidence, so that the SHG beam passes through the opposite side of the 50 mm lens before passing through a second, independent polarizer which is used to control the polarization of the measured light.

Finally, the polarized output reflects off of two dichroic mirrors (oriented in such a way as to cancel the differing effect of the Fresnel equations on the reflectivity of S and P polarized light) and is focused through a

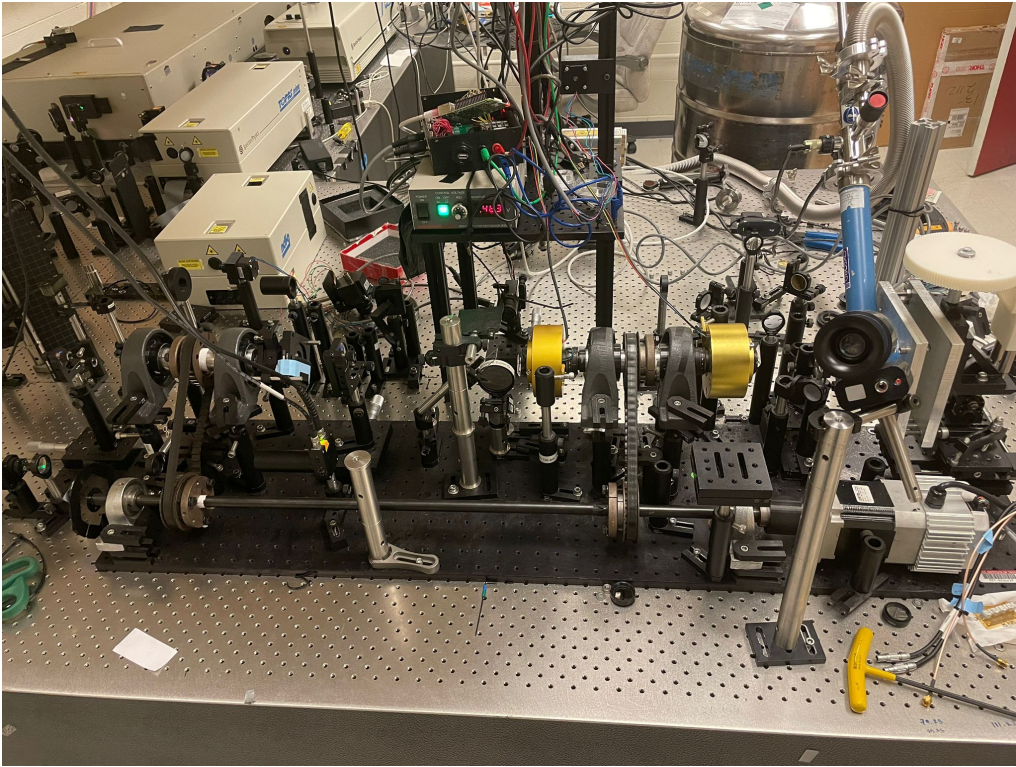


Figure 3.2: Photograph of the SHG setup used in this research. The sample lies in the blue cryostat on the right side of the image. The phase mask is mounted in a black holder with blue masking tape on the left side, and the polarizers are mounted in the two gold-colored slip rings (described in Chapter 4).

400 nm bandpass filter onto a photomultiplier tube (PMT) by a 400 mm lens. The current output of the PMT is filtered by a lock-in amplifier (for static SHG, set to the 5 kHz repetition rate of the laser) and read out on an oscilloscope. The phase mask, incoming polarizer, and outgoing polarizer are mounted on rotating lens tubes which are connected via pulley to a common motor shaft driven at  $\sim 5$  Hz by a brushless DC motor. The motor thus continuously rotates the plane of incidence of the experiment, since the latter is entirely defined by the phase mask and the polarizers. The rotation angle is tracked as a function of time by an optical rotary encoder, consisting of a laser pointer passed through a chopper wheel

(with 100 slots) mounted at the end of the motor shaft and detected via photodiode. The encoder signal and the lock-in signal are both sent to a homemade oscilloscope (an Arduino Uno microcontroller which separates the lock-in signal into different individual rotations by looking for peaks in the encoder signal), the output of which is sent to a computer for further data processing.

## 3.2 Before you build

I list here a few essential aspects of SHG that should be considered before designing a new setup.

### 3.2.1 Spot size

One of the most important quantities in an SHG setup is the diameter of the probe spot. Ideally, this diameter is as small as possible, so as to measure the smallest samples or domain sizes. However, there is an important caveat: for constant fluence (i.e. supposing we are limited by the sample damage threshold), the SHG signal to noise ratio scales linearly in the area excited by the probe, and thus SHG microscopes have a difficult time measuring small SHG signals compared to traditional SHG setups with a larger excitation area. To see this, let us say that our detector measures the number of photons per SHG pulse, which is proportional to the pulse energy  $U_p(2\omega)$ . Assuming the input and output pulse intensity profiles have the shape of a square wave with width  $\tau$  and height  $I_p(\omega)$  and  $I_p(2\omega)$ , respectively, we have

$$U_p(2\omega) = AI_p(2\omega)\tau \quad (3.1)$$

and

$$U_p(\omega) = AI_p(\omega)\tau \quad (3.2)$$

where  $A$  is the area of the beam at the sample surface. The SHG intensity is proportional to the square of the input intensity

$$I_p(2\omega) \propto I_p^2(\omega) \quad (3.3)$$

so that

$$U_p(2\omega) \propto \frac{U_p^2(\omega)}{A\tau}. \quad (3.4)$$

Substituting for the fluence  $f$

$$f(\omega) = \frac{U_p(\omega)}{A} \quad (3.5)$$

we have

$$U_p(2\omega) \propto \frac{f^2(\omega)A}{\tau} \quad (3.6)$$

i.e., if we hold the fluence constant at the sample damage threshold, the number of photons in the generated SHG pulse is proportional to the excitation area and inverse to the pulse width. The signal to noise ratio is then given by

$$\text{SNR} \propto \frac{U_p(2\omega)}{\sqrt{r}} \quad (3.7)$$

where  $r$  is the system repetition rate.

### 3.2.2 Oblique vs. normal incidence

While all of the results presented in this thesis utilized the setup in Fig. 3.1, where the incident beam makes a small angle with respect to the sample normal, plenty of groups use a different approach where that angle is set to  $0^\circ$ . This has the obvious disadvantage of not specifying all of the tensor elements, since any element  $\chi_{ijk}$  with  $i, j, k = z$  is not accessible in this geometry. However, in some cases this can actually be something of an advantage. For example, sometimes unwanted SHG contributions (see Section 2.2) may be avoided in the normal incidence geometry, assuming the numerical aperture (NA) of the focusing optic is small enough that longitudinal components of the electric field are nearly zero. Furthermore, in some materials the order parameter only couples to one or two elements of  $\chi_{ijk}$ ; if none of these elements have a  $z$  index, it is needless to complicate the analysis with oblique incidence.

In my experience, oblique incidence seems to be useful in two broad cases. For one thing, some order parameters only show up in the  $z$  components of  $\chi_{ijk}$  (this is the case in 1T-TaS<sub>2</sub>, see Chapter 5), in which case one obviously needs a nonzero angle of incidence to access these components. A more subtle point is that, even if in practice all of the phenomenology of a particular sample only shows up in the  $x$  and  $y$  indices of  $\chi_{ijk}$ , still one must measure the full tensor to *rule out* unseen

phenomenology in the other indices. Both the  $\text{CaMn}_2\text{Bi}_2$  (Chapter 6) and  $\text{CuBr}_2$  (Chapter 7) works presented in this thesis are examples of exactly this point, where the main scientific arguments involve either comparing SHG patterns in two domains or comparing oscillation amplitudes in different polarization channels. Clearly one needs to know all of the tensor elements to make those arguments exact.

### 3.2.3 Choice of detector

Our setup is somewhat unique in using a PMT for data collection rather than an electron multiplying charge coupled device (EM-CCD), which is the slightly more traditional method. Frankly, this decision was not based on the detection efficiency, but rather the fact that PMTs typically cost about two orders of magnitude less than EM-CCDs. However, the setup construction with a PMT is slightly different than with an EM-CCD, so you should probably decide which you want to use before you start building your setup. With an EM-CCD, the beam is sent into the device without focusing (L4 in Fig. 3.1) so that the beam traces a circle on the sensor as a function of time[? ]. The rotational anisotropy signal is read off by performing a radial integration of the camera image (after masking the part of the image which is outside from the circle traced by the beam). In this way, the rotation angle of the motor is correlated with the SHG signal via the azimuthal degree of freedom on the camera image. In contrast, with a PMT the SHG signal is read out as a function of time on an oscilloscope (see Section 3.1), and must be correlated with the rotation angle of the motor by some other method. We use an optical chopper wheel attached to the motor shaft; a beam from a laser pointer is directed through the chopper wheel and onto a photodiode, which produces a square wave signal that is used to trigger the oscilloscope. One must also be careful that the PMT is aligned as close to normal as possible to the axis defined by DM2 and L4 in Fig. 3.1, as the PMT output is actually quite sensitive to the angle of incidence of the input radiation.

As for the detection efficiency of the two devies, an EM-CCD is basically an *array* of PMTs—thus, there is no fundamental difference in the detection efficiencies of the two methods, although having never used an EM-CCD I cannot speak to any specific considerations that might favor one over the other.

## 3.3 tr-SHG: methodology

### 3.3.0.1 Polarization control

The main limitation for doing tr-SHG is simply that the experiment becomes longer. Each measurement of  $\chi_{ijk}$  requires averaging four different polarization channels ( $P_{\text{in}}P_{\text{out}}$ ,  $P_{\text{in}}S_{\text{out}}$ ,  $S_{\text{in}}P_{\text{out}}$ , and  $S_{\text{in}}S_{\text{out}}$ ), which, depending on the signal to noise ratio, can take as long as 2 – 3 minutes each. In a time-resolved experiment, that procedure must be repeated at least once for each time delay; in fact, it is often useful to sweep the delay stage multiple times to reduce the extent to which systematic drifts in the laser power, alignment, etc. affect the time trace. Not only is this time-consuming (typically taking  $\sim 12$  hours to get a good dataset), but it also requires four rotations of the polarizers at each delay, which is simply not feasible if the polarizers are to be rotated manually. Unfortunately, automated polarizer rotation is difficult in the RA-SHG experimental geometry because the polarizers must be rotated relative to a lens tube which is *itself* rotating at 5 Hz. The traditional method of rotating polarizers via stepper motor is thus not possible, unless one finds a method to transmit power between the stationary laboratory frame and the rotating frame that the polarizer lives in. Myself and Karna Morey designed such a method using an electronic device known as a hollow-bore electric slip ring, which uses ring-shaped conductive pads in combination with low-friction metallic brushes to conduct electricity between two rotating objects. In my opinion, such a design is essential to doing tr-SHG unless one is satisfied with only measuring a single polarization channel; thus, I have dedicated the entirety of Chapter 4 to our solution, which in my opinion represents the largest contribution we made to SHG methodology during this thesis.

### 3.3.0.2 The pump beam path

Having discussed the modifications needed for tr-SHG on the probe arm, let us now describe the pump beam path. 100 fs pulses from the regenerative amplifier (Spectra-Physics Spitfire Sptf-100f-5k-xp) are split by 90 : 10 beamsplitter (with the 10% becoming the probe beam, see Section 3.1) and are used as input to an OPA (Light Conversion TP8F1N3) which produces light of variable wavelength between 1100 and 2080 nm.

The output of the OPA is directed through a wire-grid polarizer (to pick out the signal or idler, as needed) to an optical delay line (Newport DL125 with SMC100 motion controller) and a second polarizer to vary the beam power. The beam then passes through a NIR (near-infrared) longpass filter to remove unwanted visible wavelengths that are output by the OPA. A 400 nm lens focuses the beam past two mirrors (one mounted with epoxy onto the focusing lens L3 of Fig. 3.1<sup>2</sup>) and finally onto the sample. The diameter of the pump beam at the focus is set by moving the lens position along the beampath and monitoring the beam shape with a CCD camera. The pointing of the beam is aligned so that the light reflected off the sample is perfectly backscattered. Pump scatter is avoided by mounting a small black circular disk in the center of L3, and by subtracting “dark” scans without the probe beam from the final dataset.

An optical chopper wheel is placed somewhere in the pump beam path which blocks every other pulse from the OPA, so that the effective repetition rate of the pump pulsetrain is 2.5 kHz. The output of the PMT (see Fig. 3.1) is sent to a lock-in amplifier synced to this frequency, so that the output of the lock-in is proportional to

$$I_{\text{Pump+Probe}}^{\text{SHG}} - I_{\text{Probe}}^{\text{SHG}} \quad (3.8)$$

i.e. the output of the lock-in is the pump-induced change in the measured SHG intensity.

Finally, the pump-probe time delay is varied, and for each delay the rotational anisotropy in the SHG intensity is measured in each of the four polarization channels. Alternatively, the motor rotation may be parked at a fixed angle and the SHG intensity at this angle measured as a function of delay time.

## 3.4 Data analysis

Finally, we discuss the analysis of SHG data, first in the static limit and then in the context of tr-SHG.

---

<sup>2</sup>Remember that the probe beam is arriving at oblique incidence and thus passes through the edge, rather than the center, of L3.

### 3.4.1 Static RA-SHG patterns

The typical static RA-SHG dataset consists of a set of points  $\{(\phi_n, I_n^p)\}$ ,  $n \in \{0, 1, \dots, N - 1\}$  and standard errors  $\{\sigma_n^p\}$  for each of the four independent polarization channels

$$p \in \{P_{\text{in}}P_{\text{out}}, P_{\text{in}}S_{\text{out}}, S_{\text{in}}P_{\text{out}}, S_{\text{in}}S_{\text{out}}\}.$$

By Eq. 2.13, each of these patterns may be modeled by an equation<sup>3</sup>

$$I^p(\phi) \propto |\hat{e}_i^{p,\text{out}}(\phi) \chi_{ijk} \hat{e}_j^{p,\text{in}}(\phi) \hat{e}_k^{p,\text{in}}(\phi)|^2, \quad (3.9)$$

where  $\hat{e}$  is a unit vector in the direction of the corresponding electric field. These unit vectors are given as a function of  $\phi$  and the angle of incidence  $\theta$  in table 3.1.

---

<sup>3</sup>I will focus on electric dipole SHG for now, although note that the equations for electric quadrupole and magnetic dipole SHG (Eqs. 2.23 and 2.24) are different—by Eq. 2.16, both involve a factor of the incident wavevector  $k$ , and the magnetic dipole term has a cross product.

Table 3.1: Vector definition of polarization channels.  $\theta$  is the angle of incidence and  $\phi$  is the angle of the plane of incidence with respect to the  $\hat{x}$  axis.

Input	Output	$\hat{e}^{\text{in}}(\phi)$			$\hat{e}^{\text{out}}(\phi)$		
		$\hat{e}_x^{\text{in}}(\phi)$	$\hat{e}_y^{\text{in}}(\phi)$	$\hat{e}_z^{\text{in}}(\phi)$	$\hat{e}_x^{\text{out}}(\phi)$	$\hat{e}_y^{\text{out}}(\phi)$	$\hat{e}_z^{\text{out}}(\phi)$
P	P	$\cos \phi \cos \theta$	$\sin \phi \cos \theta$	$-\sin \theta$	$-\cos \phi \cos \theta$	$-\sin \phi \cos \theta$	$-\sin \theta$
P	S	$\cos \phi \cos \theta$	$\sin \phi \cos \theta$	$-\sin \theta$	$-\sin \phi$	$\cos \phi$	0
S	P	$-\sin \phi$	$\cos \phi$	0	$-\cos \phi \cos \theta$	$-\sin \phi \cos \theta$	$-\sin \theta$
S	S	$-\sin \phi$	$\cos \phi$	0	$-\sin \phi$	$\cos \phi$	0

Let us assume that we know the point group  $P_G$  of our material. Then, the first step is to constrain the values of  $\chi_{ijk}$  using the arguments of Section 2.1. One can do this manually by solving the system of equations defined by Eq. 2.10, or one can simply look up the answer in one of a number of tables (e.g. [?])<sup>4</sup>; in the end we are left with a tensor  $\chi_{ijk}^{P_G}$  with  $M$  independent elements  $\{\chi_i, i \in 0, 1, \dots, M-1\}$ .

The goal is to simultaneously fit the four patterns  $\{(\phi_n, I_n^p)\}$  to Eq. 3.9 using the  $\chi_i$ 's. Our objective function is thus

$$f(\{\chi_i\}) = \sum_{p \in \{P_{\text{in}} P_{\text{out}}, P_{\text{in}} S_{\text{out}}, S_{\text{in}} P_{\text{out}}, S_{\text{in}} S_{\text{out}}\}} \sum_{n=0}^{N-1} \left( \frac{I^p(\phi_n) - I_n^p}{\sigma_n^p} \right)^2 \quad (3.10)$$

with  $I^p(\phi)$  defined in Eq. 3.9. Unfortunately, such a function is quite difficult to minimize. The reason is that  $I^p(\phi)$  is ultimately a sum of products of trigonometric functions of  $\phi$  (due to table 3.1) which can be difficult for typical minimization algorithms. An alternative is to cast the problem in terms of the Fourier transforms (FTs)

$$\hat{I}^p(k) \equiv \frac{1}{2\pi} \int_0^{2\pi} I^p(\phi) e^{-ik\phi} d\phi \quad (3.11)$$

of  $I^p(\phi)$  and the discrete Fourier transforms (DFTs)

$$\{(k, \hat{I}_k^p)\}, \quad (3.12)$$

of  $\{(\phi_n, I_n^p)\}$ , where<sup>5</sup>

$$\hat{I}_k^p \equiv \frac{1}{N} \sum_{n=0}^{N-1} I_n^p e^{-ik\phi_n}. \quad (3.13)$$

Since the DFT is unitary, the uncertainties  $\hat{\sigma}_k^p$  are simply the DFT of the  $\sigma_n^p$ 's. Thus, our new objective function is

$$f(\{\chi_i\}) = \sum_{p \in \{P_{\text{in}} P_{\text{out}}, P_{\text{in}} S_{\text{out}}, S_{\text{in}} P_{\text{out}}, S_{\text{in}} S_{\text{out}}\}} \sum_{k=0}^{N-1} \left( \frac{\hat{I}^p(k) - \hat{I}_k^p}{\hat{\sigma}_k^p} \right)^2. \quad (3.14)$$

---

<sup>4</sup>Be aware that these tensors are given in just one of many choices of coordinates; a rotation of  $\chi_{ijk}$  may be needed to agree with the orientation of the crystal in the experiment.

<sup>5</sup>I am assuming the  $\phi_n$ 's are equally spaced.

This is a much easier function to minimize for two reasons: one, the function is now just a quadratic function of the  $\{\chi_i\}$ 's, and two, since there are only six factors of trigonometric functions of  $\phi$  in  $I^p(\phi)$ ,  $\hat{I}^p(k) = 0$  for  $k \notin \{-6, -5, \dots, 6\}$ <sup>6</sup> (the other terms in Eq. 3.14 just contribute an overall constant to  $f$ ).

What is left then is just the choice of minimization algorithm. Unfortunately, simple gradient descent algorithms are not ideal here unless you have a really good initial guess, since Eq. 3.11 is still quadratic in the fitting parameters and the global minimum is often surrounded by many local minima which can easily cause these algorithms to become trapped. Global minimization routines are thus optimal; I have used the simulated annealing algorithm of [? ] with success, as well as the related “basinhopping” algorithm of [? ], both of which are implemented in `scipy.optimize[? ]`. Ultimately, though, it is up to the experimenter to ensure they have found the true global minimum of Eq. 3.14.

As part of this thesis, I wrote a software package in Python called ShgPy which uses `sympy[? ]` to compute the FT model Eq. 3.11 and `scipy.optimize[? ]` to fit this model to the data via Eq. 3.14. Installation instructions and a comprehensive documentation may be found at the project home page <https://bfichera.github.io/shgpy/>.

### 3.4.2 Modeling $\chi_{ijk}$ : the simplified bond hyperpolarizability model

Sometimes the symmetry-constrained  $\chi_{ijk}$  of Section 3.4.1 is difficult to analyze (perhaps it has too many fitting parameters), in which case it might be prudent try and justify an even more tightly constrained  $\chi_{ijk}$  via some a microscopic model. We have already seen two such models via Eqs. 2.37 and 2.41, but the former is typically not tractable and the latter may only be valid in the presence of a spontaneous symmetry-breaking phase transition with a well-defined order parameter. One alternative is to model the microscopic charge degrees of freedom classically—suppose most of the motion of charges in our solid occurs in the bonds between atoms, and that that motion is constrained to occur along the bond direction only. Then, the solid can be modeled as an ensemble of oscillating dipoles (one

---

<sup>6</sup>This is the case for electric dipole SHG; for electric quadrupole and magnetic dipole, we can have as much as  $k = \pm 8$ .

for each bond in the unit cell) with corresponding hyperpolarizabilities  $\{\alpha_n\}$ . Symmetry may dictate how many independent  $\alpha_n$ 's there are in the unit cell, but otherwise these are considered unknown and to be fit to the data. The electric dipole SHG response of such an ensemble was analyzed by [?], and the electric quadrupole response was later considered by [?]; the answer in both cases is quite simple:

$$\chi_{ijk}^{eee} = \sum_n \alpha_n b_i^n b_j^n b_k^n \quad (3.15)$$

$$\chi_{ijkl}^{gee} = \sum_n \gamma_n b_i^n b_j^n b_k^n b_l^n \quad (3.16)$$

where  $b^n$  is a unit vector in the direction of bond  $n$  and the  $\alpha_n$ 's and  $\gamma_n$ 's are the unknown parameters of the dipole and quadrupole models, respectively.

When valid, this simplified bond hyperpolarizability model (SBHM) is powerful for two reasons: for one, Eqs. 3.15 and 3.16 typically have fewer unknown parameters than the naive, symmetry-constrained tensor  $\chi_{ijk}^{PG}$  of Section 3.4.1, and two, there is a direct connection between the unknown parameters  $\alpha_n$  and  $\gamma_n$  and the microscopic degrees of freedom. One can thus draw conclusions *about* the microscopic degrees of freedom by fitting the SHG patterns to Eqs. 3.15 and 3.16 (see, e.g., [?]). Of course, one must be careful that the assumptions of this model—that the charges are localized to the bonds, and that the only relevant motion is along the bond direction—are actually correct before proceeding with this sort of analysis.

Myself and Karna Morey built a comprehensive interface to the SBHM in Python using `pymatgen`[?], which takes an arbitrary crystallographic information file (CIF) and calculates the relevant susceptibility tensors via Eqs. 3.15 and 3.16. The change to the susceptibility tensor induced by an elastic distortion mode ( $\chi_{ijk}(q)$ , where  $q$  is the mode amplitude) can be computed via integration with `ISODISTORT`[? ?]. See the package documentation (<https://github.com/morey18k/sbhm.git>) for examples and further information.

### 3.4.3 Fitting time traces in tr-SHG

As the final section of this chapter, let me remark on a few aspects of fitting time-domain signals that are not necessarily specific to SHG, but

are nevertheless essential for tr-SHG analysis.

Typically, in tr-SHG we plot the pump-induced change in the SHG intensity at a single angle  $\phi_0$  as a function of the delay time  $t$ ; more complicated analysis of the tensor elements themselves is possible but often unnecessary. This intensity change  $\Delta I_{2\omega}(t, \phi_0)$  is related to  $P(2\omega)$  via

$$\Delta I_{2\omega}(t, \phi_0) = I_{2\omega}^{\text{Pump+Probe}}(t, \phi_0) - I_{2\omega}^{\text{probe}}(0, \phi_0) \quad (3.17)$$

$$\propto |P_{2\omega}(0, \phi_0) + \delta P_{2\omega}(t, \phi_0)|^2 - |P_{2\omega}(0, \phi_0)|^2 \quad (3.18)$$

$$\propto 2P_{2\omega}(0, \phi_0)\delta P_{2\omega}(t, \phi_0) + |\delta P_{2\omega}(t, \phi_0)|^2 \quad (3.19)$$

where we have used that the signal is presumably independent of time if there is no pump pulse. When  $|\delta P_{2\omega}(t, \phi_0)| \ll |P_{2\omega}(0, \phi_0)|$ , this reduces to

$$\Delta I_{2\omega}(t, \phi_0) \propto P_{2\omega}(0, \phi_0)\delta P_{2\omega}(t, \phi_0). \quad (3.20)$$

The basic problem is then that we have a dataset

$$\{t_n, I_n\}, n \in \{0, 1, \dots, N - 1\} \quad (3.21)$$

with uncertainties  $\sigma_n$  which we wish to fit to some model, typically consisting of some (e.g. polynomial) background

$$b(t, \{b_k\}), k \in \{0, 1, \dots, K - 1\} \quad (3.22)$$

plus 1 to  $M$  damped harmonic oscillators

$$I(t, \theta) = \begin{cases} 0 & t < 0 \\ b(t, \{b_k\}) + \sum_{m=1}^M A_m e^{-t/\tau_m} \cos(2\pi f_m t + \psi_m) & t > 0 \end{cases}, \quad (3.23)$$

where  $\theta$  refers to the set of unknown parameters  $\{b_k\}$ ,  $\{A_m\}$ ,  $\{\tau_m\}$ ,  $\{f_m\}$ , and  $\{\psi_m\}$ . We wish to determine the model coefficients  $\theta$  by minimizing the objective function

$$f(\theta) = \sum_{n=0}^{N-1} \left( \frac{I(t_n, \theta) - I_n}{\sigma_n} \right)^2. \quad (3.24)$$

Various algorithms exist to find the minimum  $\theta_0$  of  $f$ ; the Levenberg-Marquardt (LM) algorithm [? ?] is known to have trouble with exponential functions, so it is recommended to do a Nelder-Mead search [?] first

and then use LM to refine the solution. These methods also report the uncertainties  $\{\sigma_i\}$  on each fitting parameter, basically by computing the curvature of the function  $f$  near  $\theta_0$  (which depends, among other things, on the data uncertainty  $\{\sigma_n\}$ ). Importantly, however, these uncertainties are only valid when  $f$  is a linear function of the model parameters near the minimum!<sup>7</sup> This is a point which is completely overlooked in the ultrafast condensed matter literature, even though there is really no reason that Eq. 3.24 should satisfy this criterion for typical uncertainty levels in pump-probe experiments.

The correct approach in this case is to note that the data set  $D_0 \equiv \{t_n, I_n\}$  is just one of many possible datasets  $D_0, D_1, D_2, \dots$  that we *could* have measured during our experiment.<sup>8</sup> If we could run the minimization procedure described above for each of these hypothetical datasets, we would end up with a whole distribution of model coefficients  $\theta_0, \theta_1, \theta_2, \dots$  from which our measurement  $\theta_0$  was just a single draw. The spread of this distribution (or, more precisely, the spread of the distribution  $\theta - \theta_{\text{true}}$ ) reflects exactly the quantitative uncertainty in our measurement of  $\theta$  that we would like to report.

Our goal, then, is to approximate this distribution by some method. One approach (which works when we have many observations  $\{t, I\}$  with the same  $t$ ) is called the nonparametric bootstrap[? ]. For each time  $t_n$ , let us say that we have a set of measured intensities  $\{I_m^n\}$ , with  $m \in \{1, 2, \dots, M_n\}$ . Then, we generate new hypothetical datasets  $\mathcal{D}_1, \mathcal{D}_2, \dots$  by (for each  $t_n$ ) drawing  $M_n$  items *with replacement* from the  $\{I_m^n\}$ 's. The fact that this new distribution of datasets is a faithful representation of the true distribution  $\{D_0, D_1, D_2, \dots\}$  is not obvious, but theoretical work by many authors (see [? ] for a review) has established that it is nevertheless true.

If we are confident that our model  $I(t, \theta)$  is, in fact, the true model (at least for some set of coefficients  $\theta_{\text{true}}$ ), then rather than using the dataset  $D_0$  to generate our hypothetical datasets, we can instead choose to use the model *itself*. The idea is to take our estimate  $I(t, \theta_0)$  and generate new datasets  $\{\mathcal{D}_m\}$  essentially by adding noise:

$$\mathcal{D}_m = \{(t_n, I(t_n, \theta_0) + N_n), n \in \{0, 1, \dots, N-1\}\}, \quad (3.25)$$

---

<sup>7</sup>Here, “near” means “in a neighborhood of size  $\sigma_i$ .

<sup>8</sup>The following discussion closely follows that of *Numerical Recipes*, chapter 15[? ].

for some random variable  $N_n$  which we put in by hand. This is called the parametric bootstrap, referring to the fact that we are estimating our true distribution  $\{D_0, D_1, D_2, \dots\}$  via the parameters  $\theta_0$ [? ]. In order for the distribution of  $\mathcal{D}_m$ 's to faithfully represent the true distribution  $\{D_0, D_1, D_2, \dots\}$ , obviously  $N_n$  needs to reflect the actual noise distribution of the experiment. Thankfully, in pump-probe experiments, we usually know this distribution—as long as we have enough points  $(t_n, I_n)$  with  $t_n < 0$ , we can estimate  $N_n$  with a normal distribution centered about 0 with variance  $\langle (I_n)^2 \rangle_{<0} - \langle I_n \rangle_{<0}^2$ , where  $\langle \cdot \rangle_{<0}$  means “average over points with  $t_n < 0$ .”

Once we have the hypothetical datasets  $\{\mathcal{D}_m\}$  (regardless of how we generated them), we proceed by estimating a  $\theta_m$  for each one using Eq. 3.24, and then plotting the distribution  $\{\theta_m - \theta_0\}$ ; the spread of this distribution tells us the uncertainties  $\sigma_i$  in each of our model coefficients. The important part is that these uncertainties are much more reflective of the true uncertainty in our measurement of  $\theta$  than the curvature of Eq. 3.24 near  $\theta_0$ , which we have argued is strictly incorrect in many cases.

## Chapter 4

---

### *Automated polarization rotation for multi-axis RA-SHG experiments*

#### **4.1 Preface**

This chapter is based on a manuscript intended for standalone publication and modified to fit the format of this thesis. It was coauthored by myself and Karna Morey (as co-first authors), along with Baiqing Lv, Zongqi Shen, and Nuh Gedik. Karna Morey and I initiated the project, designed and built the polarization rotators, performed the demonstration experiment, and wrote the paper. Baiqing Lv and Zongqi Shen contributed to the design and helped review the manuscript. Nuh Gedik supervised the project.

#### **4.2 Abstract**

RA-SHG is a nonlinear optical technique used to probe the symmetry of condensed matter systems. Measuring the dependence of the SHG susceptibility on one or more external parameters, notably strain, field, temperature, or time delay, is an extremely powerful way to probe complex phases of quantum materials. Experimentally, extracting maximal information about the SHG susceptibility tensor requires measurements of S and P polarized input and output combinations, which naturally involves the rotation of the polarizers during data collection. For multi-axis experiments, this has proved challenging since polarization rotation is typically done manually. Automating this process eliminates labor constraints, reduces uncertainty due to low-frequency noise, and expands the type of multi-axis datasets that can be collected; however, it is difficult due to geometrical constraints within the setup. In this work, we design and implement low-cost, high-fidelity automated polarization rotators

for use in multi-axis RA-SHG. These polarization rotators utilize an electrical slip ring to transfer power to the rotating RA-SHG optical setup as well as a miniature stepper motor to perform the polarization rotation. We demonstrate this automated system in time-resolved RA-SHG measurements in the non-centrosymmetric semiconductor GaAs. For the multi-axis measurements described above, this automated system permits data averaging over longer periods, vastly expedites data collection, and expands the setup measurement capability. This ultimately opens new frontiers in probing quantum materials using multiple tunable external parameters.

### 4.3 Introduction

Probing the structure of crystalline solids is essential to understanding their intrinsic functionalities. Traditionally, diffraction techniques based on the scattering of e.g. x-rays are used to determine this structure; however, these techniques predominantly measure the total electron density and are thus insensitive to long-range ordering of the valence electron subsystem. In contrast, nonlinear scattering techniques at optical frequencies like RA-SHG are sensitive rather to the total charge density, and thus offer a complementary view of the electronic, magnetic, and lattice properties of quantum materials [? ? ].<sup>1</sup>

Furthermore, due to the non-invasive nature of RA-SHG, it can also be used to investigate changes along one or more measurement axes, such as strain, field, pressure, temperature, or time delay. The phase diagram of quantum materials is heavily influenced by these independent variables, and thus, changes to the SHG response along such measurement axes are of great interest. For example, previous studies have used various continuous experimental parameters such as pressure [? ], time delay[? ], and magnetic field to investigate phase transitions in quantum materials. Such measurements can illuminate the roles that charge, spin, and thermal degrees of freedom play within quantum materials.

Second harmonic generation gleans microscopic information through the coupling of an order parameter to the second harmonic susceptibility tensor (at least a third-rank tensor with 18 independent components) [?

---

<sup>1</sup>In this paper, we discuss RA-SHG, although the results are fully generalizable to arbitrary harmonics, e.g. third harmonic generation.

[]. This tensor governs the relationship between the vector properties (i.e. polarization and intensity) of the incident radiation and the generated second harmonic, as shown in Eq. 4.1. The complexity of this tensor means that a significant amount of data is needed to fully resolve the tensor components, posing experimental challenges with data collection. The importance of resolving the tensor components can be seen by considering Neumann’s principle, which states that these tensors must be invariant under symmetry operations of the material’s point group, which constrains the tensors’ independent and nonzero elements [? ]. By measuring the intensity and polarization of the generated second harmonic radiation, RA-SHG provides information about these tensor elements and thus the underlying point group. When performing experiments with more than one measurement axis, the data constraints mentioned above can often be especially burdensome, limiting the type of experiments that can be performed using RA-SHG. Thus, new methods for collecting data efficiently for multi-axis RA-SHG experiments are incredibly important.

A more detailed understanding of the information that needs to be collected to fully resolve the second harmonic susceptibility can be seen by considering Fig. 4.1. Fig. 4.1 shows a schematic of an RA-SHG setup, where near-infrared light from the laser source enters at oblique incidence and is scattered off the front of the sample, generating blue light at the second harmonic frequency. To leading order, the measured second harmonic intensity is given by

$$I(\phi) = |E_i^{\text{out}}(\phi)\chi_{ijk}^{(2)\text{eee}}E_j^{\text{in}}(\phi)E_k^{\text{in}}(\phi)|^2, \quad (4.1)$$

where  $\phi$  is the azimuthal angle between the crystallographic axes and the plane of incidence,  $E^{\text{out}}$  and  $E^{\text{in}}$  are the polarization vectors of the outgoing and incoming light, respectively, and  $\chi^{(2)\text{eee}}$  is the SHG electric-dipole susceptibility tensor. For certain values of  $\phi$ , as shown in Fig. 4.1(a), the sample is symmetric with respect to the polarization axis of the incoming light; in this case, the second harmonic generation is constrained to be zero, whereas in general arbitrary angles give a non-zero second-harmonic response (see Fig. 4.1(b)). Neumann’s principle dictates that Eq. 4.1 captures the symmetry considerations shown in Fig. 4.1, i.e. the symmetries of the crystal are embedded into its nonlinear susceptibility tensor  $\chi^{(2)}$ .

These considerations demonstrate the necessity of measuring the full rotational anisotropy of the SHG response, as well as its dependence on

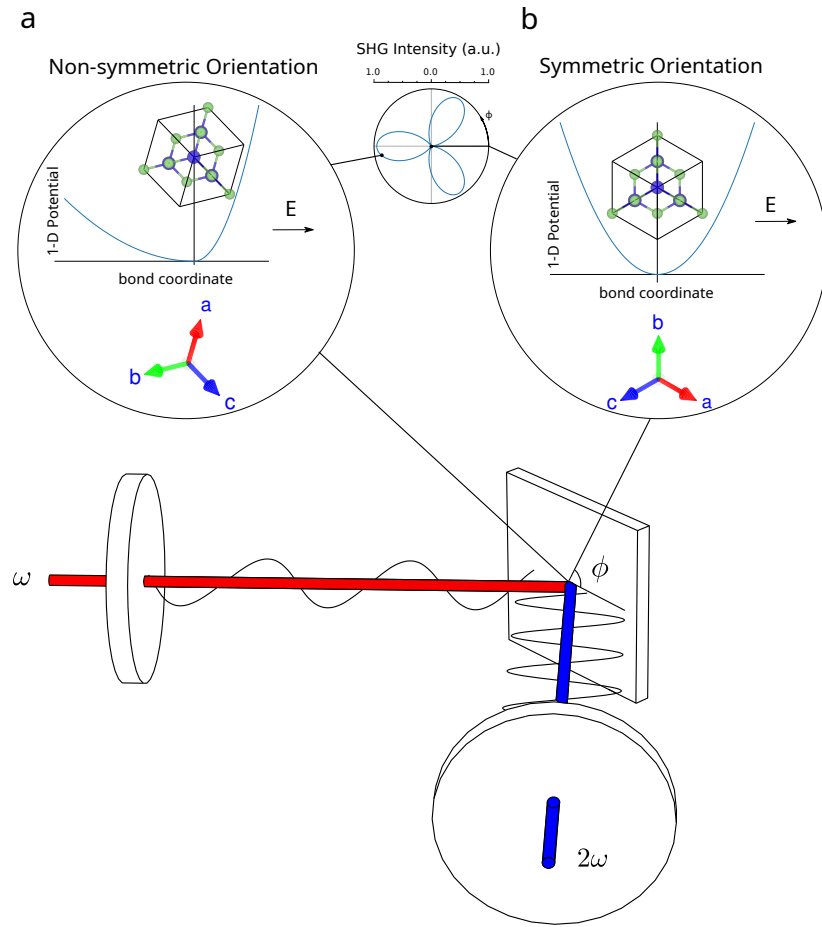


Figure 4.1: A demonstration of RA-SHG in the test sample GaAs. 800 nm light comes in at an oblique angle of incidence, after being passed through a polarizer. The polarization axis of the light is in the plane of incidence and is denoted in the insets of the figure with a black arrow. Depending on the angle of the plane of incidence relative to the crystallographic axes, as well as the polarization of the beam relative to that incoming plane of incidence, the second harmonic response to the stimuli should vary from zero points (nodes) to non-zero maxima.

the incoming and outgoing polarization directions (which may be P or S-polarized, leading to four independent polarization channels). The former requires rotating the plane of incidence, which is typically done by rotating the optical setup itself rather than the sample [? ? ? ? ]. The geometric constraints involved in rotating the optical setup make it challenging to use electromechanical components to rotate the polarizers shown in Fig. 4.1 between S and P configurations, since naively it is difficult to transfer power to the rotating frame of reference. Because of this, switching between different polarization channels is typically done manually, resulting in time and labor constraints that often limit data collection beyond a single polarization combination [? ]. Such constraints severely restrict the ability to infer tensor elements from the RA-SHG data and limit RA-SHG to studies involving often just a single tuning parameter.

Previous multi-axis RA-SHG studies typically either collected exclusively one polarization channel [? ] (for more than one axis) or simply sacrificed the quantity of collected data and therefore inferred statistics. However, these approaches can often miss certain features in RA-SHG data that would be apparent if more efficient data-taking methods were available. For example, phase transitions in which the order parameter couples differently to different polarization channels through the second harmonic susceptibility [? ] are best characterized by taking the full rotational anisotropy data. The benefit of collecting all four polarization combinations underscores the appeal of automated polarization control of RA-SHG setups.

In this work, we design and implement automated polarization rotators for use in multi-axis RA-SHG measurements. The devices utilize a miniature stepper motor housed in an electrical slip ring to circumvent the geometrical constraints imposed by the rotating plane of incidence. In section 4.5, we discuss the specific application of automated polarization rotation to time-resolved RA-SHG and show that it not only expedites data collection but also reduces the setup’s sensitivity to low-frequency noise. The advantages afforded by the automated polarization rotators exist not only for time-resolved measurements but for any measurements where an external parameter is being varied and compound rapidly as multiple parameters are varied at the same time.

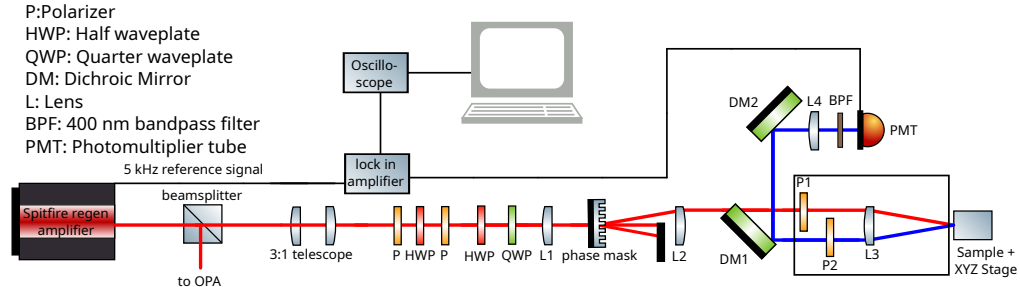


Figure 4.2: A diagram of the full second harmonic generation setup developed and described in [?]. Boxed in part of the setup shows the area of interest of this work, where the incoming and outgoing polarization channels are set.

## 4.4 Design

A detailed schematic of the RA-SHG setup is shown in figure 2. Telescopied pulses from a 5 kHz pulsed regenerative amplifier (Spectra-Physics Spitfire) are attenuated using a half-waveplate set between two polarizers and then elliptically polarized using a half-waveplate and quarter-waveplate in series. The light is then focused by a lens onto a rotating phase mask (which separates the beam into different diffraction orders), and a beam block selects the +1 order beam which is then collimated using another lens (L2). Finally, the beam passes through a dichroic mirror and a polarizer (P1) before being focused by a third lens (L3) onto the sample. The reflected radiation is passed through an analyzer (P2) and is redirected using a dichroic mirror periscope, which has equal reflectivity for S and P-polarized light and selects exclusively the 400 nm reflected radiation. The two polarizers (P1 and P2) and the phase mask are mounted on a rotating shaft coupled to an optical rotary encoder. After the dichroic mirrors, the second harmonic radiation is focused by a final lens (L4) onto a 400 nm bandpass filter and photomultiplier tube. The signal from the photomultiplier tube is sent to a lock-in amplifier synced to the 5 kHz pulsed laser reference signal and the amplified signal is then correlated with the signal from the optical rotary encoder using a home-built oscilloscope.

Importantly, the geometrical constraints introduced by the rotating plane of incidence mean that rotating P1 and P2 between S and P configurations electromechanically is challenging, as power must be transmitted

from the stationary laboratory frame to electrical components lying in the rotating frame.

To solve this problem, we utilize a hollow-bore electrical slip ring and a miniature stepper motor, shown in an exploded-view diagram in Fig. 4.3(a). A slip ring uses stationary conductive brushes sliding against a rotating through-bore cylinder to transfer power from a stationary reference frame to a rotating one, as shown in Fig. 4.3(b) [? ]. To accommodate the further requirement that the beams pass through the entire device unimpeded, we employ an 8 mm stepper motor that fits in between the two beams. Fig. 4.3(c) and Fig. 4.3(d) show a front view of the device, with the wire grid polarizer in the P and S positions, respectively, and the polarization direction of the polarizer shown in arrows on the edge of the polarizer. A full rendering, to scale, of the automated system within the full setup is shown in Fig. 4.4.

#### 4.4.1 Slip Ring

Slip rings are a standard electromechanical device for transferring power from a stationary assembly to a rotating assembly. An inner, rotating part of the slip ring can freely rotate relative to an outer, stationary part without compromising signal or power transmission. This functionality is enabled by low-friction metal brushes that slide against another set of electrical contacts, allowing free rotation while maintaining good electrical conductivity [? ], as shown in Fig. 4.3(b). To allow for the uninterrupted passage of the beams through the device, we use a hollow-bore slip ring (Moflon MT3899-S040-VD) whose 38 mm inner bore rotates along with the lens tube-pulley assembly shown in Fig. 4.4. Either set screws located on the front side of the slip ring (as shown in Fig. 4.3) or a 3D-printed cylindrical hollow bore adapter (not shown) can secure the inner bore of the slip ring to the lens tube.

#### 4.4.2 Miniature Stepper Motor

The hollow bore slip ring allows for the transfer of power to the rotating shaft. To rotate the wire grid polarizer between S and P configurations while also allowing both beams to pass through the entire device, we use an 8 mm diameter Faulhaber Series AM0820 stepper motor. The stepper motor's shaft is epoxied to a 1 inch square wire-grid polarizer

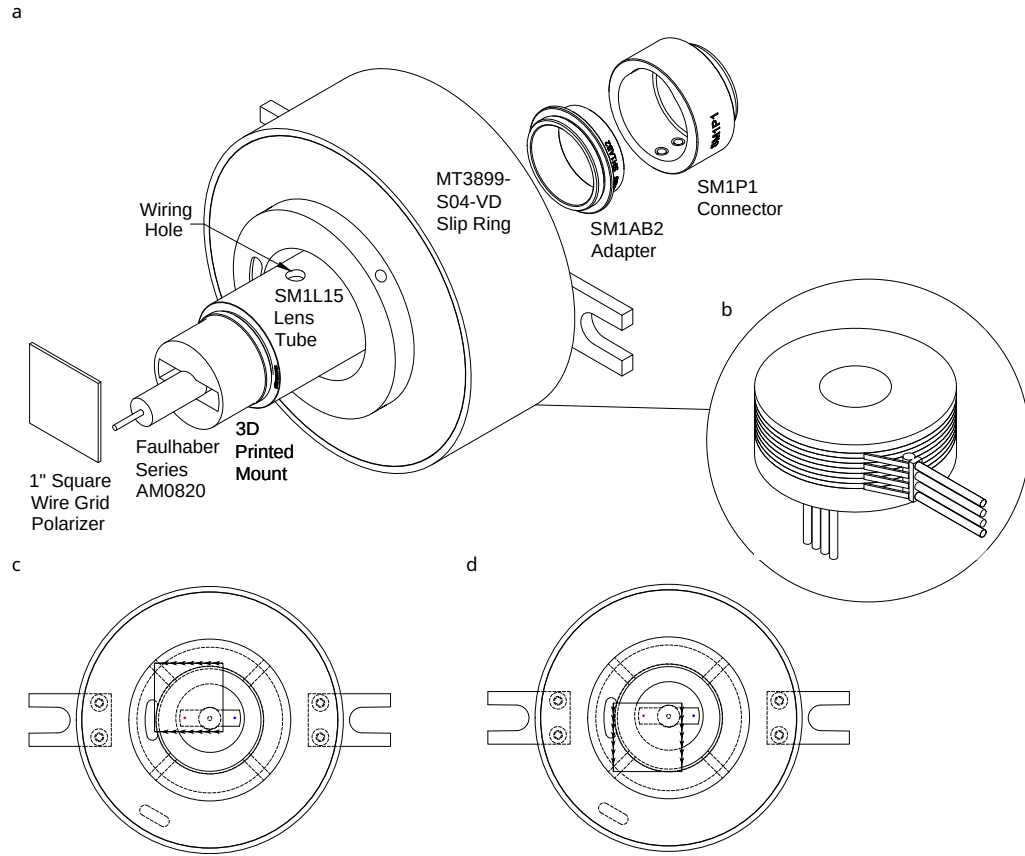


Figure 4.3: (a) An exploded-view diagram of one of the automated polarization rotators, with the individual components labeled. Each of these is a manufactured part except for the 3D-printed mount. (b) A schematic of the interior of an electrical slip ring, where low-friction metal brushes allow for electrical conduction across a rotating assembly. (c) A front view of the device, in the P-polarized state, with arrows on the edge of the polarizer indicating the polarization direction. (d) Same as Fig. 4.3(c), but in the S-polarized state.

roughly 5 mm from the closest horizontal and vertical edges, as shown in Fig. 4.3(c) and Fig. 4.3(d). The stepper motor is mounted in the center of the SM1L15 lens tube using a custom, 3D printed mount as shown in Fig. 4.3(a). This mount, along with careful epoxying of the polarizer to the motor shaft, ensures that the incidence angle of the beam is close to normal. Furthermore, the mount ensures that the stepper motor's shaft is aligned closely to the central rotation axis of the entire assembly, minimizing torques on the motor and polarizer. This stepper motor can support up to 800 total micro-steps per revolution ( $0.45^\circ$  per micro-step) and 0.65 mNm of holding torque, and is small enough to fit in between the incoming and outgoing beams.

The motor can then move the polarizer between the P configuration (Fig. 4.3(c)) and the S configuration (Fig. 4.3(d)) without manual intervention or the need to stop the rotation of the entire assembly. The offset placement of the polarizer on the motor shaft allows only one of the beams (either incoming or outgoing) to pass through the polarizer. The SM1AB2 and SM1P1 adapter pieces allow for arbitrary rotation relative to the longer lens tube-pulley assembly, allowing the beams to be aligned with the empty spaces in the stepper motor mount. These adapter pieces also allow for small ( $\pm 20^\circ$ ) rotations of the polarizer about the central axis to account for factory defects which may cause the polarization axis to be misaligned with the straight edges of the polarizer.

Another copy of the same system shown in Fig. 4.3 is mounted on the other side of the lens tube-pulley assembly and controls the polarization of the reflected beam, as shown in Fig. 4.4. The back sides of both devices, shown in Fig. 4.4, are attached to the rotating lens tube-pulley-motor-shaft assembly shown in Fig. 4.4 via threads on the long central lens tube. A hole drilled in the top and bottom of the SM1L15 piece in each device shown in figure Fig. 4.3(a) allows feedthrough wires to connect the four leads of the stepper motor to the four rotating inner-bore slip ring leads. The four leads on the stationary side of each slip ring directly connect to a Geckodrive G250X digital step driver for each device, controlled by a single Arduino Nano Every. This control circuit allows for the integration of the stepper motors with existing instrumentation software.

Whenever the stepper motors lose power, the polarizers need to be re-aligned due to the loss of their holding torque. The alignment is performed by using a reference polarizer with a known polarization axis. First, the plane of incidence of the entire assembly is positioned to the

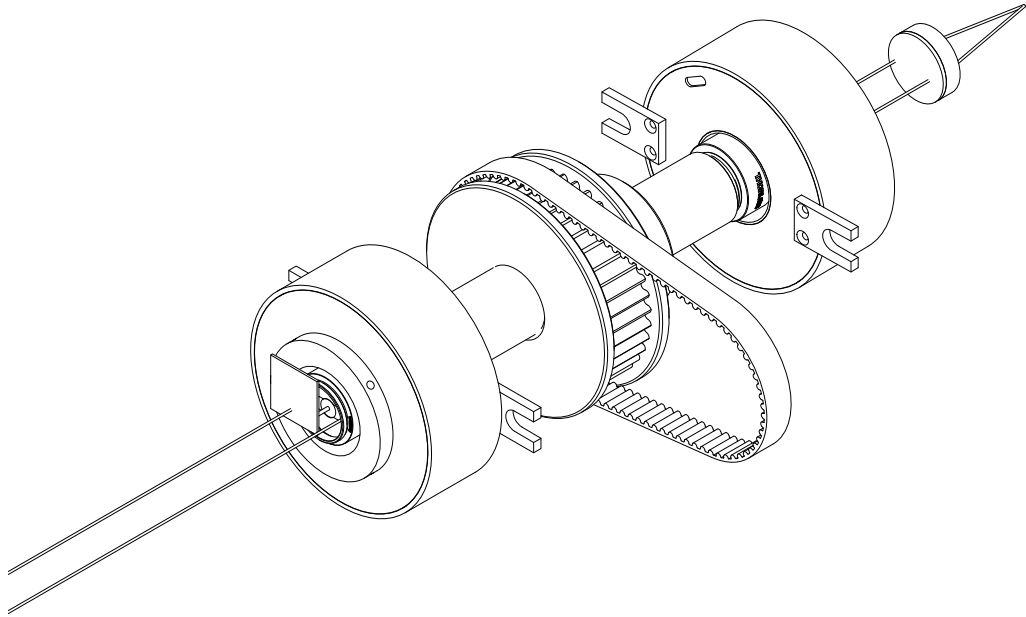


Figure 4.4: A 3-dimensional rendering of the boxed-in part of the setup in Fig. 4.2, with fully automated polarization rotators.

known polarization plane of the reference polarizer, then the polarizers themselves can be oriented by placing the beam through the reference polarizer and rotating the stepper motor until beam extinction (yielding an S-polarized alignment). The polarizers can then freely rotate between this S-polarized position and the orthogonal P-polarized position.

## 4.5 Validation and Discussion

To test these automated polarization rotators, we performed time-resolved RA-SHG on the non-centrosymmetric semiconductor GaAs [? ? ]. A pump line was added to the setup shown in Fig. 4.2 by mounting a  $45^\circ$  mirror onto L3 so that the pump beam may be reflected directly onto the sample. The pump pulse is produced by an optical parametric amplifier (Spectra-Physics Topas) tuned to a wavelength of  $1.3 \mu\text{m}$ . The pump line includes

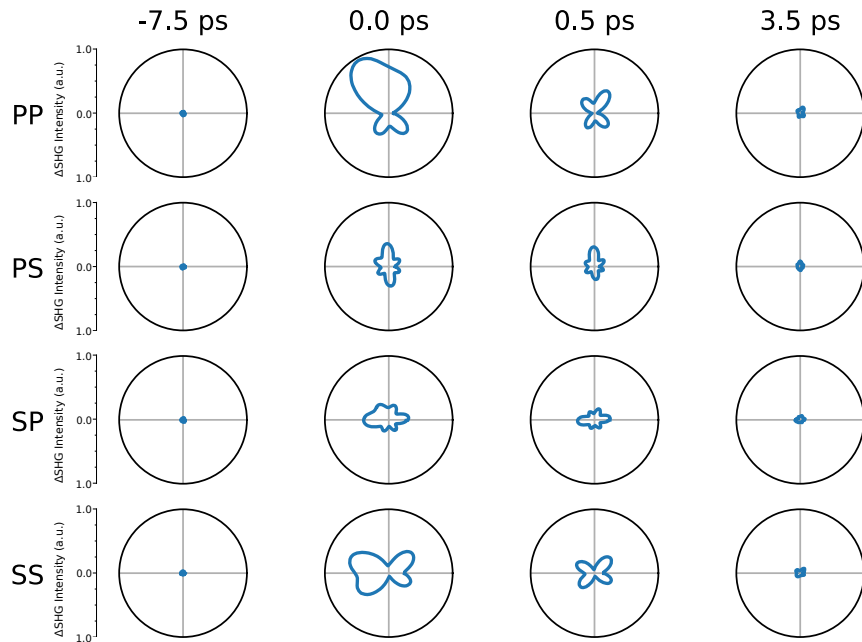


Figure 4.5: A polar plot of the change in SHG intensity (from the pre-pump state) as a function of time since zero-delay for the test sample GaAs. This is a demonstration of using the automated polarization rotators to take tr-SHG data. 55 different pump-probe delays (only four time delays are plotted) were taken in this dataset, meaning that 220 polarization rotations were performed using the automated polarizers.

a delay stage, which controls the relative time delay between the pump and the probe pulses, and a chopper wheel, which reduces the effective repetition rate of the pump pulses to 2.5 kHz. With the pump repetition rate of 2.5 kHz and the probe repetition rate of 5 kHz, locking in at a frequency of 2.5 kHz produces a signal proportional to the change in the SHG intensity relative to equilibrium. For time-resolved measurements on GaAs, shown in Fig. 4.5, 55 different pump-probe delays were taken, resulting in 220 different automatic rotations of the polarizers. The data in Fig. 4.5 shows the change in the SHG intensity relative to equilibrium as a function of the pump-probe delay, for each of the polarization channels. The use of the polarization rotators in this validation measurement demonstrates their functionality and broad utility for multi-axis RA-SHG measurements.

This system was also used to expedite data collection in recent studies of time-resolved, temperature-dependent RA-SHG [? ]. This particular type of RA-SHG measurement demonstrates the general advantages of automated polarization control in multi-axis RA-SHG measurements. To see this, note that if the rotation of the polarizers is performed manually, the best data-taking strategy involves taking the time dependence of one polarization channel in full before moving to the next. However, in the presence of low-frequency noise (due to e.g. fluctuations in the laser intensity), this is problematic as the different polarization channels will not be taken under equivalent conditions. In the automated case, in contrast, all polarization channels can be taken at each time delay. This greatly decreases the experiment’s susceptibility to low-frequency noise and expedites data taking by allowing for overnight and multi-day scans.

Automated polarization rotation thus vastly improves RA-SHG data collection, eliminating the need for manual polarization rotation, especially in cases of multiple experimental axes. The roughly 1.000 \$ total cost of both devices (not including polarizers) makes them relatively inexpensive, and the design is easily implementable in existing RA-SHG setups. Multi-axis measurements are becoming increasingly important to resolve complicated phase diagrams and competing orders, and thus future measurements will increasingly rely on automated systems such as the one presented in this work.

## Chapter 5

---

### *Second harmonic generation as a probe of broken mirror symmetry in 1T-TaS<sub>2</sub>*

#### 5.1 Preface

This chapter is based on a manuscript that was published as a Rapid Communication in *Physical Review B* in 2020, again modified to fit the format of this thesis. It was coauthored by myself, Anshul Kogar, Linda Ye, Bilal Gökce, Alfred Zong, Joseph G. Checkelsky, and Nuh Gedik. Anshul Kogar and I initiated the project and took the RA-SHG data. Linda Ye and Joseph G. Checkelsky grew the samples, Bilal G'oke helped build the RA-SHG setup, and Alfred Zong took some electron diffraction data. I analyzed the data and wrote the paper. Nuh Gedik supervised the project.

#### 5.2 Abstract

The notion of spontaneous symmetry breaking has been used to describe phase transitions in a variety of physical systems. In crystalline solids, the breaking of certain symmetries, such as mirror symmetry, is difficult to detect unambiguously. Using 1T-TaS<sub>2</sub>, we demonstrate here that RA-SHG is not only a sensitive technique for the detection of broken mirror symmetry, but also that it can differentiate between mirror symmetry-broken structures of opposite planar chirality. We also show that our analysis is applicable to a wide class of different materials with mirror symmetry-breaking transitions. Lastly, we find evidence for bulk mirror symmetry-breaking in the incommensurate charge density wave phase of 1T-TaS<sub>2</sub>. Our results pave the way for RA-SHG to probe candidate materials where broken mirror symmetry may play a pivotal role.

### 5.3 Introduction

In condensed matter systems, phases are often classified by the symmetries that they break. Identifying these symmetries enables one to understand a system's order parameter, collective excitations, topological defects, and allowable topological indices [? ? ]. Together, these attributes allow one to predict how a material will respond to external perturbations like electromagnetic fields, heat, and mechanical forces, which is a central goal of condensed matter physics.

Specifically, the presence or absence of mirror symmetry can lead to a variety of unusual phases and properties. For example, the absence of mirror plane symmetry in noncentrosymmetric materials can give rise to gyrotropic order, which can lead to a nonzero out-of-plane circular photo-galvanic effect [? ]. Moreover, in certain topological crystalline insulators, such as SnTe, the presence of mirror symmetry can give rise to conducting surface states through the existence of a nonzero mirror Chern number. This topological index guarantees an even number of Dirac cones on surfaces where mirror symmetry is retained [? ? ? ].

In other circumstances, like that in the pseudogap regime of cuprate superconductors, the existence of mirror symmetry is more controversial and has led some to seek an experimental method to serve as a binary indicator of broken mirror symmetry [? ]. In principle, several tools can already do this, including resonant ultrasound spectroscopy [? ? ], X-ray, neutron, and electron diffraction [? ? ], and a recently-proposed method, shear conductivity [? ]. Resonant ultrasound spectroscopy and the diffraction-based techniques are more sensitive to the ionic lattice, which makes the identification of subtle electronic symmetry-breaking challenging. And while shear conductivity has the potential to be an extremely versatile tool for identifying broken point group symmetries, experimental pursuits are currently only preliminary [? ]. In this study, we focus on a nonlinear optical technique, RA-SHG, which we show is capable not only of identifying broken mirror symmetry [? ] but also of resolving its sense (left- or right-handed). Furthermore, RA-SHG is sensitive to the electronic subsystem and can be used for microscopy studies, making it an ideal experimental tool for probing phase transitions where domains may arise [? ? ].

In this direction, we choose a material, 1T-TaS<sub>2</sub>, in which vertical mirror plane symmetry is manifestly broken across an incommensurate

(IC) to nearly commensurate (NC) CDW transition [? ? ]. Using this material, we demonstrate in this Rapid Communication that RA-SHG is an effective probe of broken mirror symmetry. We also show that the sense (i.e. left- or right-handed) associated with the mirror symmetry-broken structure is encoded in the angular dependence of the RA-SHG signal. Thus, RA-SHG can be used to differentiate mirror-opposite domains. While the data presented in this work is specific to the case of 1T-TaS<sub>2</sub>, we also show analytically that our technique is applicable to a wide class of transitions involving spontaneously broken mirror symmetry.

1T-TaS<sub>2</sub> is a layered material with a crystallographic structure identical to other octahedrally-coordinated transition metal dichalcogenides (Fig. 5.1(a)). The space group of the high temperature, undistorted phase is  $P\bar{3}m1$  (no.164, point group  $D_{3d}$ ) [? ], and the point group of the surface normal to the (001) direction in this phase is  $C_{3v}$  [? ? ]. Upon lowering temperature, 1T-TaS<sub>2</sub> undergoes a series of CDW transitions. At  $T_{IC} = 550$  K, a triple- $q$  IC CDW forms which breaks translational symmetry but retains the surface point group symmetries of the undistorted phase [? ? ]. The effects of the CDW on the bulk symmetries in this phase are not yet understood. On further cooling, at  $T_{IC-NC} = 353$  K there is a weak first-order transition to an NC CDW phase where three vertical mirror plane symmetries are broken [? ] and the surface point group becomes  $C_3$ . The NC phase has been visualized with scanning tunneling microscopy and exhibits patches of commensurate “Star of David” hexagrams that are separated by a network of discommensurations [? ]. Because mirror symmetry is broken, there are two energetically equivalent CDW configurations ( $\alpha$  and  $\beta$ ) in the NC phase that have opposite planar chirality (Figs. 5.1(c–d)). At even lower temperatures,  $T_{NC-C} = 184$  K, 1T-TaS<sub>2</sub> undergoes a symmetry-preserving first-order transition, where the discommensurations disappear and the CDW locks into a structure commensurate with the underlying lattice [? ].

Recent interest in the NC phase of 1T-TaS<sub>2</sub> has arisen due to the possibility of injecting mirror-opposite domains into the CDW structure [? ] which do not otherwise develop during the IC-NC transition. Zong *et al.* were able to induce these domains using a single ultrafast pulse of light, which was found to drive the material into a long-lived metastable state possessing domains of opposite planar chirality. Partly motivated by the desire to image these domains, we seek here a simple experimental method that could identify domains with opposite planar chirality.

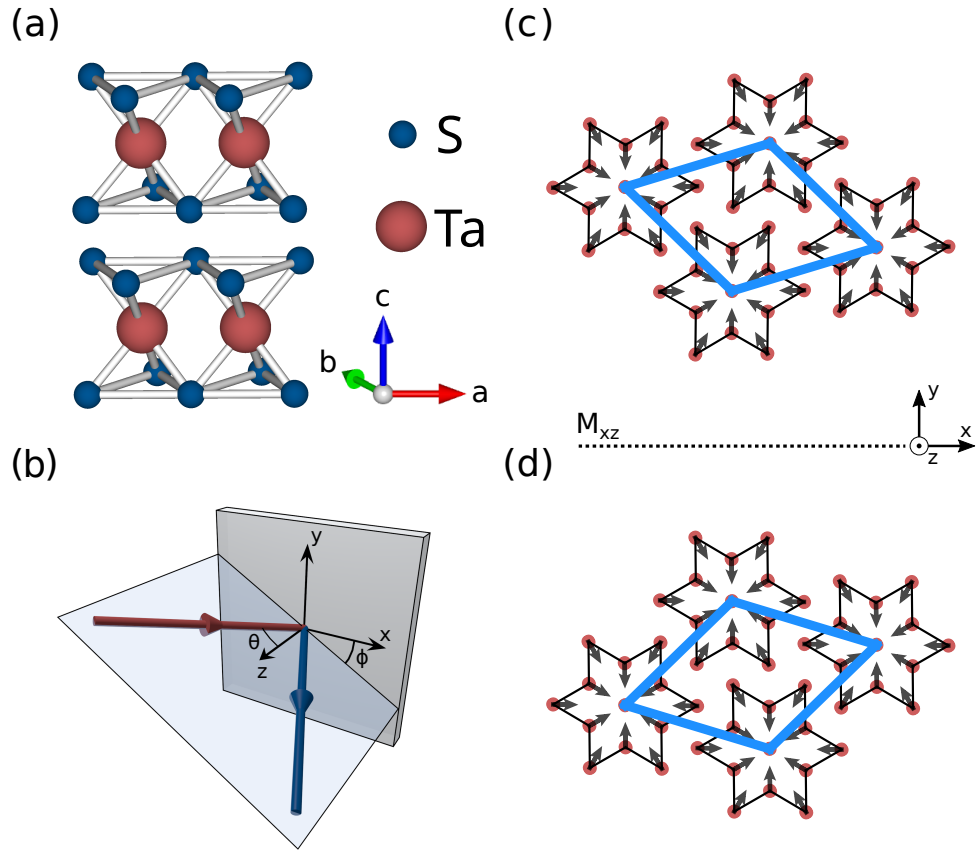


Figure 5.1: (a) Structure of 1T-TaS<sub>2</sub> in the undistorted phase. Ta and S atoms are depicted in red and blue, respectively. (b) Schematic of the experimental geometry. (c) (d) Structure of the CDW in the NC phase. Arrows denote the movement of the Ta atoms (red) below  $T_{\text{IC-NC}} = 353$  K from their undistorted positions. The transition at  $T_{\text{IC-NC}}$  spontaneously breaks mirror symmetry, so that two different CDW configurations ( $\alpha$  and  $\beta$ ) can form which have opposite planar chirality. The new unit cells of the two configurations are depicted in blue.  $M_{xz}$  denotes one vertical mirror plane which is broken beneath  $T_{\text{IC-NC}}$ . The others are related to  $M_{xz}$  by  $\pm 120^\circ$  rotation about the  $z$  axis.

## 5.4 Results and discussion

$1T\text{-TaS}_2$  samples used in the experiment were grown using the chemical vapor transport technique, as described in Ref. [? ]. We verified that the NC phase of  $1T\text{-TaS}_2$  was single-domain by performing electron diffraction on a sample from the same batch (see Section 5.7). This is in agreement with previous works [? ? ? ? ].

In RA-SHG [? ? ? ? ], a pulsed laser beam of frequency  $\omega$  and amplitude  $E(\omega)$  is focused onto a sample with nonzero angle of incidence  $\theta$  (Fig. 5.1(b)). The  $2\omega$  component of the radiation emitted by the sample is subsequently measured in various combinations of incoming and outgoing polarizations (either parallel (P) or perpendicular (S) to the plane of incidence) and as a function of the angle  $\phi$  between the plane of incidence and some crystallographic axis. In noncentrosymmetric materials, the response is dominated by the bulk electric dipole moment  $P_i(2\omega) = \chi_{ijk}E_j(\omega)E_k(\omega)$  [? ], where  $\chi_{ijk}$  is a material-specific susceptibility tensor which must be invariant under all symmetry operations present in the crystallographic point group. In centrosymmetric crystals such as  $1T\text{-TaS}_2$ , the bulk electric dipole response is forbidden [? ? ]. In this case, the dominant response often comes from the surface of the sample, which necessarily breaks inversion symmetry [? ]. SHG from surfaces of materials is described by a different susceptibility tensor,  $\chi_{ijk}^S$ , which is constrained by the crystal symmetries of the surface. In addition, there can be bulk contributions from higher-order processes which are allowed in the presence of inversion symmetry, such as the bulk quadrupole response  $Q_{ij}(2\omega) = \chi_{ijkl}^Q E_k(\omega)E_l(\omega)$  [? ? ]. Our experimental implementation uses a fast-rotation setup similar to that described in [? ] and [? ]. Here, we use an 800 nm (1.55 eV) laser beam incident at  $10^\circ$  with respect to the (001) sample normal. Further experimental details can be found in the supplement (see Section 5.7).

To show that we are sensitive to the breaking of mirror symmetry across the IC to NC transition, we took RA-SHG data on  $1T\text{-TaS}_2$  in both phases. Figs. 5.2(a) and 5.2(b) show the second harmonic response from the sample above and below  $T_{\text{IC-NC}} = 353$  K in two polarization channels, plotted as a function of  $\phi$ . We are able to fit the rotational anisotropy in the IC phase using the surface point group  $C_{3v}$  (Fig. 5.2(a)), which is in agreement with previous reports [? ? ]. It should be noted that in order to fit the  $S_{\text{in}}\text{-}S_{\text{out}}$  polarization channel appropriately, we find that

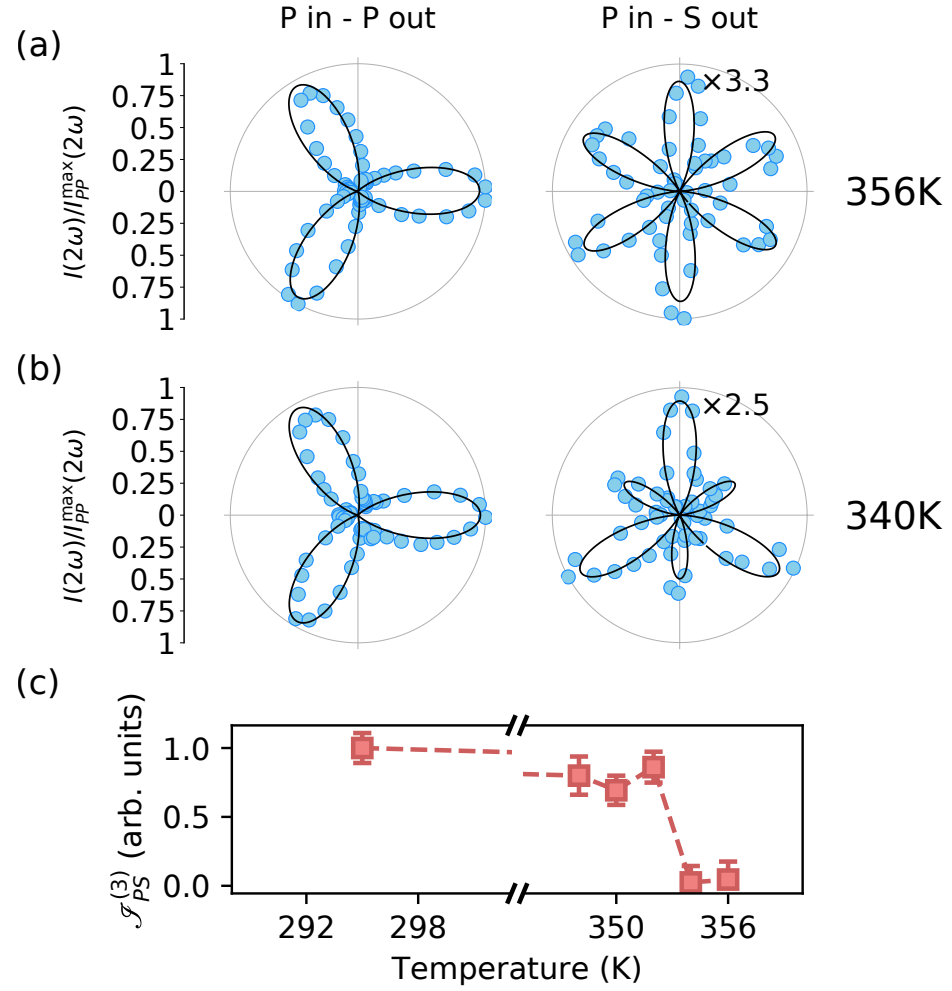


Figure 5.2: (a) (b) Second harmonic intensity from 1T-TaS<sub>2</sub> as a function of  $\phi$  above (Fig. 5.2(a)) and below (Fig. 5.2(b))  $T_{IC-NC} = 353$ K. For clarity, only two polarization channels are shown; the others are reproduced in the supplement (see Section 5.7). Solid lines in Fig. 5.2(a) and Fig. 5.2(b) are best fits to the data using the surface point groups  $C_{3v}$  and  $C_3$ , respectively. Data is normalized to the maximum value of the  $P_{in}-P_{out}$  signal for each temperature. (c) Temperature dependence of the third Fourier coefficient,  $\mathcal{I}_{PS}^{(3)}$ , of the intensity (see main text and Section 5.7 for details).

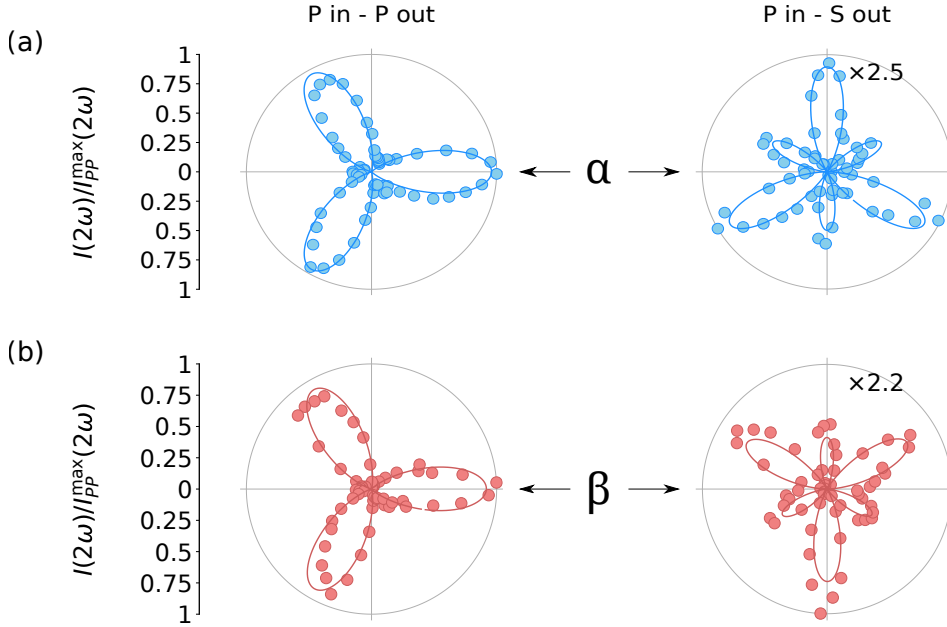


Figure 5.3: Second harmonic intensity as a function of  $\phi$  from mirror-opposite samples of 1T-TaS<sub>2</sub> in the NC phase ( $T = 340$  K). The labels  $\alpha$  and  $\beta$  refer to the two degenerate mirror-image configurations which are allowed in the NC phase. The solid line in (a) is a fit to the data using the surface point group  $C_3$ . The fit in (b) was generated by performing a mirror operation (see Section 5.7) to the numerical susceptibility tensor obtained from 5.3(a). Data is normalized to the maximum value in the P<sub>in</sub>-P<sub>out</sub> polarization channel for each sample.

it is necessary to add an additional bulk quadrupole contribution to the signal. The consequences of this contribution will be discussed later, but at the moment they do not affect our conclusions.

Upon cooling into the NC phase, mirror symmetry is spontaneously broken and the surface point group reduces to  $C_3$  [? ]. As a result, the RA-SHG exhibits a marked lowering of symmetry (Fig. 5.2(b)). This lowering of symmetry can be understood by noting that the  $\phi$  dependence

of  $I_{\text{PS}}(2\omega)$  under  $C_3$  is given by (see Section 5.7)

$$I_{\text{PS}}(2\omega) = (A_0 + A_1 \cos(3\phi) + A_2 \sin(3\phi))^2, \quad (5.1)$$

where  $A_0$ ,  $A_1$ , and  $A_2$  are functions of the susceptibility elements  $\chi_{ijk}^S$ .

Symmetry considerations (see Section 5.7) show that  $A_0$  and  $A_1$  vanish identically in the presence of mirror symmetry. The absence of these terms lead to the six-fold symmetry in the  $P_{\text{in}}-S_{\text{out}}$  channel and its alignment with the crystallographic axes as seen in Fig. 5.2(a). However, these terms can adopt nonzero values when mirror symmetry is broken. Below  $T_{\text{IC-NC}}$ , the RA-SHG intensity therefore exhibits a three-fold rather than six-fold symmetric pattern, arising from a nonzero  $A_0$ . The effect of a nonzero  $A_1$  is to rotate the RA-SHG intensity away from the high-symmetry axes, but we observe this coefficient to be zero within the resolution of our instrument. A negligible rotation of the SHG pattern should be expected, as the atomic positions of the Ta atoms only contract towards a central Ta atom and do not rotate away from their high symmetry axes to break the mirror symmetry (see Figs. 5.1(c)–d)).

The three-fold nature of the RA-SHG intensity can be quantified experimentally by performing a spectral (sine) decomposition of the intensity and extracting the third Fourier coefficient,  $\mathcal{I}_{\text{PS}}^{(3)}$ , of  $I_{\text{PS}}(2\omega)$  (see Section 5.7). Fig. 5.2(c) shows that  $\mathcal{I}_{\text{PS}}^{(3)}$  appears discontinuously below  $T_{\text{IC-NC}}$ , consistent with the first-order nature of the phase transition. Taken together, the above considerations confirm that  $\mathcal{I}_{\text{PS}}^{(3)}$  is a binary indicator of broken mirror symmetry in 1T-TaS<sub>2</sub>.

Having established that RA-SHG is sensitive to the breaking of vertical mirror plane symmetry in 1T-TaS<sub>2</sub>, we now seek to demonstrate that it can differentiate between CDW configurations of opposite planar chirality in the NC phase. To do so, we generate two samples with opposite planar chirality by cleaving a single sample of 1T-TaS<sub>2</sub>. We then perform RA-SHG on both sides of the same cleave. Referring to Figs. 5.1(c) and 5.1(d), cleaving the sample is equivalent to performing a 180° rotation about the  $x$ -axis, which in a single layer is equivalent to a mirror reflection about  $M_{xz}$ .

Fig. 5.3 shows the results of RA-SHG measurements in the  $P_{\text{in}}-P_{\text{out}}$  and  $P_{\text{in}}-S_{\text{out}}$  polarization channels as functions of  $\phi$ , where the two mirror images are labeled  $\alpha$  and  $\beta$ . As shown in the figure, whether the CDW configuration was  $\alpha$  or  $\beta$  is indicated in RA-SHG by the orientation (up

or down) of the pattern in the  $P_{\text{in}}-S_{\text{out}}$  channel, which is determined by the sign of  $A_0$  in Eq. 5.1 (see Section 5.7). This feature constitutes an experimental observable capable of identifying the sense associated with broken mirror symmetry in 1T-TaS<sub>2</sub>.

To validate the analysis contained above, we first fit the data for the  $\alpha$  structure using the surface point group  $C_3$  to generate a tensor  $\chi_{ijk}^{\alpha}$  with numerical coefficients. The fit is shown in Fig. 5.3(a). Then, we transform  $\chi_{ijk}^{\alpha}$  by a mirror reflection about  $M_{xz}$  to generate  $\chi_{ijk}^{\beta}$  (see Section 5.7); with this transformation, we find that the rotational anisotropy simulated using  $\chi_{ijk}^{\beta}$  collapses onto the measured signal, as shown in Fig. 5.3(b).

While the data contained in this work is specific to 1T-TaS<sub>2</sub>, the analysis is applicable to a variety of different phase transitions involving broken mirror symmetry. By understanding which Fourier coefficients of the SHG intensity adopt nonzero values in the low-symmetry phase, one can show that almost every structural phase transition involving broken mirror symmetry implies a measurable change in the symmetry of the SHG pattern (i.e. beyond a simple change in overall intensity). We have performed a symmetry analysis of all possible phase transitions involving spontaneously broken mirror symmetry and in each case identified the relevant experimental indicator(s). The results of this analysis can be found in the supplement (see Section 5.7).

The final observation of this work concerns the contribution from the bulk of the sample to the measured RA-SHG signal. As mentioned above, we find that in order to fit the data in the  $S_{\text{in}}-S_{\text{out}}$  polarization channel correctly, we need to introduce an additional bulk quadrupole contribution to the SHG signal. This contribution, which is described by the effective polarization  $\nabla_j Q_{ij} = 2i\chi_{ijkl}^Q k_j E_k E_l$ , is the next-lowest order contribution to SHG and is allowed in the presence of inversion symmetry [? ?]. Importantly, the quadrupole contribution is generated by the entire illumination volume and is therefore insensitive to the surface symmetry. Quadrupole SHG can be identified by examining the  $\theta$  dependence of the SHG intensity in the  $S_{\text{in}}-S_{\text{out}}$  channel. For purely electric dipole SHG, the symmetry in this channel does not depend on the incident angle. The  $\theta$  dependence depicted in Figs. 5.4(a) and 5.4(b) therefore establishes the presence of a quadrupole contribution in our signal.

According to diffraction measurements [? ], the correct surface and bulk point groups in the NC phase are  $C_3$  and  $S_6$ , respectively. Fig. 5.4(a)

shows our results in this phase, which are consistent with this assignment. To understand the three-fold symmetry in Fig. 5.4(a), we note that the  $\phi$  dependence of  $I_{\text{SS}}(2\omega)$  in this symmetry assignment is given by (see Section 5.7)

$$I_{\text{SS}}(2\omega) = (B_0 + B_1 \cos(3\phi) + B_2 \sin(3\phi))^2, \quad (5.2)$$

where  $B_1$  and  $B_2$  are functions of the susceptibility elements  $\chi_{ijk}^S$  and  $\chi_{ijkl}^Q$ , but  $B_0$  depends on  $\chi_{ijkl}^Q$  only (and is zero when the quadrupole contribution is ignored).  $B_0$  is then a probe of the bulk structure only and is not affected by the surface symmetry. When mirror symmetry is broken, all three coefficients are allowed and the function is three-fold symmetric as in Fig. 5.4(a).

However, symmetry considerations (see Section 5.7) show that  $B_0$  is zero in the presence of mirror symmetry. If bulk mirror symmetry were fully restored in the IC phase, we would therefore expect the signal to be six-fold symmetric. Fig. 5.4(c) shows that the RA-SHG instead remains three-fold symmetric in this phase, suggesting that the bulk breaks mirror symmetry. On the other hand, the highest-symmetry surface point group consistent with Figs. 5.2(a) and 5.4(c) is  $C_{3v}$ , which retains mirror symmetry. With RA-SHG, it is not possible to deduce the full crystal structure, but we speculate that this discrepancy between surface and bulk symmetries might be attributable to the particular stacking arrangement associated with the CDW above  $T_{\text{IC-NC}}$  (see Section 5.7). This would explain why the surface component, which is measuring the local structure at the surface of the sample [?], is consistent with the existence of mirror symmetry, whereas the bulk component, which measures the global structure of many layers, is not.

## 5.5 Conclusion

In summary, we have demonstrated here that RA-SHG can be used to identify broken mirror symmetry in crystalline materials. In addition, we have found that RA-SHG can differentiate between structural configurations related by mirror reflection. By considering the different symmetry constraints on the  $S_{\text{in}}\text{-}S_{\text{out}}$  channel, we have also shown that RA-SHG is sensitive to broken mirror symmetry in the bulk of 1T-TaS<sub>2</sub>, and have found evidence that the IC phase of this material breaks mirror symmetry

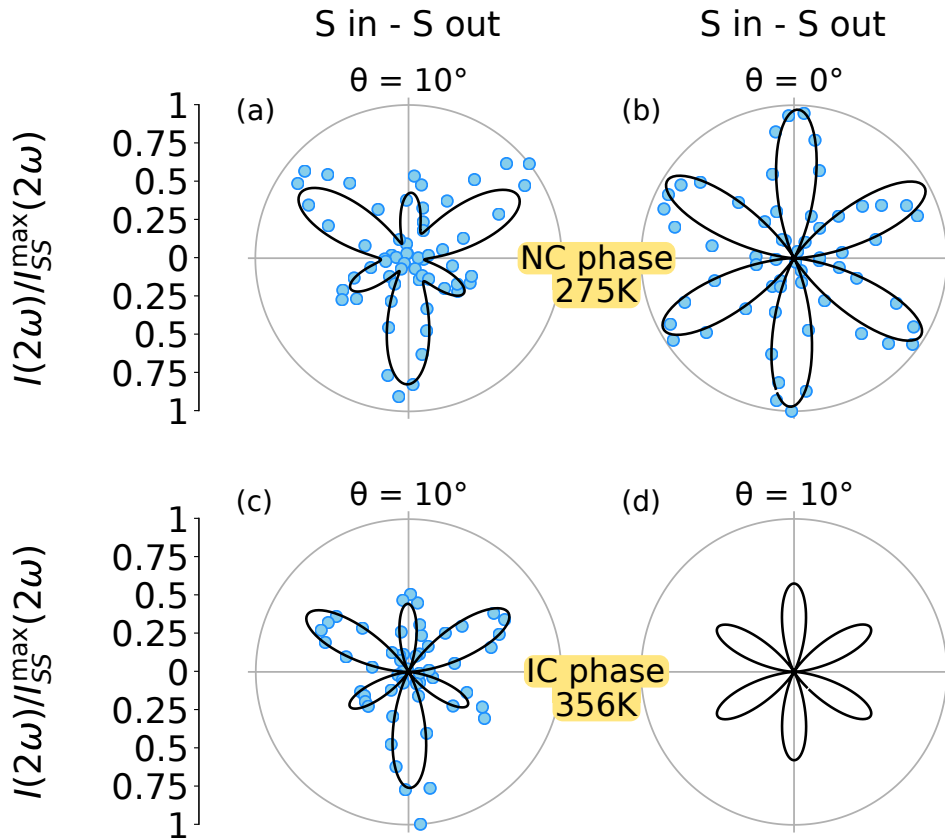


Figure 5.4: Second harmonic intensity as a function of  $\phi$  in the  $S_{in}$ - $S_{out}$  polarization channel. Temperatures, phases and incident angles ( $\theta$ ) are indicated on the figure. Also shown are fitting curves using the point group assignments (a)  $C_3$  surface and  $S_6$  bulk, (b)  $C_3$  surface and  $S_6$  bulk, (c)  $C_{3v}$  surface and  $S_6$  bulk. (d) Best fit to data in 5.4(c) using  $C_{3v}$  surface and  $D_{3d}$  bulk. Data in all plots was normalized to one for clarity. Other polarization channels are depicted in the supplement (see Section 5.7).

in the bulk. Importantly, our analysis is generalizable beyond the specific case of 1T-TaS<sub>2</sub>, and therefore opens up the possibility for RA-SHG to detect mirror symmetry-broken phases and their domain structures in other candidate materials.

## 5.6 Acknowledgments

We would like to thank Adrian Po and Liang Fu for helpful discussions regarding this work. This work was supported by the Gordon and Betty Moore Foundation’s EPiQS Initiative Grant GBMF4540 to NG (data analysis and manuscript writing) and Grant GBMF3848 to JGC (instrumentation), Shell through the MIT Energy Initiative (experimental setup and material development) and through DARPA DSO under DRINQS program grant number D18AC00014 (sample growth and data taking). L.Y. acknowledges support by the STC Center for Integrated Quantum Materials, NSF Grant No. DMR-1231319 and by the Tsinghua Education Foundation. B.G. gratefully acknowledges the German Academic Exchange Service (DAAD) for supporting his research stay with a fellowship.

## 5.7 Supplemental material

### 5.7.1 Probing broken mirror symmetry with RA-SHG

#### 5.7.1.1 Complete RA-SHG data

In the first section of the main text, we discuss how RA-SHG is sensitive to the breaking of mirror symmetry in 1T-TaS<sub>2</sub>. In Fig. 5.2 and Fig. 5.2(b) of the main text, we display RA-SHG data in two polarization channels: P<sub>in</sub>-P<sub>out</sub> and P<sub>in</sub>-S<sub>out</sub>. For completeness, the other polarization channels are reproduced in Fig. 5.5. Importantly, the fits in the figure only include a surface electric dipole contribution (see main text). The inability to fit the S<sub>in</sub>-S<sub>out</sub> polarization channel with a pure electric dipole contribution suggested to us that a second contribution was necessary in the form of a bulk electric quadrupole term. This is discussed in the main text as well as in Section 5.7.5.

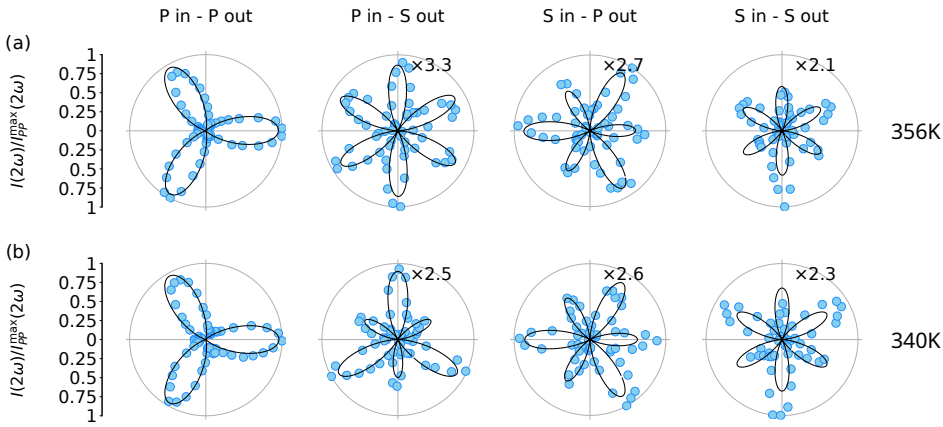


Figure 5.5: RA-SHG intensity as a function of  $\phi$  above (a) and below (b)  $T_{IC-NC} = 353K$ . Solid lines are best fits to the data using electric dipole SHG in the surface point groups  $C_{3v}$  and  $C_3$ , respectively. Data is normalized to the maximum value of the  $P_{in}-P_{out}$  signal for each temperature.

### 5.7.1.2 $\mathcal{J}_{PS}^{(3)}$ as an indicator of broken mirror symmetry

In the main text, we used the relation given by Eq. 5.1 to show that the breaking of sixfold symmetry in the  $P_{in}-S_{out}$  channel is consistent with the lowering of the surface point group from  $C_{3v}$  to  $C_3$  during the IC to NC phase transition. In this section, we show how Eq. 5.1 is derived.

Given any crystallographic point group, it is always possible to compute the form of the susceptibility tensor  $\chi_{ijk}^S$ . In  $C_3$ , the susceptibility

tensor is given by [?]

$$\chi_{ijk}^S = \begin{pmatrix} a & -b & c \\ -b & -a & -d \\ c & -d & 0 \\ \hline -b & -a & d \\ -a & b & c \\ d & c & 0 \\ \hline e & 0 & 0 \\ 0 & e & 0 \\ 0 & 0 & f \end{pmatrix}_{ijk} \quad (5.3)$$

for some  $a, b, c, d, e$ , and  $f$  which are dependent on the material. Here, the threefold axis is taken to be along the  $z$  direction. In the point group  $C_{3v}$ , the susceptibility tensor is constrained by symmetry so as to take a form which is the same as Eq. 5.3, but with  $b = d = 0$ , i.e.

$$\chi_{ijk}^S = \begin{pmatrix} a & 0 & c \\ 0 & -a & 0 \\ c & 0 & 0 \\ \hline 0 & -a & 0 \\ -a & 0 & c \\ 0 & c & 0 \\ \hline e & 0 & 0 \\ 0 & e & 0 \\ 0 & 0 & f \end{pmatrix}_{ijk} . \quad (5.4)$$

Here, the mirror planes are taken to be the  $xz$ -plane and those related to it by rotation about the  $z$ -axis through  $\pm 120^\circ$ .

To compute the RA-SHG intensity in the  $P_{\text{in}}-S_{\text{out}}$  channel, we consider a frame of reference in which the plane of incidence is held fixed and the sample is rotated about the optical axis. This reference frame is equivalent to that of the experimental setup (where the sample is fixed and the plane of incidence rotates), but it is easier to visualize and formulate mathematically. In this frame, the incoming  $P$ -polarized light at frequency  $\omega$  is parallel to the vector  $E_i(\omega) = (-\cos \theta, 0, \sin \theta)_i^T$ , and the outgoing  $S$ -polarized light which we wish to compute is parallel to the  $y$ -axis. The RA-SHG intensity in this channel is therefore given by

$$I_{PS}^{2\omega}(\phi) \propto |P_y^{2\omega}(\phi)|^2 \propto |\bar{\chi}_{yjk}^S(-\phi)E_j(\omega)E_k(\omega)|^2 , \quad (5.5)$$

where  $\bar{\chi}_{ijk}^S(\phi)$  is the susceptibility tensor corresponding to the sample when it has been rotated by an angle  $\phi$ . The relative sign in the argument of  $\bar{\chi}_{ijk}^S$  is due to the different reference frame used here compared to Fig. 5.1(b), where  $\phi$  is defined.

With the rotation matrix

$$R(\phi)_{ij} = \begin{pmatrix} \cos \phi & -\sin \phi & 0 \\ \sin \phi & \cos \phi & 0 \\ 0 & 0 & 1 \end{pmatrix}_{ij}, \quad (5.6)$$

$\bar{\chi}_{ijk}^S(\phi)$  is given by

$$\bar{\chi}_{ijk}^S(\phi) = R(\phi)_{il} R(\phi)_{jm} R(\phi)_{kn} \chi_{lmn}^S. \quad (5.7)$$

Substituting Eq. 5.7 into Eq. 5.5, we then have

$$I_{PS}^{2\omega}(\phi) \propto |R(-\phi)_{yl} R(-\phi)_{jm} R(-\phi)_{kn} \chi_{lmn}^S E_j(\omega) E_k(\omega)|^2. \quad (5.8)$$

With Eq. 5.3 as  $\chi_{ijk}^S$ , we arrive at Eq. 5.1 in the main text,

$$I_{PS}(2\omega) \propto (A_0 + A_1 \cos(3\phi) + A_2 \sin(3\phi))^2, \quad (5.9)$$

where

$$A_0 = 2d \sin(\theta) \cos(\theta), \quad (5.10)$$

$$A_1 = -b \cos^2(\theta), \quad (5.11)$$

and

$$A_2 = a \cos^2(\theta). \quad (5.12)$$

Since  $b = d = 0$  in  $C_{3v}$ , these equations show that  $A_0$  and  $A_1$  are zero in the presence of mirror symmetry, as cited in the main text. Furthermore, in  $C_{3v}$ , Eq. 5.9 reduces to

$$I_{PS}(2\omega) \propto A_2^2 \sin^2(3\phi), \quad (5.13)$$

which possesses sixfold rotational symmetry.

In the main text, we also remark that the breaking of sixfold rotational symmetry across the IC to NC phase transition can be quantified experimentally by performing a spectral (sine) decomposition of the measured intensity ( $I_{PS}^{2\omega}(\phi)$ ) and extracting the third Fourier coefficient, which we

called  $\mathcal{I}_{PS}^{(3)}$ . Here, we define  $\mathcal{I}_{PS}^{(3)}$  explicitly and show that it is present in 1T-TaS<sub>2</sub> only when mirror symmetry is broken.

The spectral decomposition for any given polarization channel ( $\Gamma_{in}$ - $\Gamma_{out}$ ) is defined formally by writing

$$I_{\Gamma_{in}\Gamma_{out}}^{2\omega}(\phi) = \sum_{n=0}^{\infty} \mathcal{I}_{\Gamma_{in}\Gamma_{out}}^{(n)} \sin \left[ n\phi + \psi_{\Gamma_{in}\Gamma_{out}}^{(n)} \right]. \quad (5.14)$$

This equation defines  $\mathcal{I}_{\Gamma_{in}\Gamma_{out}}^{(n)}$  and  $\psi_{\Gamma_{in}\Gamma_{out}}^{(n)}$  as the amplitude and phase of the  $n$ -fold Fourier component of the corresponding SHG intensity.

Using Eqs. 5.3, 5.8 and 5.14, we can then compute  $\mathcal{I}_{PS}^{(3)}$  and  $\psi_{PS}^{(3)}$  in the low temperature phase as

$$\mathcal{I}_{PS}^{(3)}(\chi_{ijk}^S) \propto 4\sqrt{C_1^2 + C_2^2} \quad (5.15)$$

and

$$\psi_{PS}^{(3)}(\chi_{ijk}^S) = \text{atan2}(C_1, C_2), \quad (5.16)$$

where

$$C_1 = -b \cdot d \sin \theta \cos^3 \theta, \quad (5.17)$$

$$C_2 = a \cdot d \sin \theta \cos^3 \theta, \quad (5.18)$$

$\theta$  is the angle of incidence, and

$$\text{atan2}(y, x) \equiv \begin{cases} \arctan\left(\frac{y}{x}\right) & x > 0 \\ \arctan\left(\frac{y}{x}\right) + \pi & y > 0, x < 0 \\ \arctan\left(\frac{y}{x}\right) - \pi & y < 0, x < 0 \\ +\frac{\pi}{2} & y > 0, x = 0 \\ -\frac{\pi}{2} & y < 0, x = 0 \\ \text{undefined} & x = y = 0 \end{cases}. \quad (5.19)$$

By comparing Eqs. 5.3 and 5.4, we find that

$$C_1 = C_2 = 0 \quad (5.20)$$

in the high temperature phase, so that  $\mathcal{I}_{PS}^{(3)}(\chi_{ijk}^S) = 0$ .

Note that Eq. 5.15 highlights an important aspect of our experiment, which is that  $\mathcal{I}_{PS}^{(3)}$  requires a nonzero angle of incidence to be observed.

This can be understood by noting that  $\mathcal{I}_{PS}^{(3)}$  is nonzero only when the tensor element  $\chi_{yxz}^S$  is nonzero. However, for such a term to be observable in the experiment, there needs to be an out-of-plane component to the incoming electric fields, which in turn requires a nonzero angle of incidence. Moreover, in a system with three-fold symmetry like 1T-TaS<sub>2</sub>, the aforementioned tensor element can only be nonzero in a system where mirror symmetry is absent. To see that this is true, consider the term  $P_y(2\omega) = \chi_{yxz}^S E_x(\omega)E_z(\omega)$ . Under an  $x \rightarrow -x$  mirror operation, we require that  $P_y \rightarrow P_y$ ,  $E_x \rightarrow -E_x$ ,  $E_z \rightarrow E_z$ , and  $\chi_{yxz}^S \rightarrow \tilde{\chi}_{yxz}^S$ . However, if this operation is a symmetry of the crystal then we have  $\tilde{\chi}_{yxz}^S = \chi_{yxz}^S$ , so that  $P_y = -P_y$ . This implies that  $\chi_{yxz}^S = 0$ . Therefore both a nonzero angle of incidence and broken mirror symmetry are required for a nonzero  $\mathcal{I}_{PS}^{(3)}$  in the geometry of our experiment.

### 5.7.2 Physical importance of the P<sub>in</sub>-S<sub>out</sub> channel

In this section we explain physically why the P<sub>in</sub>-S<sub>out</sub> polarization channel is the most sensitive to mirror symmetry breaking in 1T-TaS<sub>2</sub>. Consider the experimental geometry depicted in Fig. 5.6(a). A *P*-polarized electric field  $E_{in}$  is incident on a sample with vertical mirror symmetry about the *xz* plane (indicated by the sides A and B of the sample being the same color). The geometry is such that the plane of incidence makes an angle  $\phi$  with the reflection plane. Let  $\mathbf{P}_\perp(\phi)$  be the *S*-polarized component of the polarization resulting from second harmonic generation by the interaction of the sample with  $E_{in}$ .

Now consider applying the mirror operation both to  $E_{in}$  and to the sample (Fig. 5.6(b)). Then the resulting *S*-polarized component of the polarization (in the frame of the plane of incidence) will be  $-\mathbf{P}_\perp(\phi)$ . However, since the sides A and B in Fig. 5.6(b) are the same, by symmetry the problem is equivalent to Fig. 5.6(a) but with  $\phi$  replaced by  $-\phi$ . Thus  $\mathbf{P}_\perp(-\phi) = -\mathbf{P}_\perp(\phi)$ , implying that  $\mathbf{P}_\perp(0) = \mathbf{P}_\perp(\pi) = 0$ . This along with threefold rotational symmetry is sufficient to prove that the RA-SHG pattern from IC-phase 1T-TaS<sub>2</sub> in the P<sub>in</sub>-S<sub>out</sub> polarization channel is purely sixfold-symmetric. However, in the case where mirror symmetry is broken (Figs. 5.6(c) and 5.6(d)) the above argument no longer holds and the constraint  $\mathbf{P}_\perp(-\phi) = -\mathbf{P}_\perp(\phi)$  is relaxed. Therefore in 1T-TaS<sub>2</sub>,  $\mathcal{I}_{PS}^{(3)}$  is allowed in the NC phase but not in the IC phase.

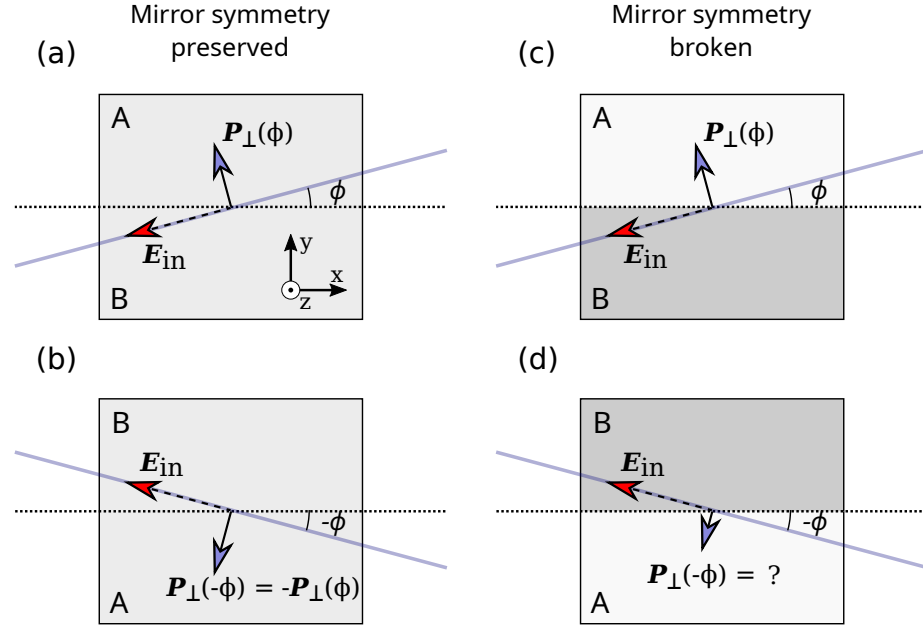


Figure 5.6: (a) Geometry referenced in showing that the  $P_{\text{in}}-S_{\text{out}}$  geometry is sensitive to the breaking of vertical mirror symmetry.  $E_{\text{in}}$  is the input electric field and  $\mathbf{P}_{\perp}$  is the  $S$ -polarized component of the polarization. The arrow identifying the direction of  $E_{\text{in}}$  is dashed to indicate that there is a component in the  $z$ -direction (out of the page). The solid blue and dotted black lines represent the plane of incidence and the mirror symmetry plane, respectively, which are in the  $z$ -direction and make an angle  $\phi$  with each other. The two halves (A and B) of the sample are the same color to indicate that mirror symmetry is present in this sample. (b) Mirror image of 5.6(a), showing that  $\mathbf{P}_{\perp}$  flips sign (when measured in the frame of the plane of incidence) under mirror reflection. (c) Same geometry as 5.6(a) with broken mirror symmetry, represented by the difference in color between sides A and B. (d) Mirror image of 5.6(c).

Initial group	Final group	Indicator(s)
$T_d$	$T$	None
$T_d$	$D_{2d}$	None
$T_d$	$C_{3v}$	None
$C_{6v}$	$C_{3v}$	$\mathcal{I}_{PP}^{(3)}, \mathcal{I}_{PP}^{(6)}, \mathcal{I}_{PS}^{(0)}, \mathcal{I}_{PS}^{(6)}, \mathcal{I}_{SP}^{(3)}, \mathcal{I}_{SP}^{(6)}, \mathcal{I}_{SS}^{(0)}, \mathcal{I}_{SS}^{(6)}$
$C_{6v}$	$C_{2v}$	$\mathcal{I}_{PP}^{(2)}, \mathcal{I}_{PP}^{(4)}, \mathcal{I}_{PS}^{(0)}, \mathcal{I}_{PS}^{(4)}, \mathcal{I}_{SP}^{(2)}, \mathcal{I}_{SP}^{(4)}$
$C_{6v}$	$C_6$	$\mathcal{I}_{PS}^{(0)}$
$C_{4v}$	$C_{2v}$	$\mathcal{I}_{PP}^{(2)}, \mathcal{I}_{PP}^{(4)}, \mathcal{I}_{PS}^{(0)}, \mathcal{I}_{PS}^{(4)}, \mathcal{I}_{SP}^{(2)}, \mathcal{I}_{SP}^{(4)}$
$C_{4v}$	$C_4$	$\mathcal{I}_{PS}^{(0)}$
$D_{3h}$	$C_{3h}$	$\psi_{PP}^{(6)*}, \psi_{PS}^{(6)*}, \psi_{SP}^{(6)*}, \psi_{SS}^{(6)*}$
$D_{3h}$	$C_{2v}$	None
$D_{3h}$	$D_3$	$\mathcal{I}_{PS}^{(3)}$
$C_{3h}$	$C_3$	$\psi_{PP}^{(1)*}, \psi_{PP}^{(2)*}, \psi_{PP}^{(3)*}, \psi_{PP}^{(4)*}, \psi_{PP}^{(5)*}, \psi_{PP}^{(6)*}, \psi_{PS}^{(1)*}, \psi_{PS}^{(2)*},$ $\psi_{PS}^{(3)*}, \psi_{PS}^{(4)*}, \psi_{PS}^{(5)*}, \psi_{PS}^{(6)*}, \psi_{SP}^{(1)*}, \psi_{SP}^{(2)*}, \psi_{SP}^{(3)*}, \psi_{SP}^{(4)*},$ $\psi_{SP}^{(5)*}, \psi_{SP}^{(6)*}, \psi_{SS}^{(2)*}, \psi_{SS}^{(4)*}, \psi_{SS}^{(6)*}$
$C_{3v}$	$C_3$	$\psi_{PP}^{(3)}, \psi_{PP}^{(6)*}, \mathcal{I}_{PS}^{(3)}, \psi_{PS}^{(6)*}, \psi_{SP}^{(6)*}, \psi_{SS}^{(6)*}$
$C_{3v}$	$C_{1h}$	$\mathcal{I}_{PP}^{(1)}, \mathcal{I}_{PP}^{(2)}, \mathcal{I}_{PP}^{(4)}, \mathcal{I}_{PP}^{(5)}, \mathcal{I}_{PS}^{(1)}, \mathcal{I}_{PS}^{(2)}, \mathcal{I}_{PS}^{(3)}, \mathcal{I}_{PS}^{(4)}, \mathcal{I}_{PS}^{(5)},$ $\mathcal{I}_{SP}^{(1)}, \mathcal{I}_{SP}^{(2)}, \mathcal{I}_{SP}^{(4)}, \mathcal{I}_{SP}^{(5)}, \mathcal{I}_{SS}^{(2)}, \mathcal{I}_{SS}^{(4)}$
$D_{2d}$	$S_4$	$\psi_{PP}^{(4)*}, \psi_{PS}^{(4)*}, \psi_{SP}^{(4)*}$
$D_{2d}$	$D_2$	$\mathcal{I}_{PS}^{(2)}$
$C_{2v}$	$C_2$	$\psi_{PP}^{(2)*}, \psi_{PP}^{(4)*}, \mathcal{I}_{PS}^{(2)}, \psi_{PS}^{(4)*}, \psi_{SP}^{(2)*}, \psi_{SP}^{(4)*}$
$C_{2v}$	$C_{1h}$	$\mathcal{I}_{PP}^{(1)}, \mathcal{I}_{PP}^{(3)}, \mathcal{I}_{PP}^{(5)}, \mathcal{I}_{PP}^{(6)}, \mathcal{I}_{PS}^{(1)}, \mathcal{I}_{PS}^{(2)}, \mathcal{I}_{PS}^{(3)}, \mathcal{I}_{PS}^{(5)}, \mathcal{I}_{PS}^{(6)},$ $\mathcal{I}_{SP}^{(1)}, \mathcal{I}_{SP}^{(3)}, \mathcal{I}_{SP}^{(5)}, \mathcal{I}_{SP}^{(6)}, \mathcal{I}_{SS}^{(0)}, \mathcal{I}_{SS}^{(2)}, \mathcal{I}_{SS}^{(4)}, \mathcal{I}_{SS}^{(6)}$

\* Measured from  $\pi/2$

Table 5.1: Indicators of broken mirror symmetry in mirror-symmetry-breaking transitions between noncentrosymmetric point groups. Values in the rightmost column (defined in Eq. 5.14) are zero in the initial group and nonzero in the final group. In all cases, the analysis was done in a geometry such that the sample normal is parallel to the broken mirror plane (i.e. the mirror plane is vertical).

In contrast to the  $S$ -polarized output ( $\mathbf{P}_\perp(\phi)$ ), the  $P$ -polarized output ( $\mathbf{P}_\parallel(\phi)$ ) does not change sign (as defined in the frame of the plane of incidence) under mirror reflection. Therefore the constraint for  $P$ -polarized output is that  $\mathbf{P}_\parallel(\phi) = \mathbf{P}_\parallel(-\phi)$ . Importantly, this constraint does not forbid Fourier components like  $\mathcal{I}_{PP}^{(3)}$  and  $\mathcal{I}_{SP}^{(3)}$ , even when mirror symmetry is present.

Finally, while the  $S_{in}$ - $S_{out}$  channel is subject to the constraint  $\mathbf{P}_\perp(-\phi) = -\mathbf{P}_\perp(\phi)$ , it can also be shown (see Section 5.7.5.2) that in the electric dipole regime,  $S_{in}$ - $S_{out}$  is twofold-symmetric regardless of the crystallographic point group. Therefore the  $P_{in}$ - $S_{out}$  polarization channel is especially sensitive to the breaking of vertical mirror plane symmetry in the geometry depicted in Fig. 5.6.

### 5.7.3 Generalization to other mirror symmetry-breaking transitions

While the argument above is effective in the case of a  $C_{3v}$  to  $C_3$  transition (as in 1T-TaS<sub>2</sub>), the presence or absence of other symmetries in different point groups may call for symmetry arguments which differ from those above. Therefore, to generalize this work we provide in table 5.1 a list of mirror-symmetry-breaking transitions between noncentrosymmetric point groups and identify corresponding terms (like  $\mathcal{I}_{PS}^{(3)}$  in 1T-TaS<sub>2</sub>) which adopt nonzero values in the low-symmetry phase. This table was generated using the same analysis as in Section 5.7.1.2 for 1T-TaS<sub>2</sub>. Note that while RA-SHG is only nonzero in noncentrosymmetric point groups, it can still be used in centrosymmetric materials because crystal surfaces necessarily break inversion symmetry.

In most of the transitions in table 5.1,  $\mathcal{I}_{PS}^{(n)}$  can be used as an indicator of broken mirror symmetry for some  $n$ . However, for others the RA-SHG pattern rotates rather than (or in addition to) changing symmetry, which is indicated by a change in the phase  $\psi_{\Gamma_{in}\Gamma_{out}}^{(n)}$  of certain Fourier components. Additionally, it should be observed that for a minority of the transitions in table 5.1, RA-SHG is not sensitive to the breaking of mirror symmetry (e.g. in the transition from  $T_d$  to  $T$ , two point groups for which the susceptibility tensor is equivalent).

## 5.7.4 Probing the sense of planar chirality with RA-SHG

### 5.7.4.1 Complete RA-SHG data

As in Section 5.7.1.1, for completeness we reproduce in Fig. 5.7 the RA-SHG data in the  $\alpha$  and  $\beta$  CDW configurations, including the two polarization channels which were truncated from Fig. 5.3 in the main text. The poor fit in the  $S_{\text{in}}\text{-}S_{\text{out}}$  polarization channel again indicated to us that there was an additional bulk quadrupole contribution to the signal.

### 5.7.4.2 Electron diffraction confirming the sample is single domain

To confirm that 1T-TaS<sub>2</sub> is single-domain in the NC phase, we performed electron diffraction on a sample from the same batch as the one used for the RA-SHG measurements. The absence of CDW sister peaks in Fig. 5.8 demonstrates that the sample is single-domain, in agreement with previous reports [? ? ? ?]. The thickness of the sample measured by electron diffraction was  $\sim 80$  nm, which is approximately equal to the penetration depth of 1T-TaS<sub>2</sub> at 800 nm [?]. We note that recent studies have demonstrated that it is possible to inject mirror domains into an otherwise uniform sample of 1T-TaS<sub>2</sub> using intense pulses of light [?]. To control for this effect, we used an incident fluence of 1.4 mJ/cm<sup>2</sup> which is well below the threshold fluence 5 mJ/cm<sup>2</sup> reported in [?].

### 5.7.4.3 Fitting RA-SHG data in the $\alpha$ and $\beta$ configurations

To fit the data in Fig. 5.3 of the main text, we performed the following procedure. First, we used the six independent elements in the  $C_3$  susceptibility tensor given by Eq. 5.3 as fitting parameters to fit the data on the  $\alpha$  sample (Fig. 5.7(a)) to

$$|P_i(\phi)|^2 \propto |R(-\phi)_{il}R(-\phi)_{jm}R(-\phi)_{kn}\chi_{lmn}^S E_j(\omega)E_k(\omega)|^2. \quad (5.21)$$

The fit was constrained in such a way as to forbid large changes in the susceptibility elements that exist in both phases (i.e.  $a$ ,  $c$ ,  $e$ , and  $f$ ). This gave us a set of six numbers  $\{\chi_{ijk}^\alpha\}$ , from which we can form the tensor  $\chi_{ijk}^\alpha$ . The cleaving operation can be represented by the operator  $\mathcal{C} = A\Gamma(\gamma)\hat{R}_x$ ,

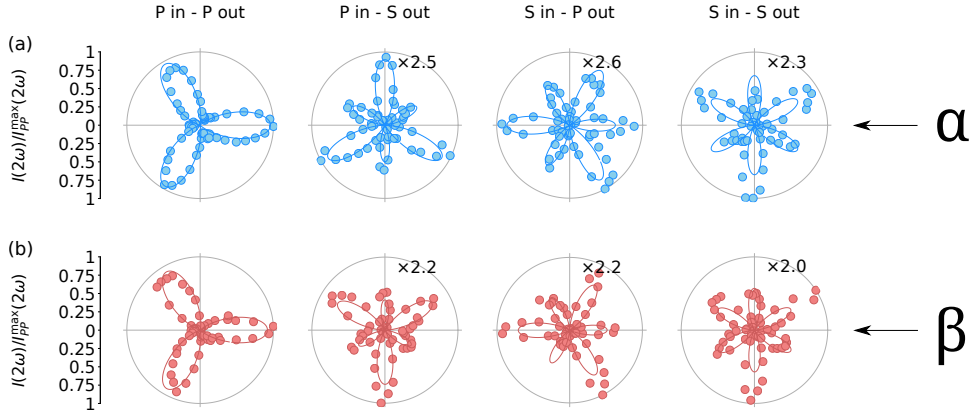


Figure 5.7: Second harmonic intensity as a function of  $\phi$  from two samples of 1T-TaS<sub>2</sub> in the NC phase ( $T = 340K$ ). The labels  $\alpha$  and  $\beta$  refer to the two degenerate mirror-image configurations which can exist in the NC phase. The solid line in (a) is a fit to the data using the surface point group  $C_3$ . The fit in (b) was generated by performing a mirror operation (see Section 5.7.4.3) to the numerical susceptibility tensor obtained from 5.7(a). Data is normalized to the maximum value in the P<sub>in</sub>-P<sub>out</sub> polarization channel for each sample.

where  $R_x$  is the operator which rotates the sample 180° about the  $x$ -axis,

$$R_x = \begin{pmatrix} 1 & 0 & 0 \\ 0 & -1 & 0 \\ 0 & 0 & -1 \end{pmatrix}, \quad (5.22)$$

$\Gamma(\gamma)$  is the operator which rotates the sample about the  $z$ -axis by an arbitrary angle  $\gamma$ ,

$$\Gamma(\gamma) = \begin{pmatrix} \cos \gamma & -\sin \gamma & 0 \\ \sin \gamma & \cos \gamma & 0 \\ 0 & 0 & 1 \end{pmatrix}, \quad (5.23)$$

and  $A$  is a positive overall constant which represents minor, day-to-day fluctuations in experimental conditions. If we were able to cleave the sample exactly along the high-symmetry axis, then  $\gamma$  would be 0° and

$\Gamma(\gamma)$  would be identity. Also note that the fact that the determinant of  $\mathcal{C}$  in the  $(x, y)$  subspace is  $-1$  is equivalent to the statement that  $\mathcal{C}$  switches the planar chirality of the sample.

To simulate the effect of cleaving the sample, we therefore applied  $\mathcal{C}$  to  $\chi_{ijk}^\alpha$  to form  $\chi_{ijk}^\beta(\{\chi_{ijk}^\alpha\}, \gamma, A)$ . Formally, this amounts to computing

$$\chi_{ijk}^\beta(\{\chi_{ijk}^\alpha\}, \gamma, A) = \mathcal{C}_{il}(\gamma, A)\mathcal{C}_{jm}(\gamma, A)\mathcal{C}_{kn}(\gamma, A)\chi_{lmn}^\alpha. \quad (5.24)$$

Now,  $\chi_{ijk}^\beta(\{\chi_{ijk}^\alpha\}, \gamma, A)$  is a function of only two free parameters ( $\gamma$  and  $A$ ). We find that with the proper choice of  $\gamma$  and  $A$ , the signal computed with  $\chi_{ijk}^\beta$  collapses onto the data in Fig. 5.7(b).

By applying  $R_x$  to the tensor given in Eq. 5.3, one can see that the effect of cleaving the sample is to flip the sign of  $b$  and  $d$ . By examining Eqs. 5.9–5.12, and noting that  $A_1 \approx 0$  within the resolution of our instrument, we see that this reproduces the change of the orientation of the RA-SHG pattern in the  $P_{in}$ - $S_{out}$  channel depicted in Fig. 5.3 of the main text.

## 5.7.5 Bulk broken mirror symmetry in 1T-TaS<sub>2</sub>

### 5.7.5.1 Complete RA-SHG data at $T = 295K$

As in Section 5.7.4.1, for completeness we reproduce in Fig. 5.9 the RA-SHG data at  $T = 295K$  (NC phase) which is used in Fig. 5.4 to argue that there is a nonzero bulk electric quadrupole component to the measured signal. Furthermore, we reproduce in Fig. 5.10 the RA-SHG data at  $T = 356K$  (IC phase) to show that we can fit all four polarization combinations using the surface point group  $C_{3v}$  as well as a bulk point group  $S_6$ , which is the highest-symmetry subgroup of the undistorted point group which breaks mirror symmetry (see below). The  $S_{in}$ - $S_{out}$  channel of Fig. 5.10 is shown in Fig. 5.4 of the main text.

### 5.7.5.2 Symmetry analysis of RA-SHG data

In the last section of the main text, we used the relation given by Eq. 5.2 to argue that the breaking of sixfold symmetry in the  $S_{in}$ - $S_{out}$  polarization channel indicates that bulk mirror symmetry is broken in the IC phase of 1T-TaS<sub>2</sub>. Here we derive Eq. 5.2 as we did Eq. 5.1 in Section 5.7.1.2.

As mentioned in the main text, the effective polarization for bulk electric quadrupole SHG is given by [? ? ]

$$\nabla_j Q_{ij} = 2i\chi_{ijkl}^Q k_j E_k E_l, \quad (5.25)$$

so that the total intensity in the S<sub>in</sub>-S<sub>out</sub> channel (including surface electric dipole) is given by

$$I_{SS}^{2\omega}(\phi) \propto \left| \left( \bar{\chi}_{yjk}^S(-\phi) + 2i\bar{\chi}_{ypjk}^Q(-\phi)k_p \right) E_j(\omega) E_k(\omega) \right|^2, \quad (5.26)$$

where

$$\bar{\chi}_{ijk}^S(\phi) = R(\phi)_{il} R(\phi)_{jm} R(\phi)_{kn} \chi_{lmn}^S, \quad (5.27)$$

$$\bar{\chi}_{ipjk}^Q(\phi) = R(\phi)_{il} R(\phi)_{pq} R(\phi)_{jm} R(\phi)_{kn} \chi_{lqmn}^Q, \quad (5.28)$$

and  $E_i(\omega) = (0, 1, 0)_i^T$ .

In the NC phase of 1T-TaS<sub>2</sub>, the appropriate assignment for the surface and bulk point groups is given by diffraction measurements [? ] to be  $C_3$  and  $S_6$ , respectively. Therefore for  $\chi_{ijk}^S$  we use the tensor defined by Eq. 5.3, and for  $\chi_{ijkl}^Q$  we use the tensor given in [? ] for the point group  $S_6$  (which for the sake of brevity we do not reproduce here). With these tensors, we then have

$$I_{SS}(2\omega) \propto (B_0 + B_1 \cos(3\phi) + B_2 \sin(3\phi))^2, \quad (5.29)$$

with

$$B_0 = \chi_{xyxx}^Q \sin \theta, \quad (5.30)$$

$$B_1 = \chi_{yyy}^S - \chi_{xzxy}^Q \cos \theta, \quad (5.31)$$

and

$$B_2 = -\chi_{xxx}^S + \chi_{xzgy}^Q \cos \theta. \quad (5.32)$$

Importantly, if bulk mirror symmetry were restored in the IC phase we would have  $\chi_{xyxx}^Q = \chi_{xzxy}^Q = 0$ , and therefore  $B_0 = 0$ . This can be checked by inspecting the quadrupole susceptibility tensor for the undistorted bulk point group  $D_{3d}$  (which preserves vertical mirror symmetry) defined in [? ].

Since  $B_0 = 0$  if the pattern possesses sixfold rotational symmetry (as can be seen by taking  $\phi \rightarrow \phi + 60^\circ$ ), we have that the breaking of sixfold rotational symmetry in the RA-SHG pattern (Fig. 5.4(c) of the main text)

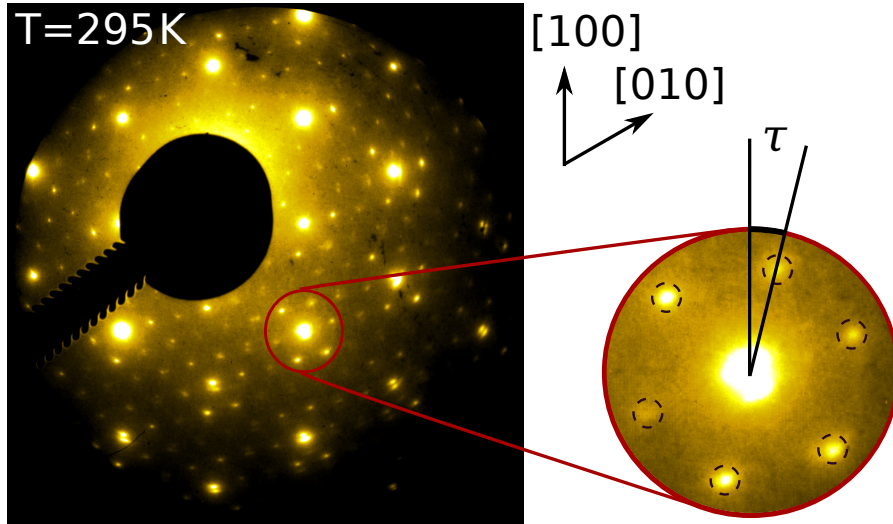


Figure 5.8: Electron diffraction data from a sample of 1T-TaS<sub>2</sub> in the NC phase of the same batch as the one used in RA-SHG measurements. Surrounding each Bragg reflection can be seen six CDW peaks, which are rotated about  $\tau = 13^\circ$  from the high-symmetry axes. The sign of the rotation angle  $\tau$  indicates whether the CDW configuration is  $\alpha$  or  $\beta$ . The lack of additional CDW peaks  $-13^\circ$  from the high-symmetry axes indicates that the sample is single-domain.

implies  $B \neq 0$ . This implies that  $\chi_{xyxx}^Q \neq 0$ , and therefore mirror symmetry is broken in the bulk.

There are two additional important remarks which can be made about Eq. 5.29. For one, it should be noted that the  $\theta$  dependence observed in Figs. 5.4(a) and 5.4(b) is consistent with Eq. 5.29, since  $B_0 = 0$  for  $\theta = 0$ . Additionally, we see that in the absence of the quadrupole component (i.e. for purely electric dipole SHG),  $B_0 = 0$  and the pattern should have sixfold rotational symmetry. Since the data in Figs. 5.4(a) and 5.4(c) clearly break this symmetry, this supports our claim that there is an extra contribution to the RA-SHG beyond the surface electric dipole contribution.

A more intuitive way to understand why the threefold spectral compo-

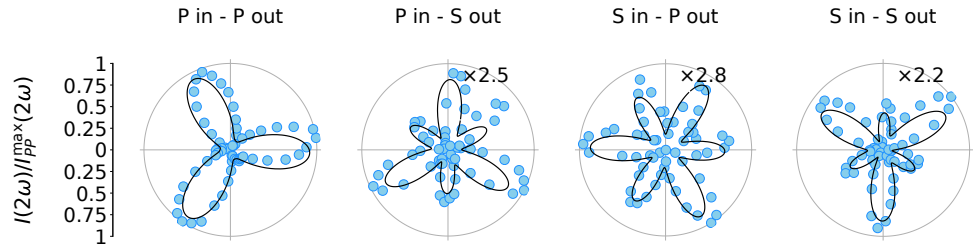


Figure 5.9: RA-SHG intensity as a function of  $\phi$  at  $T = 295K$ . Solid lines are best fits to the data using a surface electric dipole term in the point group  $C_3$ , as well as a bulk electric quadrupole term in the point group  $S_6$ . Data is normalized to the maximum value of the  $P_{\text{in}}-P_{\text{out}}$  signal.

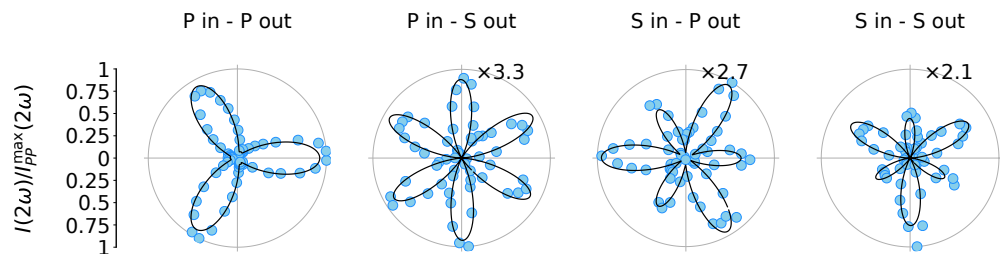


Figure 5.10: RA-SHG intensity as a function of  $\phi$  at  $T = 356K$ . Solid lines are best fits to the data using a surface electric dipole term in the point group  $C_{3v}$ , as well as a bulk electric quadrupole term in the point group  $S_6$ . Data is normalized to the maximum value of the  $P_{\text{in}}-P_{\text{out}}$  signal.

ment in Fig. 5.4(a) and Fig. 5.4 is not allowed by pure electric dipole SHG is to note that, for purely electric dipole SHG, the rotational anisotropy always has at least twofold symmetry in the  $S_{\text{in}}-S_{\text{out}}$  channel. To see that this is true, consider the effect of taking  $\phi \rightarrow \phi + \pi$  in an  $S$ -polarized input geometry. In the frame where the sample is stationary, this simply changes the sign of the input field. Since the polarization is proportional to the square of the input field ( $P_i(2\omega) = \chi_{ijk}E_jE_k$ ), then it will be symmetric under  $\phi \rightarrow \phi + \pi$ , as will be its projection out of the plane of incidence (note, however, that because the component of  $\mathbf{P}(2\omega)$  parallel to the direction of propagation is not visible in the experiment, the same cannot be said for the  $P$ -polarized output). Therefore, if the measured RA-SHG in

the  $S_{\text{in}}\text{-}S_{\text{out}}$  channel lacks twofold symmetry, then there is a contribution to the rotational anisotropy which exists beyond the electric dipole.

For the sake of completeness, we also note here two alternative explanations for the breaking of sixfold rotational symmetry depicted in Fig. 5.4(c) which do not appeal to an additional quadrupole contribution. Firstly, it is possible that the surface of the sample was rough or nonuniform in such a way as to modulate the observed SHG intensity as a function of  $\phi$ . In principle, this could result in a nonzero  $B_0$ . To account for this artifact, we measured SHG on 1T-TaS<sub>2</sub> in multiple locations and on multiple different samples, and found that the results in this work were consistent across all measurements. Furthermore, with SHG measurements there is always the possibility of an additional contribution arising from the presence of adsorbates on the sample surface[? ]. While such a contribution may be present in our experiment, we note that this too is an unlikely explanation for the nonzero  $B_0$  because of the wavevector dependence of Figs. 5.4(a) and 5.4(b). This is because the dominant contribution from adsorbates is generally of the electric dipole type and therefore should not depend on  $k$  in  $S_{\text{in}}\text{-}S_{\text{out}}$ .

### 5.7.6 Methods

RA-SHG data was taken with the 800 nm pulsed output of a regeneratively amplified Ti:Sapphire laser operating at 5 kHz. The beam was scattered by a transmissive phase grating into multiple diffraction orders, and the +1-order component was steered through a polarizer and focused onto the sample with a fluence of 1.4 mJ/cm<sup>2</sup> and a spot diameter of  $\sim 150\mu\text{m}$  at a 10° angle with respect to the (001) sample normal. This experimental geometry is similar to that described in [? ] and [? ]. The reflected light at 400 nm was directed through an analyzer and into a photomultiplier tube, where the intensity was measured with a lock-in amplifier synchronized to the 5 kHz pulsed output of the laser with a 1 ms time constant. We rotated the phase grating at  $\sim 5$  Hz and recorded the signal as a function of time with an oscilloscope triggered on an optical rotary encoder marking 360° rotations. Each polarization combination required averaging 5000 rotations. Using the aforementioned encoder, we expressed the corresponding time trace in terms of the azimuthal angle  $\phi$  (Fig. 5.1(b)) to obtain the full rotational anisotropy.

The thickness of the samples used in the RA-SHG experiments was  $\sim 50 \mu\text{m}$ .

## Chapter 6

---

### *Light-induced reorientation transition in the antiferromagnetic semiconductor $\text{CaMn}_2\text{Bi}_2$*

#### **6.1 Preface**

This chapter is based on a manuscript intended for standalone publication and modified to fit the format of this thesis. It was coauthored by myself and Baiqing Lv (as co-first authors), along with Karna Morey, Zongqi Shen, Changmin Lee, Elizabeth Donoway, Alex Liebman-Peláez, Anshul Kogar, Takashi Kurumaji, Martin Rodriguez-Vega, Rodrigo Humberto Aguilera del Toro, Mikel Arruabarrena, Batyr Ilyas, Tianchuang Luo, Peter Müller, Aritz Leonardo, Andres Ayuela, Gregory A. Fiete, Joseph G. Checkelsky, Joseph Orenstein, and Nuh Gedik. A detailed description of each author's contributions may be found in Section 6.9.

#### **6.2 Abstract**

Due to the lack of a net magnetic moment, antiferromagnets possess a unique robustness to external magnetic fields and are thus predicted to play an important role in future magnetic technologies. However, this robustness also makes them quite difficult to control, and the development of novel methods to manipulate these systems with external stimuli is a fundamental goal of antiferromagnetic spintronics. In this work, we report evidence for a metastable reorientation of the order parameter in an antiferromagnetic semiconductor triggered by an ultrafast quench of the equilibrium order via photoexcitation above the band gap. The metastable state forms less than 10 ps after the excitation pulse, and persists for longer than 150 ps before decaying to the ground state via thermal fluctuations. Importantly, this transition cannot be induced thermodynamically, and requires the system to be driven out of equilibrium. Broadly speaking,

this phenomenology is ultimately the result of large magnetoelastic coupling in combination with a relatively low symmetry of the magnetic ground state. Since neither of these properties are particularly uncommon in magnetic materials, the observations presented here imply a generic path toward novel device technology enabled by ultrafast dynamics in antiferromagnets.

### 6.3 Introduction

When the Hamiltonian of a system contains multiple interaction strengths of comparable magnitude, the corresponding free energy is often host to a diverse collection of metastable states just barely separated in energy from the true ground state. This phenomenology results in an extreme sensitivity to external stimuli[? ? ? ], which can be exploited in an ultrafast way using light to drive transitions between these states[? ? ? ? ].

One important application is in magnetic devices, where the electron spins form an ordered state in equilibrium and may thus be used to store information. AFMs have received special attention in this regard, as they possess zero net magnetic moment and are thus robust to stray magnetic fields from adjacent magnetic devices[? ]. The dominance of exchange rather than anisotropy energies in the dynamics of spins which are antiferromagnetically ordered also leads to order-of-magnitude faster switching timescales compared to their ferromagnetic counterparts[? ].

Importantly, the ground state of an AFM is typically not unique, with the number of degenerate states (corresponding generically to various rotations of the AFM order parameter (OP)) being determined by the number of symmetries which are broken at the magnetic ordering temperature. In the context described above, this degeneracy invites the possibility of an ultrafast antiferromagnetic device which uses light to switch between these different states. Moreover, if the symmetry of the magnetic phase is sufficiently low (relative to the parent phase), the number of such states can be quite high, and a multi-step magnetic memory might be constructed which operates via ultrafast reorientation transitions of the AFM OP between states that are not anti-parallel.

Broadly speaking, one can distinguish two different approaches for achieving such transitions in real materials. In the first case, one imagines manipulating the AFM orientation “coherently” by, for example,

resonantly driving an infrared-active phonon mode to large amplitude, although this usually requires large electric fields (as the relevant light-matter interactions are usually highly nonlinear[? ]) which are difficult to obtain in the frequency range associated with phonons in crystals. An alternative mechanism—which has been shown to occur abundantly in superconductivity (SC)[? ] and CDW[? ] systems—is to *quench* the equilibrium order by exciting carriers above the band gap, and then exploit the subsequent relaxation dynamics which may, in the right system, show a preference for one state over the other[? ]. In contrast to the case of resonant phonon driving, this mechanism involves primarily electronic excitations and therefore requires relatively little energy if the photon frequency is above the band gap. However, despite successful demonstrations of this approach in nonmagnetic systems[? ? ], evidence for this mechanism occurring in AFMs does not currently exist, and whether the phenomenology described here actually occurs in real magnetic materials remains a fundamental open question.

In this work, we report a light-induced phase transition between nearly degenerate AFM states in the antiferromagnetic semiconductor  $\text{CaMn}_2\text{Bi}_2$  [? ] triggered by an ultrafast quench of the equilibrium OP with a femtosecond light pulse. Using tr-SHG, a pump-probe technique with the unique ability to track both the magnitude and direction of the AFM order parameter as a function of time, we find that above-gap optical excitation indeed causes the system to switch to a new, metastable orientation of the AFM OP. The transition is fast (occurring less than 10 ps after photoexcitation), requires low pump fluence ( $\sim 200 \mu\text{J} \cdot \text{cm}^{-2}$  vs.  $\sim 10 \text{ mJ} \cdot \text{cm}^{-2}$  [? ]), and cannot be induced thermodynamically. These findings suggest a new way to manipulate AFMs, and open the door to novel opto-spintronic device architectures exploiting nonequilibrium phase transitions between different nearly degenerate states.

## 6.4 Results

### 6.4.1 Equilibrium

Crystallographically,  $\text{CaMn}_2\text{Bi}_2$  consists of a puckered-honeycomb tiling of Mn atoms with a high-temperature crystallographic point group of  $\bar{3}m$  (see Fig. 6.1(a)). The electronic gap is on the order of 4 meV (see Fig. 6.1(b))

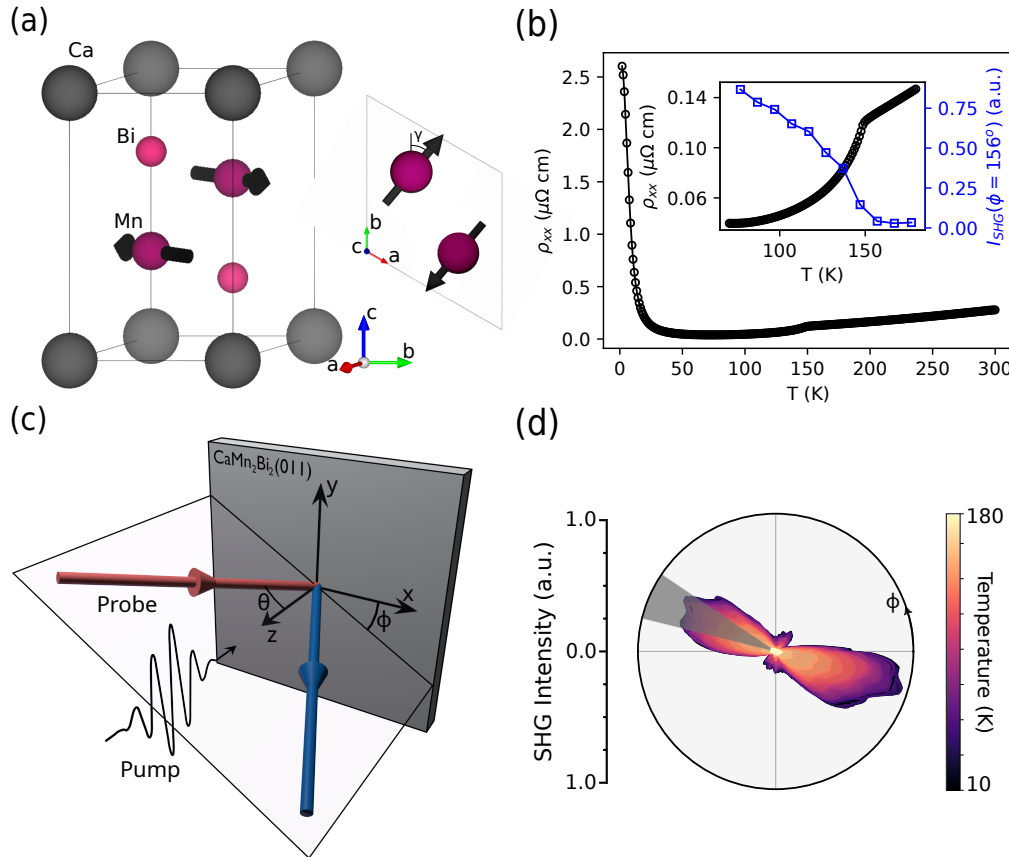


Figure 6.1: (a) Magnetic unit cell of  $\text{CaMn}_2\text{Bi}_2$ . The angle  $\gamma$  is such that the Mn spin does not lie precisely along any particular crystallographic axis. (b) Resistivity as a function of temperature for a representative sample. Inset shows an enlarged view of the resistivity near  $T_c$  plotted against the SHG intensity integrated across the region indicated in 6.1(d). (c) Schematic of the RA-SHG setup. (d) Temperature dependence of the RA-SHG intensity in the  $P_{\text{in}}P_{\text{out}}$  polarization channel from the (011) surface of  $\text{CaMn}_2\text{Bi}_2$ . Other polarization channels are shown in the Supplementary material, Fig. 6.14. The shaded area indicates the region integrated to produce the inset of 6.1(b).

and is thought to be due to a delicate combination of correlations and hybridization between relatively localized Mn 3d states and dispersive Bi 6p / Mn 4s hybrid bands[? ? ? ]. Néel-type antiferromagnetic LRO with spins lying in the *ab*-plane develops in this material at  $T_c = \sim 150$  K, accompanied by a kink in the electrical resistivity (Fig. 6.1(b)) and the appearance of a new peak in the powder neutron diffraction[? ]. Importantly, the powder neutron refinement indicates that the ordered moments are slightly misaligned with the *a*- and *b*-axes of the high-symmetry phase (see Fig. 6.1(a)), so that the low-temperature magnetic point group is  $\bar{1}'$ ; i.e., the only symmetries that are preserved in the low temperature phase are the identity operator and the product of inversion and time-reversal[? ]. The remarkably low symmetry of this magnetic ground state is likely due to highly frustrated magnetic interactions, as suggested by to the proximity of isostructural CaMn<sub>2</sub>Sb<sub>2</sub> to a mean-field magnetic tricritical point[? ? ]. In contrast, the lattice is thought to remain fully symmetric at all temperatures, so that the symmetry-breaking at  $T_c$  is solely due to the AFM order (this is verified with single-crystal X-ray diffraction (XRD), see Supplementary material, Fig. 6.13).

As spin-orbit coupling is expected to be strong in this material, the breaking of inversion symmetry by the magnetic order should result in a strong SHG signal below  $T_c$ , despite the fact that the lattice remains centrosymmetric[? ? ]. We probe this SHG signal using a RA-SHG apparatus (Fig. 6.1(c)) which measures the reflected second harmonic intensity as the plane of incidence is rotated about the sample normal[? ? ]. Figs. 6.1(b) and 6.1(d) depict the SHG signal from the (011) surface of CaMn<sub>2</sub>Bi<sub>2</sub> as a function of temperature across  $T_c$ , demonstrating that RA-SHG is indeed sensitive to the magnetic order in this material.

Frequently, AFM materials may host intricate domain configurations, the details of which greatly impact the relevant magnetic functionalities[? ? ]. Because the low-temperature magnetic point group of CaMn<sub>2</sub>Bi<sub>2</sub> breaks multiple symmetries of the high-temperature point group, we indeed expect that the low-temperature magnetic ground state should involve some number of energetically degenerate domains. In Fig. 6.2, we characterize these domains using a combination of RA-SHG and a spatially-resolved optical polarimetry technique known as photo-thermal modulated birefringence (PTMB), which is a sensitive technique for measuring small changes in the anisotropic index of refraction (and consequently, the direction of the AFM OP)[? ? ].

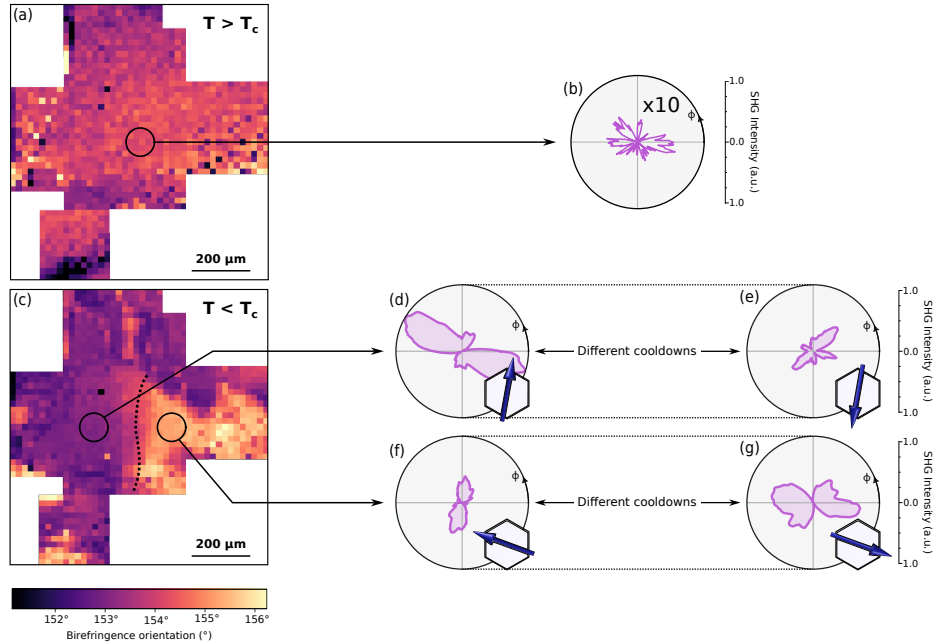


Figure 6.2: (a) Birefringence orientation map for  $T = 200\text{ K} > T_c$ . (b) RA-SHG intensity in the  $P_{\text{in}}P_{\text{out}}$  polarization channel for the region indicated in 6.2(a) at 157 K. Other polarization channels are shown in the Supplementary material, Fig. 6.15. (c) Birefringence orientation map for  $T = 152.5\text{ K} < T_c$ . (d) (e) RA-SHG intensity at 8 K in the  $P_{\text{in}}P_{\text{out}}$  polarization channel for consecutive cooldowns for the region indicated in 6.2(c). The system randomly chooses the RA-SHG pattern in 6.2(d) or 6.2(e) on each cooldown. Insets show the corresponding value of the AFM OP proposed in the text, relative to the hexagonal crystallographic motif. Other polarization channels are shown in the Supplementary material, Fig. 6.15. (f) (g) RA-SHG intensity at 8 K in the  $P_{\text{in}}P_{\text{out}}$  polarization channel for consecutive cooldowns for the region indicated in 6.2(c). The system randomly chooses the RA-SHG pattern in 6.2(f) or 6.2(g) on each cooldown. Insets show the corresponding value of the AFM OP proposed in the text, relative to the hexagonal crystallographic motif. Other polarization channels are shown in the Supplementary material, Fig. 6.15. The schematic representations beneath the RA-SHG plots are for illustration purposes only and the depicted angles are not quantitatively verified.

Fig. 6.2(a) shows the PTMB signal from the (011) surface of  $\text{CaMn}_2\text{Bi}_2$  above  $T_c$ . No contrast is found within a  $\sim 500 \mu\text{m} \times 500 \mu\text{m}$  area on the sample, suggesting that the thermally modulated index of refraction is spatially uniform at high temperature. As the temperature is lowered below  $T_c$  (Fig. 6.2(c)), a pronounced contrast appears in the PTMB map which indicates the presence of two separate AFM domains with different OP directions.

While PTMB is nominally sensitive to the direction of the AFM OP, it cannot differentiate between  $180^\circ$  domains as it couples only to the linear index of refraction of the material. Therefore, it is not clear from PTMB alone whether the domains in Fig. 6.2(c) are truly homogeneous or may contain a mixture of  $180^\circ$  domains. In contrast, nonlinear spectroscopies like SHG can differentiate  $180^\circ$  AFM domains due to an interference between the SHG sources (e.g. electric dipole, magnetic dipole, and electric quadrupole) which transform differently under time-reversal symmetry[? ? ? ? ]. This effect can be especially pronounced in the presence of magnetostriction[? ]. We thus proceed to investigate the presence of  $180^\circ$  domains in this material using RA-SHG.

Figs. 6.2(d)–g) depict the RA-SHG results at 8 K in the two regions identified in Fig. 6.2(c). The same crystal piece was used for both measurements. As with PTMB, we do find that the SHG domains are large and apparently homogenous (on a scale of hundreds of  $\mu\text{m}$ ). Surprisingly, however, in different cooldowns we observe that the RA-SHG pattern in the leftmost region of Fig. 6.2(c) randomly takes the form of either Fig. 6.2(d) or Fig. 6.2(e), and in the rightmost region, it takes the form of either Fig. 6.2(f) or Fig. 6.2(g). In contrast, the PTMB does not change upon thermal cycling. Anticipating again that RA-SHG should be sensitive to the phase of the AFM OP as well as its direction, we interpret Fig. 6.2 as follows: Fig. 6.2(d) and Fig. 6.2(e) correspond to opposite  $180^\circ$  AFM domains, as do Fig. 6.2(f) and Fig. 6.2(g); in addition, there is a relative angle between Figs. 6.2(d)–e) and Figs. 6.2(f)–g), as indicated by the PTMB. This interpretation is depicted schematically in the insets to Figs. 6.2(d)–g), where the AFM OP (defined as the difference in the magnetic moment on the two Mn sublattices, see Fig. 6.1(a)) is represented by a blue arrow. Importantly, within a single location, the two opposite orientations are accessible via thermal cycling; hence they are energetically degenerate. We have verified that the identification described here is consistent with the SHG susceptibility tensors[? ] extracted by fitting the data in Fig. 6.2 (see

Supplementary material, Section 6.10.3). In addition, the data presented in Fig. 6.2 is not consistent with an alternative interpretation involving the interference of two independent order parameters (see Supplementary material, Section 6.10.2).

#### 6.4.2 Nonequilibrium

Having demonstrated that  $\text{CaMn}_2\text{Bi}_2$  hosts an elaborate free energy surface with multiple degenerate or nearly degenerate ground states, we now turn to the question of whether light can be used to manipulate or possibly switch between these states. To answer this question, we pump each of the OP directions identified in Fig. 6.2 at 8 K with a  $\sim 100$  fs normally incident near-infrared light pulse ( $\hbar\omega \approx 1$  eV) and probe the AFM OP with RA-SHG using a subsequent probe pulse. By varying the delay  $\Delta t$  between the two pulses, we create a series of snapshots of the AFM OP at different times following excitation. The results are shown in Fig. 6.3, where the four rows correspond to the four OP directions identified in Fig. 6.2, and the horizontal axis is the time delay between the pump and probe pulses. The first two rows (Figs. 6.3(a)–b)) correspond to the left-most domain in Fig. 6.2(c), for which it is found that, after pumping, the strength of the RA-SHG signal is quickly extinguished. After a delay of around  $\sim 8 - 10$  ps, the AFM order recovers so that the shape of the RA-SHG pattern is similar to before zero delay up to small changes in the relative peak heights. The OP magnitude and direction inferred by this data is depicted schematically in the insets to Figs. 6.3(a)–b).

The striking observation is in the latter two rows (Figs. 6.3(c)–d)), which depict the time-resolved RA-SHG results in the rightmost domain of Fig. 6.2(c). In this domain, the RA-SHG signal again quickly decreases, and the shape does not initially change. However, roughly  $\sim 6 - 8$  ps after excitation, the RA-SHG pattern abruptly changes shape, so that the pattern after  $\sim 10$  ps is equivalent to Fig. 6.3(a). Together with the findings of Fig. 6.2, these results suggest that the final state in Figs. 6.3(c)–d) is one in which the AFM OP direction has indeed been reoriented relative to equilibrium. Remarkably, one must use light to reach this metastable state as it is not present in thermal equilibrium at this spot.

We performed the above measurements out to  $\Delta t \gtrsim 150$  ps (see Supplementary material, Fig. 6.19) and found that the reoriented state persists at least this long before relaxing back to equilibrium in time for the next

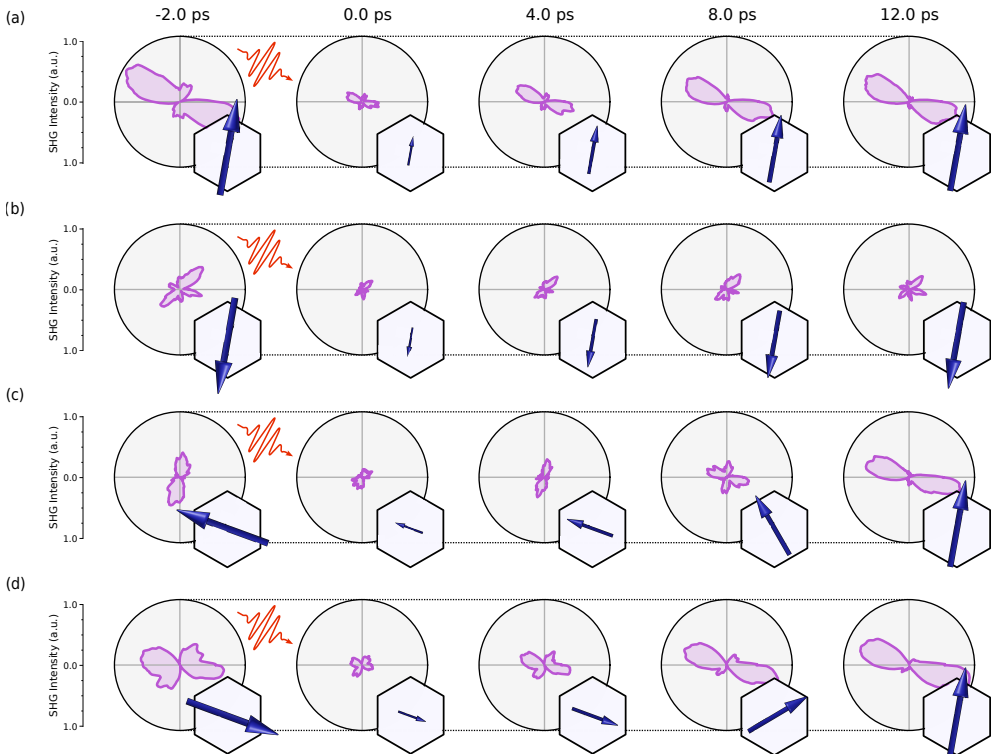


Figure 6.3: RA-SHG intensity at 8 K in the  $P_{\text{in}}P_{\text{out}}$  polarization channel as a function of time for the AFM OP identified in (a) Fig. 6.2(d), (b) Fig. 6.2(e), (c) Fig. 6.2(f), and (d) Fig. 6.2(g). The pump fluence is set to  $\sim 600 \mu\text{J} \cdot \text{cm}^{-2}$ . Insets show the corresponding value of the AFM OP proposed in the text, relative to the hexagonal crystallographic motif. Other polarization channels are shown in the Supplementary material, Fig. 6.16. The schematic representations beneath the RA-SHG plots are for illustration purposes only and the depicted angles are not quantitatively verified.

pair of pulses to arrive (roughly 200  $\mu\text{s}$  later). As the pump fluence is decreased (see Supplementary material, Fig. 6.11), the effect of the excitation is diminished until, at low fluences ( $\sim 100 \mu\text{J} \cdot \text{cm}^{-2}$ ), the final state is equivalent to the initial state, and only small changes to the SHG (associated with dynamics that do not launch the system into the metastable state) are visible near zero delay. Interestingly, which of the two opposite directions (Fig. 6.2(d) or Fig. 6.2(e)) the magnetic order favors after excitation is consistent from pulse to pulse, but not from one sample to another (see Supplementary material, Figs. 6.18 and 6.19), suggesting that, below the magnetic ordering temperature, interactions between neighboring domains break the degeneracy between these states. Finally, we note that no aspect of these observations changes with the polarization of the pump pulse (see Supplementary material, Fig. 6.17).

## 6.5 Discussion

Taken together, these considerations indeed point to a *bona fide* ultrafast phase transition in CaMn<sub>2</sub>Bi<sub>2</sub> induced by a femtosecond light pulse. We now seek to understand, at least qualitatively, the microscopic nature of this transition. Before discussing the time-resolved data of Fig. 6.3, we must first understand the equilibrium phenomenology implied by Fig. 6.2. Group theory (see Supplementary material, Section 6.10.1.3) suggests that there should be twelve energetically degenerate OP directions, independent of location on the sample. However, only two directions are observed per measurement location in our experiment. This observation is explained by recognizing that local strain fields in the material are expected to pole the LRO (see Supplementary material, Section 6.10.1.1), so that certain OP directions are energetically favored relative to others at a given spot[? ? ]. Since these strain fields may vary from one location to another (the details of which depend subtly on the local growth conditions), different locations on the sample would then show different sets of RA-SHG patterns, in agreement with the findings of Fig. 6.2. This picture also explains the observation that opposite AFM configurations are energetically degenerate, as strain itself is inherently symmetric under 180° rotations.

Turning now to the nonequilibrium phenomenology (Figs. 6.3 and 6.4), we begin by noting that the sudden suppression of the SHG intensity at

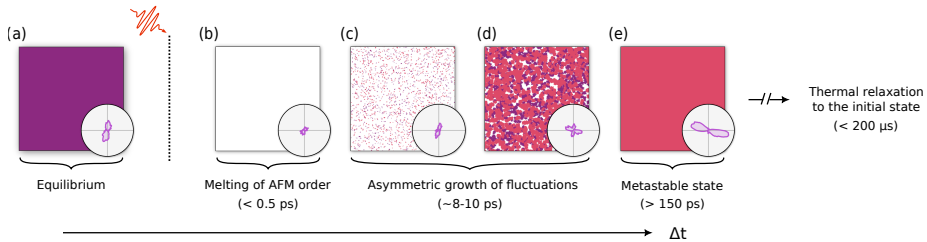


Figure 6.4: Illustration of the dynamics following laser excitation as described in the text. Ultrafast melting of the AFM order (6.4(a)-6.4(b)) is followed by the rapid growth of fluctuations (6.4(c)-6.4(d)), with the final state (6.4(e)) determined by the relative growth rate of different orders. The fluctuation growth step (6.4(c)-6.4(d)) may occur with or without a background of coherent oscillations (see Supplementary material, Sections 6.10.1.2 and 6.10.1.3).

early times indicates that the primary effect of the pump pulse is simply to quench the AFM OP (Figs. 6.4(a) and 6.4(b)). According to recent theoretical work [??], the dynamics following such a quench are governed not by the global minimum of the free energy, but rather by the exponential amplification of spatial OP fluctuations (Figs. 6.4(c) and 6.4(d)), which may occur differently for different orders (Supplementary material, Section 6.10.1.2). The final state of the transition (Fig. 6.4(e)) is then determined by which state supports the fastest-growing fluctuations. In the context of light-induced SC[??], for example, the dominant order in equilibrium is a CDW, whose fluctuations naturally involve motion of the massive nuclei and are thus much slower than fluctuations of the SC OP[??]. Note that, in the general case, the final state is determined not just by the relaxation rates, but also by their start times; that is, if one order is *quenched* faster than another, fluctuations of that order are afforded a longer period to grow and may thus dominate at long times.

In our system, the relatively slow ( $\sim 8 - 10$  ps, see Fig. 6.3) recovery timescale indicates that the dynamics of the AFM OP, like the CDW order of ??, also likely involve motion of the atomic nuclei (i.e. magnetoelastic coupling). However, in contrast to the CDW-SC competition referred to above, the dominant and subdominant orders in our system correspond

not to completely different orders, but rather to different orientations of the same order. One would thus naively expect the corresponding fluctuations to exhibit more or less the same dynamics. However, as described above, this naive symmetry of the material is in fact broken at all temperatures by the internal strain; thus, it is appropriate to think of the two non-parallel AFM orientations as truly distinct orders. Importantly, it is noted in [? ] that small variations in the density of different fluctuations are exponentially amplified as the system relaxes, so that only a modest difference in the relevant dynamics is sufficient to favor the metastable state as the system recovers. Such asymmetric amplification of non-parallel AFM orientations thus likely forms the basis for the reorientation transition in CaMn<sub>2</sub>Bi<sub>2</sub>.

Evidence supporting this picture may be found by examining the time dependence of the SHG signal at short times (Supplementary material, Fig. 6.10), before the OP switches to the metastable state. In particular, on examining the initial decay rates it can be seen that the SHG signal corresponding to Fig. 6.3(a) reaches 30% of its original value just 0.5 ps after zero delay; the equivalent drop in SHG intensity for Fig. 6.3(c) takes > 0.5 ps longer. That is, the quench dynamics associated with the metastable state are roughly twice as fast as those associated with the equilibrium state. As a result, long-wavelength fluctuations of the sub-dominant, metastable order experience a longer period of exponential amplification compared to the equilibrium order, which may explain the dominance of the metastable state at long times. The metastability of the final state is provided by the fact that the long-term relaxation dynamics are presumably dependent on the thermal nucleation and subsequent motion of AFM domain walls, which can be quite slow[? ? ]. Finally, we remark that while the quench dynamics described here can explain all features of our data, they also likely occur alongside a background of coherent excitations (e.g. coherent phonons, which are observable in time-resolved reflectivity, see Supplementary material, Fig. 6.12) which can couple to the order parameter via the lattice strain (see Supplementary material, Section 6.10.1.3). While no evidence of these excitations is apparent in our SHG data, further studies will be needed to determine the extent to which they might still be important.

## 6.6 Conclusion

To summarize, we have presented evidence of a magnetic reorientation transition in the antiferromagnetic semiconductor  $\text{CaMn}_2\text{Bi}_2$  induced by above-gap optical excitation. Looking forward, we note two ingredients that seem to be most important for the transition demonstrated in this work: low symmetry, so that there are multiple energetic minima in the magnetic phase, and, presumably, some degree of magnetoelastic coupling, so that the different minima are not precisely degenerate in thermal equilibrium. Neither of these properties are unique to  $\text{CaMn}_2\text{Bi}_2$ , and analogous materials may exist with similar light-induced phenomenology. The apparently pronounced coupling between light and magnetic order in this material also invites the fascinating possibility that the magnetic order could be manipulated via additional tuning parameters like strain or current. This is a key prediction of so-called  $\mathcal{PT}$ -symmetric systems, in which inversion and time-reversal symmetries are independently broken but the product of the two is preserved[? ? ? ]. Further investigation of these and related compounds could have far-reaching impacts for future opto-spintronic technology.

## 6.7 Methods

### 6.7.1 Material growth

Single crystals of  $\text{CaMn}_2\text{Bi}_2$  were grown by a Bi flux method following [? ]. The starting materials were Ca ingot, Mn powder, and Bi powder. They were loaded into an alumina crucible in the molar ratio of Ca : Mn : Bi = 1 : 2 : 10, which was sealed in an evacuated quartz tube. The ampoule was heated to 1000°C and kept at this temperature for 11 hours before being slowly cooled to 400°C in 10 days. The excess flux was removed by a centrifuge at this temperature. The single phase nature of the crystals was checked by powder XRD and the orientation was checked by a single-crystal x-ray diffractometer.

### 6.7.2 Tr-SHG measurements

The tr-SHG measurements were performed using a fast-rotating optical grating method which has been described previously[? ? ? ]. Ultra-

short ( $\sim 100$  fs) probe pulses were sourced from a regeneratively amplified Ti:Sapphire laser operating at a repetition rate of 5 kHz. A portion of the Ti:Sapphire output was directed to an optical parametric amplifier, producing  $\sim 1$  eV pump pulses which were delayed relative to the probe pulses with an optical delay line. The incident probe fluence was  $\sim 250 \mu\text{J} \cdot \text{cm}^{-2}$ , with the probe spot diameter being  $\sim 100 \mu\text{m}$  at the sample surface, and the pump pulses (with varying fluence) were focused to a spot roughly  $\sim 400 \mu\text{m}$  in diameter. The pump was normally incident to the sample surface, but the probe was incident with an angle of  $\sim 10^\circ$ . The reflected SHG signal was collected with a photomultiplier tube, filtered with a lock-in amplifier operating at the repetition rate of the regenerative amplifier, and correlated with the rotation angle of the grating with an optical rotary encoder and homebuilt oscilloscope. To eliminate potential artifacts due to low-frequency fluctuations in the laser intensity, multiple random sweeps of the delay stage were averaged together for each dataset, and the polarizers were controlled automatically at each delay using custom polarization rotators described in [?].

### 6.7.3 PTMB measurements

The polarization-dependent optical birefringence (linear dichroism) measurements were conducted using the experimental setup detailed in [?]. A 633 nm probe laser beam was focused onto a  $5 \mu\text{m}$  spot at surface of the sample, while a 780 nm pump/heating beam was similarly focused onto the same location. To improve the signal-to-noise ratio and eliminate polarization artifacts originating from the experimental setup, the sample temperature was modulated at 2 kHz by passing the pump beam through an optical chopper. The linear dichroism signal was subsequently measured using a standard balanced photodetection scheme and a lock-in amplifier. Position-dependent measurements of optical birefringence were obtained by scanning the sample position with a piezoelectric scanner. The dependence of the polarization rotation on the probe polarization angle was fit to a sinusoidal function at each spot, and the phase shift parameter extracted from each fit was plotted in Figs. 6.2(a) and 6.2(c). Note that the birefringence signal involves contributions from both the lattice and the magnetism, so that the angle extracted from this fit should not be identified with the angle of the AFM OP.

### 6.7.4 XRD measurements

XRD data (Supplementary material, Fig. 6.13) were collected at 100 K and 180 K on a Bruker-AXS X8 Kappa Duo diffractometer with I<sub>μ</sub>S micro-sources, coupled to a Photon 3 CPAD detector using Mo K $\alpha$  radiation ( $\lambda = 0.710\,73\text{ \AA}$ ), performing  $\phi$ -and  $\omega$ -scans. Reconstructed precession images of the  $(0kl)$ ,  $(h0l)$  and  $(hk0)$  planes were calculated directly from the diffraction images using algorithms included in the APEX3[?] software.

### 6.7.5 Data availability

Data supporting the figures within this paper and other findings of this study are available from the corresponding author upon request.

## 6.8 Acknowledgments

The authors thank Clifford Allington, Martin Eckstein, Shiang Fang, Feng Hao, David Hsieh, Honglie Ning, Jia Xu, and Guangua Zhang for several helpful discussions. The authors also acknowledge the MIT SuperCloud and Lincoln Laboratory Supercomputing Center for providing HPC resources that have contributed to the research results reported within this paper. B.F., B.L., K.M., Z.S., B.I., T.L., and N.G. acknowledge support from the US Department of Energy, BES DMSE (data taking and analysis), and Gordon and Betty Moore Foundation's EPiQS Initiative grant GBMF9459 (instrumentation). C.L., E.D., A.L.-P., and J.O. acknowledge support from the Quantum Materials program under the Director, Office of Science, Office of Basic Energy Sciences, Materials Sciences and Engineering Division, of the US Department of Energy, Contract No. DE-AC02-05CH11231. G.A.F. gratefully acknowledges support from the NSF through the Center for Dynamics and Control of Materials: an NSF MRSEC under DMR-1720595, NSF DMR2114825, and the Alexander von Humboldt Foundation. R.H.A.d.T., M.A., A.L., and A.A. acknowledge support from the Spanish Ministry of Science and Innovation through grants PID2019-105488GB-I00, TED2021-132074B-C32 and PID2022-PID2022-139230NB-I00, the European Commission from the MIRACLE (ID 964450), and the Basque Government through Project No. IT-1569-22.

## 6.9 Author contributions

B.F. and B.L. led the project, under the supervision of N.G. B.F., B.L., K.M., and A.K. designed the SHG experiments. B.F., B.L., K.M., Z.S., and A.K. performed the SHG measurements. B.F., B.L., K.M., and Z.S. analyzed the SHG data. B.F., B.L., and A.K. conceived of the project. C.L, E.D., A.L.-P., and J.O. performed and analyzed the PTMB measurements. T.K. and J.C. grew the samples and performed the resistivity measurements. B.I. and T.L. performed the time-resolved reflectivity measurements. P.M. performed and analyzed the XRD measurements. M.R.V., G.A.F., R.H.A.d.T., M.A., A.L., and A.A. developed the theoretical models and performed the calculations. B.F. wrote the paper and supplemental material, except for the supplemental theoretical discussion, which was written by M.R.V. with input from R.H.A.d.T. All authors assisted in revising the manuscript.

## 6.10 Supplementary Material

### 6.10.1 Supporting theoretical discussion

#### 6.10.1.1 Equilibrium strain-spin coupling

To study the coupling between intrinsic strain and magnetic order in CaMn<sub>2</sub>Bi<sub>2</sub>, theoretical calculations were performed using the projected augmented wave method (PAW) implemented in the Vienna Ab-initio Software Package (VASP)[? ? ]. For the exchange and correlation potential, we use the Perdew-Burke-Ernzerhof form of the generalized gradient approximation (GGA), which is further corrected with the Couloumb U parameter following the GGA+U formulation of Dudarev[? ]. We perform a test calculation of the partial density of states (PDOS) using the HSE06 hybrid functional. Comparing this with the GGA and GGA+U calculations, we determine that for an improved system description, it is necessary to include the terms  $U(\text{Mn}) = 4\text{ eV}$  and  $U(\text{Bi}) = 3\text{ eV}$ . All calculations were performed with a well-converged plane-wave cutoff energy of 700 eV, a gamma-centered  $15 \times 15 \times 8$  Monkhorst-Pack  $k$ -point mesh, and a Fermi smearing of 20 meV. Atomic coordinates were relaxed until forces in all directions were smaller than 0.5 meV/Å. An energy convergence criterion of  $1 \times 10^{-7}$  eV is used. The atomic valence configuration

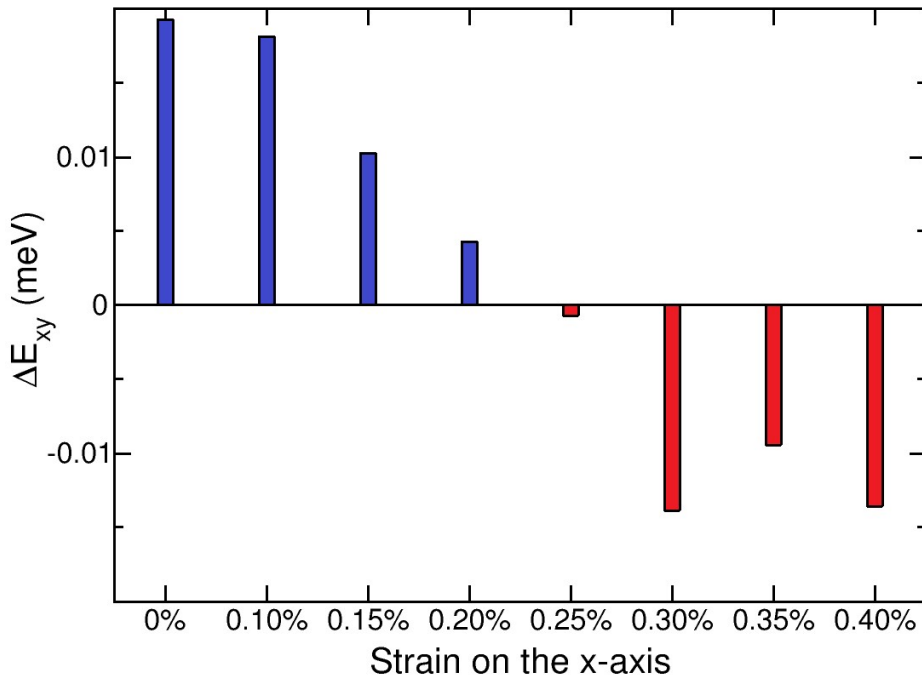


Figure 6.5: Energy difference between  $x$  and  $y$ -directions with respect to the easy axis. Blue bars indicate the  $x$ -direction for the AFM OP is preferred, and red bars indicate the  $y$ -direction for the AFM OP is preferred. Note that for strains in experiments, the difference value goes to zero, indicating a change in the in-plane magnetic moment direction.

for Ca, Mn and Bi are  $3s^23p^64s^24p^{0.01}$ ,  $4s^23d^5$  and  $6s^26p^3$ , respectively. The ground state in the trigonal unit cell shows AFM order between the Mn atoms with an energy difference of about 200 meV.

By including the spin-orbit coupling, we performed additional tests to converge the magnetocrystalline anisotropy energy (MAE) with respect to the Brillouin zone sampling. The spin-orbit coupling energetically favors certain spin orientations in the crystal. We have determined that the easy axis is the  $x$ -axis. The energy needed to align the spin out-of-plane is 2.4 meV, a value that is about a hundred times larger than the MAE difference with the  $y$ -axis, which is on the order of 0.02 meV. The MAE difference with respect to the  $z$ -axis remains constant regardless of strain.

The MAE difference between the  $x$  and  $y$  directions decreases by applying strain along the  $x$ -axis, as shown in Fig. 6.5. With a strain of around 0.25%, the easy spin orientation of the crystal changes to lie along the  $y$ -axis.

### 6.10.1.2 Laser-induced dynamics of competing magnetic domains: “incoherent” scenario

In this section, we explore the possibility of interpreting the results of the main text based on the recent quench dynamics theory introduced by Sun and Millis [?], and Dolgirev et al. [?].

We consider the four observed domains A, B, C, and D as competing AFM orders favored in equilibrium by the local sample anisotropy, regardless of its microscopic origin. Normally, in the absence of anisotropies, the magnetism in CaMn<sub>2</sub>Bi<sub>2</sub> would be described by model-G [?]. However, the presence of anisotropies, indicated by the existence of only four domains out of the expected twelve configurations due to symmetry, suggests that total magnetization is not conserved. Thus, the relaxational behavior of type A studied in detail in [? ?], is applicable. The corresponding relaxational time-dependent-Ginzburg-Landau model is given by  $\frac{1}{\gamma_i} \partial_t \psi_i(\mathbf{r}, t) = -\frac{\delta F(t)}{\delta \psi_i(\mathbf{r}, t)} + \eta_i(\mathbf{r}, t)$ , where  $\psi_i$  corresponds to the staggered magnetization in domain  $i = A, B, C$ , and  $D$ .  $\gamma_i$  and  $\eta_i$  are the  $i$ -th domain relaxation rate and Gaussian white noise source. The free-energy functional follows the form of Equation (2) in [?], with interactions among the domains,  $F = \int d^D \mathbf{r} (\sum_i f_i + f_c)$ ,  $f_i = -\alpha_i \psi_i^2 + (\xi_{i0} \nabla \psi_i)^2 + \psi_i^4$ , and  $f_c = \psi_C^2 (c_{AC} \psi_A^2 + c_{CB} \psi_B^2) + \psi_D^2 (c_{AD} \psi_A^2 + c_{BD} \psi_B^2)$ .  $\xi_{i0}$  is the bare coherence lengths, and  $\alpha_i = \alpha_i(t)$  is a time-dependent dimensionless coefficient influenced by the laser pump excitation’s temperature profile.

During the laser pump excitation, characterized by a high temperature and  $\alpha_i(t) < 0$ , and until  $\alpha_i(t) = 0$ , the mean-field order parameters have small values, and the dynamics are governed by order-parameter fluctuations. Subsequently, the fluctuations grow exponentially, leading to a metastable state determined by the fastest-relaxing domain. In our experiment, domain A always goes to A, domain B always goes to B, while domain C and D can go to either A or B. Assuming that the coefficients  $\alpha_i$  in equilibrium are equal across the four domains, this observation aligns with the theory prediction if  $\gamma_{A/B} > \gamma_{C/D}$  and  $\gamma_A \approx \gamma_B$ .

### 6.10.1.3 Laser-induced dynamics of competing magnetic domains: “coherent” scenario

*Group theory aspects of the magnetic order*

$\text{CaMn}_2\text{Bi}_2$  belongs to the trigonal symmorphic space group  $P\bar{3}m1$  (No. 164) [? ]. The Wyckoff positions of the atoms are Bi 2d, Mn 2d, and Ca 1a. The Ca atoms form a triangular lattice on the top and bottom of the Bi and Mn atoms, while Mn and Bi form buckled hexagonal lattices. At the  $\Gamma$  point, the point group is  $\bar{3}m$ , which possess twelve symmetry operations:

$$\begin{aligned}\{1|0\}: (x, y, z) &\rightarrow (x, y, z) \\ \{3_{001}^+|0\}: (x, y, z) &\rightarrow (-y, x - y, z) \\ \{3_{001}^-|0\}: (x, y, z) &\rightarrow (-x + y, -x, z) \\ \{2_{110}|0\}: (x, y, z) &\rightarrow (y, x, -z) \\ \{2_{100}|0\}: (x, y, z) &\rightarrow (x - y, -y, -z) \\ \{2_{010}|0\}: (x, y, z) &\rightarrow (-x, -x + y, -z)\end{aligned}$$

plus their composition with inversion symmetry  $\{-1|0\} : (x, y, z) \rightarrow (-x, -y, -z)$ . With this lattice information above the magnetic transition temperature, we proceed with a group theory analysis of the possible magnetic orders with the aid of ISOTROPY [? ]. In  $\text{CaMn}_2\text{Bi}_2$ , the magnetic transition is not accompanied by a lattice deformation, such that the magnetic unit cell coincides with the chemical unit cell. Therefore, the magnetic order is associated with  $\Gamma$  point irreducible representations. The magnetic subgroups resulting from the onset of all possible  $\Gamma$  point irreducible representations are shown in table 6.1. The  $A_{2g}$  and  $A_{1u}$  irreducible representations (irreps) correspond to out-of-plane ferromagnetic and antiferromagnetic order, respectively. The two-dimensional irreps  $E_g$  and  $E_u$  induce in-plane magnetic and AFM order, respectively. A general direction of the OP is associated with the magnetic subgroup  $P\bar{1}'$ , which corresponds to the experimental magnetic space group [? ]. Notice that special directions of the OP lead to magnetic structures with higher symmetry and corresponding magnetic space groups  $C2/m'$  or  $C2'/m$ .

Finally, noting that each of the twelve symmetry operations listed above leads to a different AFM OP direction (as the real OP does not lie along any of the special directions), the free energy surface in equilibrium

should have exactly twelve minima in the absence of strain, as referenced in the text.

IR	Subgroup	Direction
$\Gamma_1^+ (A_{1g})$	(164.85) $P\bar{3}m1$	P1 (a)
$\Gamma_2^+ (A_{2g})$	(164.89) $P\bar{3}m'1$	P1 (a)
$\Gamma_3^+ (E_g)$	(12.58) $C2/m$	P1 (a,-1.732a)
	(12.62) $C2'/m'$	P2 (a,0.577a)
	(2.4) $P1$	C1 (a,b)
$\Gamma_1^- (A_{1u})$	(164.88) $P\bar{3}'m'1$	P1 (a)
$\Gamma_2^- (A_{2u})$	(164.87) $P\bar{3}'m1$	P1 (a)
$\Gamma_3^- (E_u)$	(12.60) $C2'/m$	P1 (a,-1.732a)
	(12.61) $C2/m'$	P2 (a,0.577a)
	(2.6) $P1'$	C1 (a,b)

Table 6.1: Subgroups obtained by the onset of magnetic order of a given irreducible representation. The columns indicate the irreducible representations, the magnetic group, and the OP direction in the representation space.

#### *Free energy model*

Now we construct a free energy model considering magnetic order, strain, and phonon modes. As discussed in the previous section, the in-plane AFM groundstate corresponds to the magnetic irrep  $\Gamma_3^-$ , with general in-plane OP directions  $L_1, L_2$ . The parent cell supports strain mode distortions with irrep  $\Gamma_1^+$  and  $\Gamma_3^+$ . We consider a two component  $\Gamma_3^+$  mode with components  $\epsilon_{xx} = -\epsilon_{yy}$  ( $\epsilon_1$ ) and  $\epsilon_{xy}$  ( $\epsilon_2$ ). Finally, the phonon mode ( $Q$ ) is assumed to be totally symmetric. The free energy, to fourth order, then takes the form  $\mathcal{F} = \mathcal{F}_M + \mathcal{F}_S + \mathcal{F}_C + \mathcal{F}_P$ , with

$$\mathcal{F}_M = (T/T_c - 1)L_1^2 + (T/T_c - 1)L_2^2 + (L_1^2 + L_2^2)^2, \quad (6.1)$$

$$\mathcal{F}_S = \frac{1}{2}(e_1^2 + e_2^2) + e_1^3 - e_1 e_2^2 + (e_1^2 + e_2^2)^2, \quad (6.2)$$

$$\mathcal{F}_P = \frac{\omega^2}{2}Q^2 + Q^3 + Q^4, \quad (6.3)$$

$$\begin{aligned} \mathcal{F}_C = & (L_1^2 - L_2^2)e_1 - L_1 L_2 e_2 + (L_1^2 + L_2^2)(e_1^2 + e_2^2) \\ & + L_1 L_2 e_1 e_2 + (L_1^2 + L_2^2)(Q + Q^2) + (e_1^2 + e_2^2)(Q + Q^2) \\ & + (L_1^2 - L_2^2)e_1 Q - L_1 L_2 e_2 Q + e_1^3 Q - e_1 e_2^2 Q. \end{aligned} \quad (6.4)$$

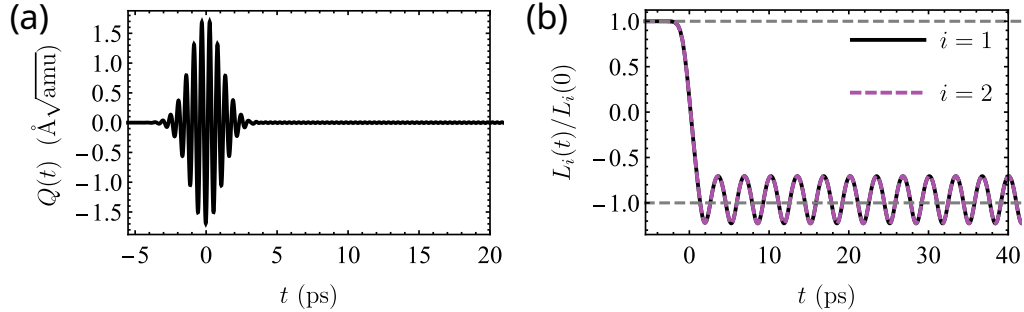


Figure 6.6: (a) Phonon mode and (b) AFM OP following photo-excitation with coupling  $(L_1^2 + L_2^2)(Q + Q^2)$ .

Each of the terms in the model  $\mathcal{F}$  is preceded by a constant whose sign and absolute value cannot be determined within group theory and are sample-dependent. The magnetic term,  $\mathcal{F}_M$ , could include anisotropic terms (due to spin-orbit coupling or single-ion anisotropies, for example), which we omit as the simplest model presented can describe the phenomenology in the experiment.

We assume that the laser excites the totally-symmetric phonon coherently via a displacive excitation mechanics [? ]. The laser-phonon coupling term is given by  $\mathcal{F}_l = E_0 \eta(t) Q$ , where  $\eta(t) = \kappa \int_0^\infty g(t-\tau) e^{-\beta\tau} d\tau$ , and  $g(t)$  is the laser pulse shape, and  $\beta$  is a parameter associated with rate of electronic relaxation to the groundstate. The differential equations governing the system can be obtained by taking the variation of the  $\mathcal{F} + \mathcal{F}_l$  potential with respect to the AFM OPs, strain, and phonon. For the results in the main text, we include phenomenological damping. The equations of motion are  $-\delta(\mathcal{F} + \mathcal{F}_l)/\delta\chi_i = \partial_t^2 \chi_i(t) + \gamma_i \partial_t \chi_i(t)$ , where  $\chi = \{Q, L_1, L_2\}$  and  $\gamma_i$  is the damping coefficient.

#### *Phonon coupling effect.*

First, we assume that there is no strain in the sample. The only term linking the AFM OP to the time-dependent phonon is  $(L_1^2 + L_2^2)(Q + Q^2)$ . We find that this term can lead to flips of  $L_1$  and  $L_2$  by 180 degrees for long-enough laser pulses. Fig. 6.6(a) shows the phonon dynamics following photo-excitation with a 1eV pulse and duration  $\tau = 1.1$  ps. The phonon frequency was assumed to be  $\omega/(2\pi) = 3$  THz, and the initial temperature

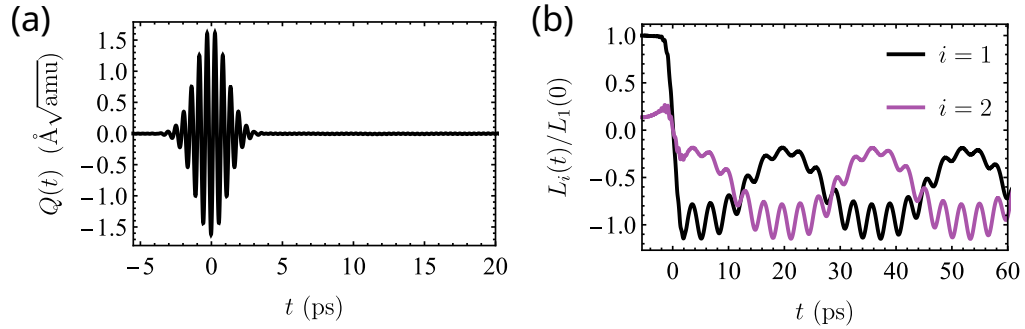


Figure 6.7: (a) Phonon mode and (b) AFM OP following photo-excitation with coupling  $L_1 L_2 e_2 Q$ .

is  $T = 0$ .

#### Strain

The presence of strain mediates coupling terms between the phonon and the AFM OP that can lead to orientations absent in equilibrium. In particular, the coupling term  $L_1 L_2 e_2 Q$  induces a solution where the components  $L_1, L_2$  oscillate around a position distinct to the initial configuration and to 180-degree flips. We consider a pulse with duration  $\tau = 1.2$  ps, phonon frequency  $\omega/(2\pi) = 3$  THz,  $T = 0$ , and strains  $\epsilon_1 = 0.01, \epsilon_2 = 0.05$ . The long-time average of  $L_2(t)$  acquires values comparable with  $L_1(t)$ , as seen in Fig. 6.7(b).

### 6.10.2 Nonviability of secondary order parameter in describing the RA-SHG data

Using a combination of PTMB and RA-SHG, we argue in the main text that, in equilibrium, the magnetism in  $\text{CaMn}_2\text{Bi}_2$  that we observe is described by a spatial distribution of four domains  $A, B, C$ , and  $D$ , for which the order parameters satisfy the relations  $l_A = -l_B, l_C = -l_D$ , and  $l_C = R(l_A)$ , where  $R$  is an element of the high-temperature point group  $\bar{3}m$ . In this scenario, the contrast in SHG between e.g.  $l_A$  and  $l_B$  comes from the fact that there can be two contributions to the RA-SHG signal which interfere

with each other and transform differently as  $l_A \rightarrow l_B$ . That is, we can write

$$I_{\text{SHG}} \propto |e_i^{\text{out}} \chi_{ijk} e_j^{\text{in}} e_k^{\text{in}}|^2, \quad (6.5)$$

where

$$\chi_{ijk} \equiv \chi_{ijk}^\alpha + \chi_{ijk}^\beta, \quad (6.6)$$

$$\begin{aligned} T(\chi_{ijk}^\alpha) &= -\chi_{ijk}^\alpha, \\ T(\chi_{ijk}^\beta) &= \chi_{ijk}^\beta, \end{aligned} \quad (6.7)$$

$T$  is the time-reversal operator which takes  $l_A \rightarrow -l_A = l_B$ , and  $e^{\text{in}}$  and  $e^{\text{out}}$  are unit vectors in the direction of the polarization of the incoming and outgoing electric fields, respectively.

An important question thus arises: what is the origin of the two sources  $\chi^\alpha$  and  $\chi^\beta$ ? The simplest explanation is that both contributions are due to the AFM OP; the relations in Eq. 6.7 are then permitted below  $T_c$ , where time-reversal symmetry is broken and so  $\chi_{ijk}$  can, in general, have parts which transform as both even and odd under time-reversal. However, an alternative interpretation is that there are in fact two OPs  $l$  and  $g$ , with  $g$  being e.g. some structural OP, so that, e.g.

$$\begin{aligned} \chi^C &\propto l + g, \text{ and} \\ \chi^D &\propto l + Rg, \end{aligned} \quad (6.8)$$

for some  $R \in \bar{3}m$ .

In this interpretation, alternative descriptions of the time-resolved results, involving e.g. a melting of  $g$  while the  $l$  stays fixed, may explain Fig. 6.3, but not imply a reorientation of  $l$  as we claim in the main text. However, we argue that such an interpretation is not a viable description of our results, both in and out of equilibrium. This can be understood by considering the fact that the RA-SHG pattern in Fig. 6.2(f) has nodes at  $\phi = 0$  and  $\phi = \pi$  for all temperatures below  $T_c$  (see Fig. 6.20). In the case  $Rg = -g$ , this suggests that, if there are indeed two independent order parameters contributing to the RA-SHG pattern, their amplitudes must exactly cancel for all  $T < T_c$ . This is unlikely as the two independent order parameters should in general depend differently on temperature. Moreover, the case  $Rg \neq -g$  is difficult to reconcile in light of the result that the PTMB signal is invariant under thermal cycling. In nonequilibrium, any scenario involving the melting of one OP while the other stays fixed must

also be reconciled with the observation that the nodes in Fig. 6.3(c) in the initial state (before  $t = 0$ ) become peaks in the final state.

Furthermore, the above interpretation must also explain how the final state of the transition seems to differ from sample to sample (as explained in the main text; see Figs. 6.18 and 6.19), as well as how the RA-SHG is poled in equilibrium to only two of many different degenerate states. Both of these facts fall out naturally from the assignment presented in the main text.

Together with the lack of a change in the XRD across  $T_c$  (see Fig. 6.13), the above considerations suggest that the scenario presented in the main text, which neatly describes the data both in and out of equilibrium, is the most likely. Future studies will be required to completely truly rule out all alternative scenarios.

### 6.10.3 Fits to susceptibility tensors

In the text, it was remarked that the OP assignment depicted in Figs. 6.2–6.3 was consistent with the SHG susceptibility tensors extracted by fitting the RA-SHG patterns. In this section, we state how this fitting was performed.

Before that discussion, however, we must mention one important point about the predictive power of these fits. Since the low-temperature point group of CaMn<sub>2</sub>Bi<sub>2</sub> is  $\bar{1}'$ , the relevant susceptibility tensors are entirely unconstrained and the cost function to be minimized may involve upward of 36 free parameters. Thus, in principle, many combinations of parameters may fit the data appropriately, thereby limiting the extent to which the SHG fits can be used to draw conclusions about the underlying state. One must look to other arguments, e.g. involving PTMB, to draw useful conclusions about the data, as was done in the text. However, once a conclusion has been made, it can at least be checked that a set of fitting parameters *does* exist that is consistent with the conclusion and with the data. This is the goal of this section.

The OP assignment discussed in the text involves two parts. In the first part, the equilibrium SHG in the four domains of Fig. 6.2 is assigned to four different OP directions, in which the SHG on consecutive cooldowns on a single spot is due to 180° AFM configurations, and adjacent spots have a relative angle between them. As argued in the text, since the 180° domains have different RA-SHG patterns, there are most likely two

contributions to the SHG adding coherently to give an interference term, as observed in other magnetic systems[? ? ? ]. Designating the four configurations as  $A$ ,  $B$ ,  $C$ , and  $D$  (for Fig. 6.2(d), Fig. 6.2(e), Fig. 6.2(f), and Fig. 6.2(g), respectively), we thus have

$$\begin{aligned}\chi_{ijk}^A &= \chi_{ijk}^\alpha + \chi_{ijk}^\beta \\ \chi_{ijk}^B &= -\chi_{ijk}^\alpha + \chi_{ijk}^\beta \\ \chi_{ijk}^C &= R(\chi_{ijk}^\alpha + \chi_{ijk}^\beta) \\ \chi_{ijk}^D &= R(-\chi_{ijk}^\alpha + \chi_{ijk}^\beta),\end{aligned}\tag{6.9}$$

where  $\chi^\alpha$  is the susceptibility tensor related to the magnetic order[? ],  $\chi^\beta$  is the susceptibility tensor corresponding to the secondary component discussed above, and  $R(\cdot)$  refers to an operation by some element  $R$  of the high-temperature point group ( $\bar{3}m$ ), i.e.

$$R(\chi_{ijk}) \equiv R_{il}R_{jm}R_{kn}\chi_{lmn}.$$

In the time-resolved case, 6.9 should hold before zero delay, and a similar set of equations should hold after zero delay in the final state:

$$\begin{aligned}\chi_{ijk}^{A'} &= \alpha\chi_{ijk}^\alpha + \chi_{ijk}^\beta \\ \chi_{ijk}^{B'} &= -\alpha\chi_{ijk}^\alpha + \chi_{ijk}^\beta \\ \chi_{ijk}^{C'} &= \alpha\chi_{ijk}^\alpha + \chi_{ijk}^\beta \\ \chi_{ijk}^{D'} &= \alpha\chi_{ijk}^\alpha + \chi_{ijk}^\beta.\end{aligned}\tag{6.10}$$

Here,  $\alpha$  is an overall factor to account for the fact that the magnitude of the OP may change due to heating following the transition. We also allow a relative scale (close to unity) between  $A$  /  $B$  /  $A'$  /  $B'$  and  $C$  /  $D$  /  $C'$  /  $D'$  to account for the fact that these are taken on different spots on the sample.

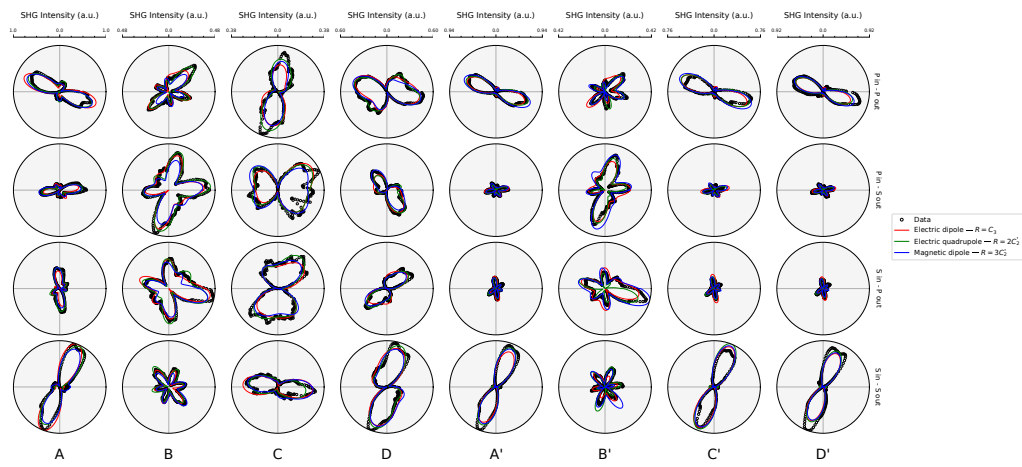


Figure 6.8: Fits to the RA-SHG pattern in the four domains of Fig. 6.2 2.0 ps before ( $A, B, C, D$ ) and  $\sim 40$  ps after ( $A', B', C', D'$ ) zero delay. Data is represented by black circles; solid lines are fits to Eqs. 6.5 and 6.6 with  $\chi^\beta$  denoted in the legend.

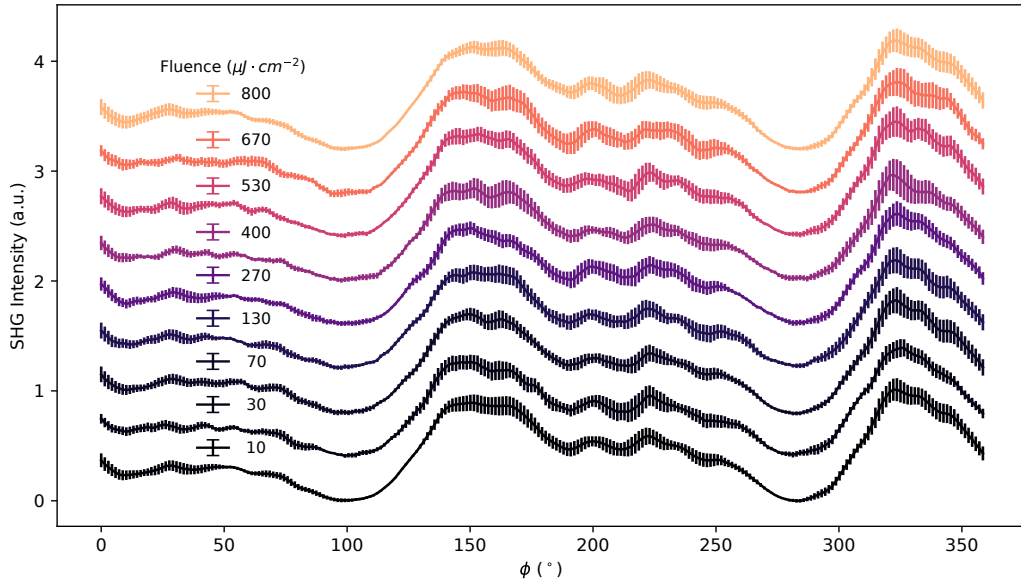


Figure 6.9: RA-SHG results of Fig. 6.11 depicted with estimated errorbars (see text).

For  $\chi_{ijk}^\alpha$ , we use the totally asymmetric complex electric dipole SHG tensor in the point group  $\bar{1}'$ , which has 36 independent elements. In the language of [?], this would be referred to as a *c*-type tensor and should have purely imaginary components; however, in the presence of dispersion or dissipation, complex components are also allowed. For  $\chi_{ijk}^\beta$ , many options are possible, including an *i*-type electric dipole component, electric quadrupole component, or magnetic dipole component, each of which may couple with the AFM OP. With each of these options for  $\chi^\alpha$  and  $\chi^\beta$ , we fit the RA-SHG data at  $\Delta t = -2$  ps and at long times ( $\Delta t \approx 40$  ps). It is found that all possibilities for  $\chi^\beta$  produce an appropriate fit to the data (see Fig. 6.8).

#### 6.10.4 Error bar estimation for Fig. 6.11

The errorbars in Fig. 6.9 are ultimately due to uncertainty in the value of the SHG intensity at each angle  $\phi$ . When these angles are integrated over, the associated uncertainties in the SHG intensity are summed in quadrature. To extract the uncertainties in the SHG intensity as a function

of angle is a somewhat difficult process, as these uncertainties are largely systematic rather than statistical. Indeed, the RA-SHG pattern should in general be a smooth function of  $\phi$ ; however, it is seen (e.g. Fig. 6.3(d)) that the RA-SHG patterns are not necessarily smooth. We therefore estimate the size of the errorbars using more heuristic methods, which, while imprecise, should at least give a rough approximation to the true uncertainty.

These heuristic errorbars in the SHG intensity are found by estimating the size of the variations in the RA-SHG pattern compared to a smoothed approximation (approximated with an  $N = 6$  FFT filter). The errorbars computed this way are shown in Fig. 6.9.

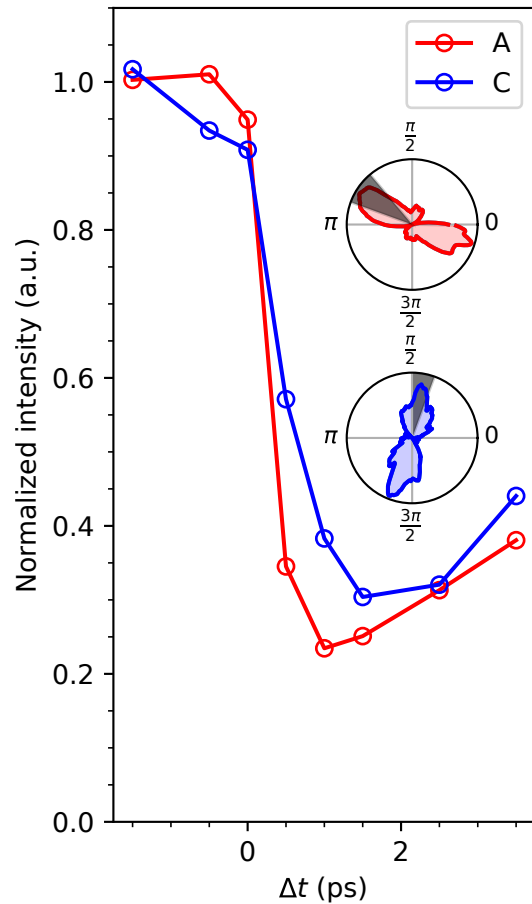


Figure 6.10: Integrated SHG intensity as a function of time corresponding to Fig. 6.4(a) (A, red) and Fig. 6.4(c) (C, blue). Insets show the equilibrium SHG patterns in the  $P_{\text{in}}P_{\text{out}}$  polarization combination for the two domains, with the integration region indicated in gray. The  $y$ -axis normalization for either domain is defined such that the average signal before zero delay equal to 1.0.

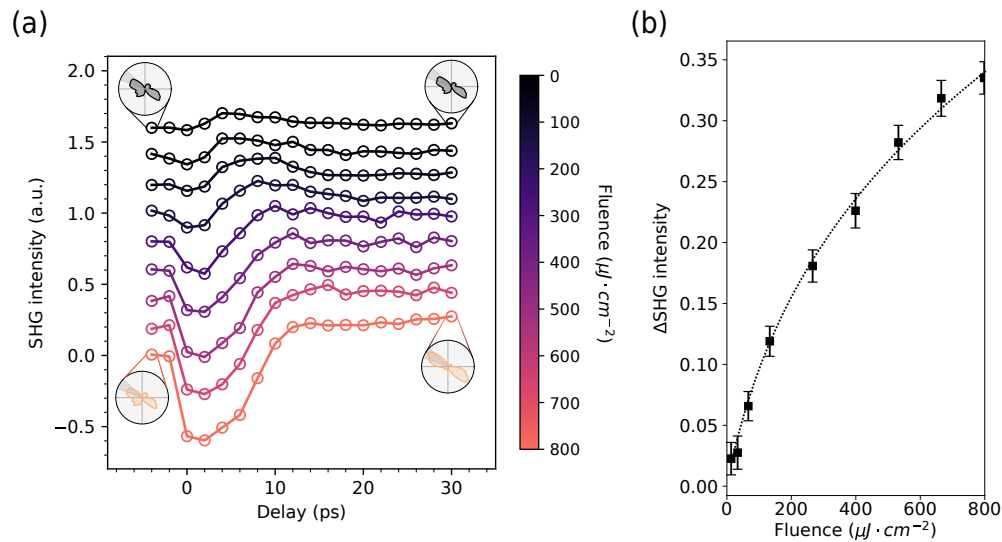


Figure 6.11: (a) Integrated SHG intensity for a representative AFM domain as a function of delay and pump fluence. Insets show the initial (left) and final (right) states at high (bottom) and low (top) pump fluences, as well as the integration region (indicated by the shaded area). (b) Difference between the intensity of the integration region specified in 6.11(a) at long times (averaged from  $\Delta t = 40$  to  $\Delta t = 50$  ps) and the intensity before zero delay (averaged from  $\Delta t = -4$  to  $\Delta t = -2$  ps). Dashed line is a guide to the eye.

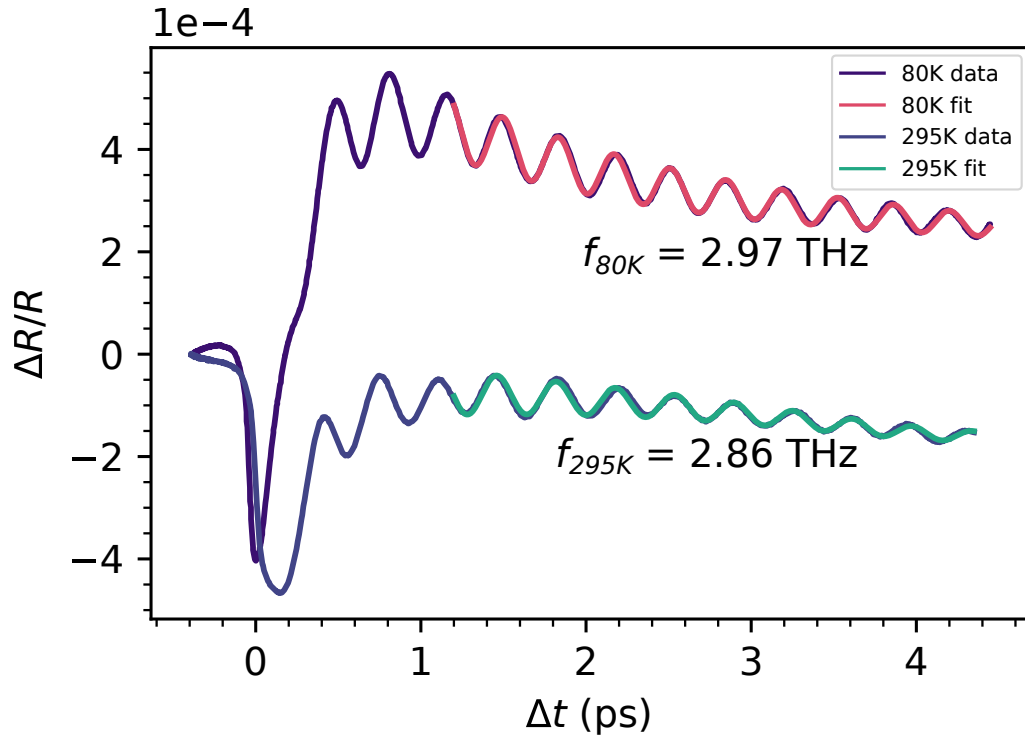


Figure 6.12: Time-resolved reflectivity obtained from  $\text{CaMn}_2\text{Bi}_2$  at 80 K and 295 K. The pump and probe wavelengths were both 800 nm, the pulse width was 28 fs, and the pump and probe fluences were 10 and  $1 \mu\text{J} \cdot \text{cm}^{-2}$ , respectively. The data is windowed after the initial transients and then fit to a damped harmonic oscillator plus a polynomial background.

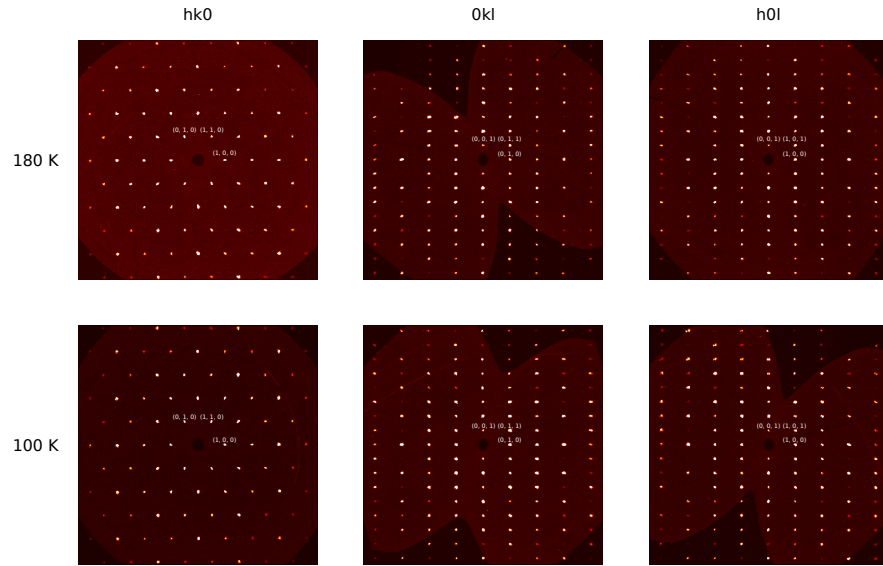


Figure 6.13: Single-crystal XRD precession images obtained from  $\text{CaMn}_2\text{Bi}_2$ . The high temperature refinement is in agreement with previous reports[? ]. No change in the crystal structure is observed across  $T_c = 150 \text{ K}$ .

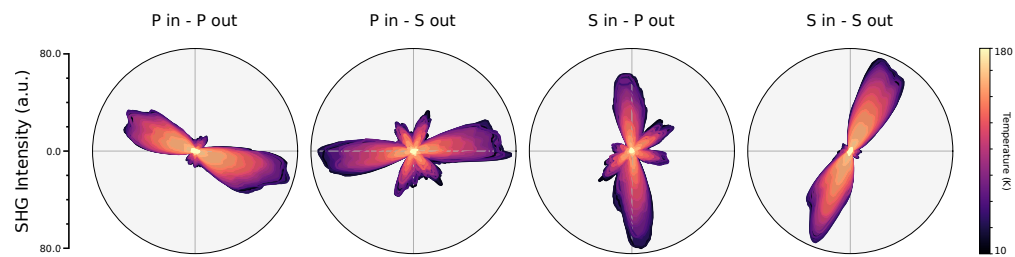


Figure 6.14: RA-SHG results of Fig. 6.1 depicted in all four polarization channels ( $P_{\text{in}}P_{\text{out}}$ ,  $P_{\text{in}}S_{\text{out}}$ ,  $S_{\text{in}}P_{\text{out}}$ , and  $S_{\text{in}}S_{\text{out}}$ )

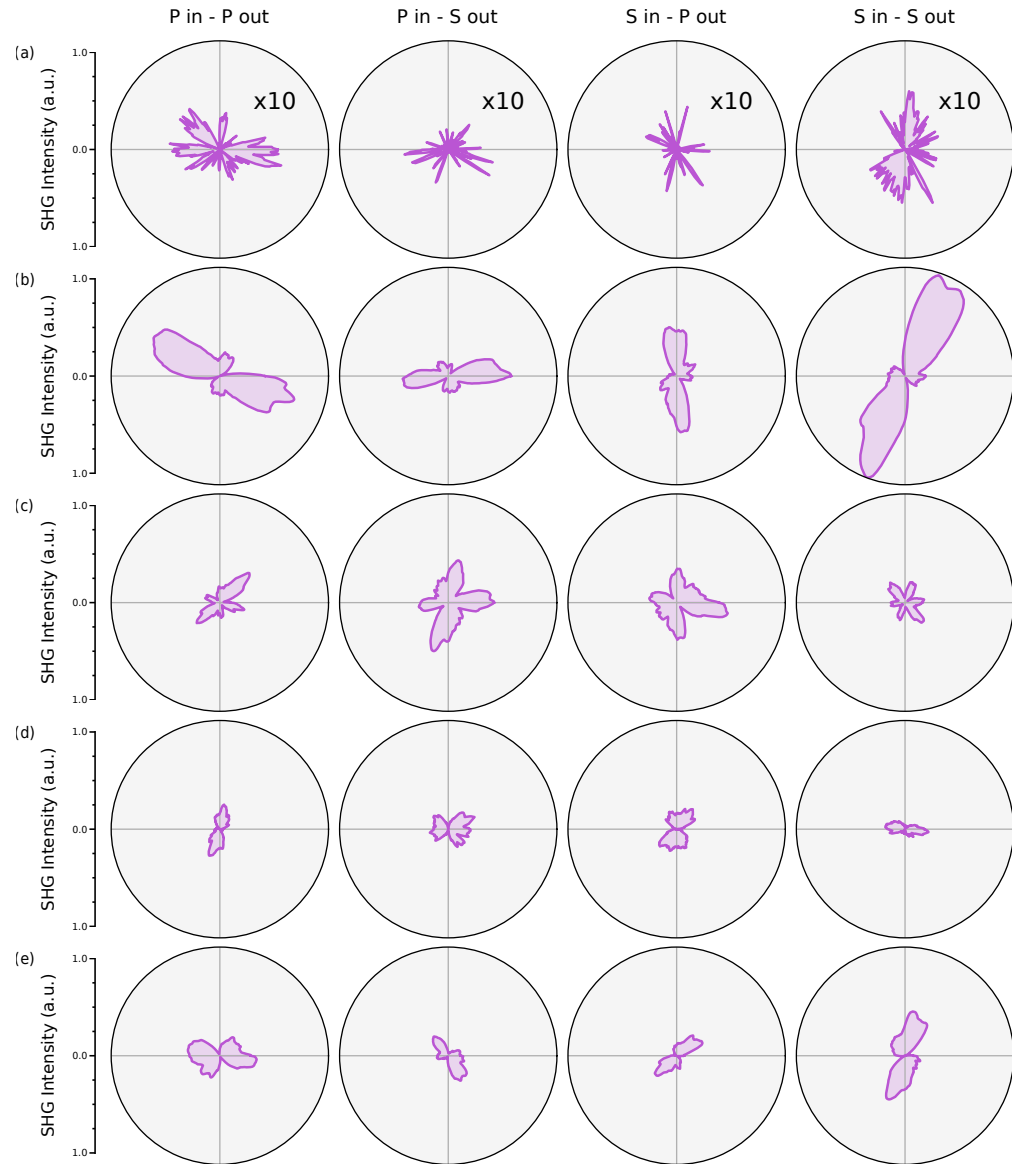


Figure 6.15: (a) (b) (c) (d) (e) RA-SHG results of Figs. 6.2(b) and 6.2(d)–g) depicted in all four polarization channels ( $P_{\text{in}}P_{\text{out}}$ ,  $P_{\text{in}}S_{\text{out}}$ ,  $S_{\text{in}}P_{\text{out}}$ , and  $S_{\text{in}}S_{\text{out}}$ ).

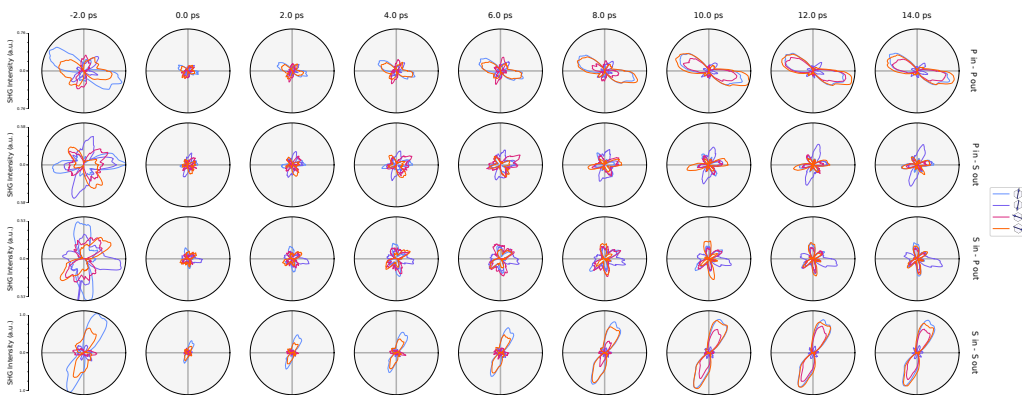


Figure 6.16: RA-SHG results of Fig. 6.3 depicted in all four polarization channels ( $P_{\text{in}}P_{\text{out}}$ ,  $P_{\text{in}}S_{\text{out}}$ ,  $S_{\text{in}}P_{\text{out}}$ , and  $S_{\text{in}}S_{\text{out}}$ ). The pump fluence is set to  $\sim 600 \mu\text{J} \cdot \text{cm}^{-2}$ .

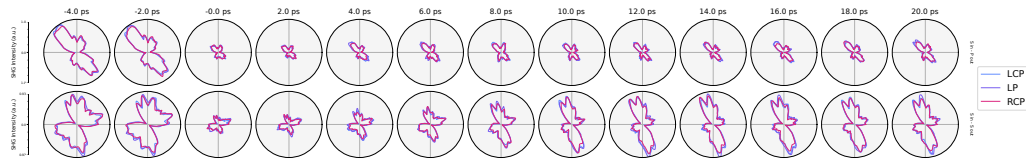


Figure 6.17: RA-SHG results in a representative domain as a function of time for different pump polarization states (left circularly- (LCP), right circularly- (RCP), and linearly-polarized). The pump fluence is set to  $\sim 600 \mu\text{J} \cdot \text{cm}^{-2}$ .

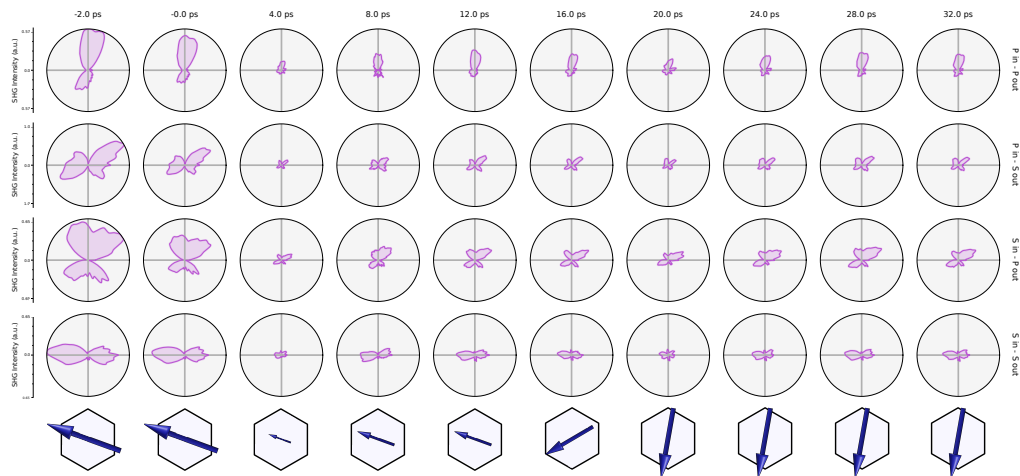


Figure 6.18: RA-SHG snapshots showing a transition to the state opposite to Figs. 6.3(c–d). The pump fluence is set to  $\sim 600 \mu\text{J} \cdot \text{cm}^{-2}$ . The last row depicts the corresponding value of the AFM OP proposed in the text, relative to the hexagonal crystallographic motif. The schematic representations beneath the RA-SHG plots are for illustration purposes only and the depicted angles are not quantitatively verified.

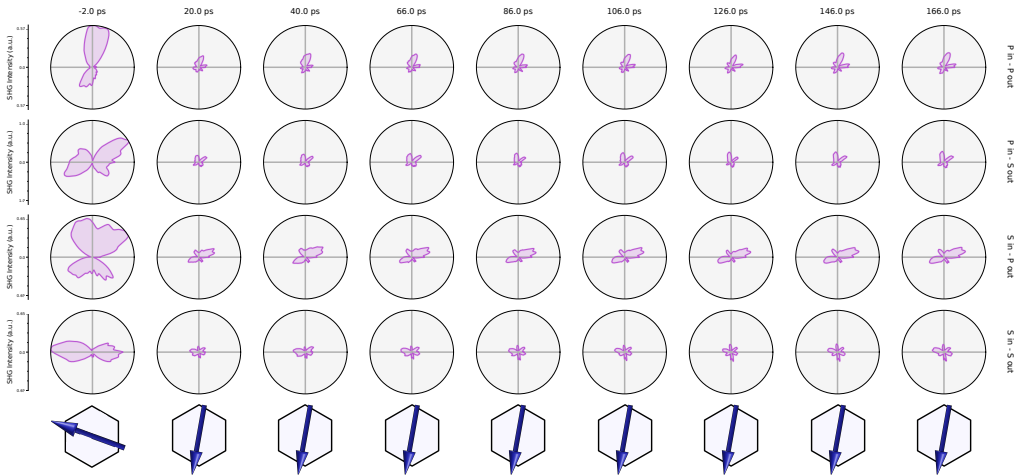


Figure 6.19: RA-SHG results in the same domain as Fig. 6.18 plotted out to longer times. The pump fluence is set to  $\sim 600 \mu\text{J} \cdot \text{cm}^{-2}$ . The last row depicts the corresponding value of the AFM OP proposed in the text, relative to the hexagonal crystallographic motif. The schematic representations beneath the RA-SHG plots are for illustration purposes only and the depicted angles are not quantitatively verified.

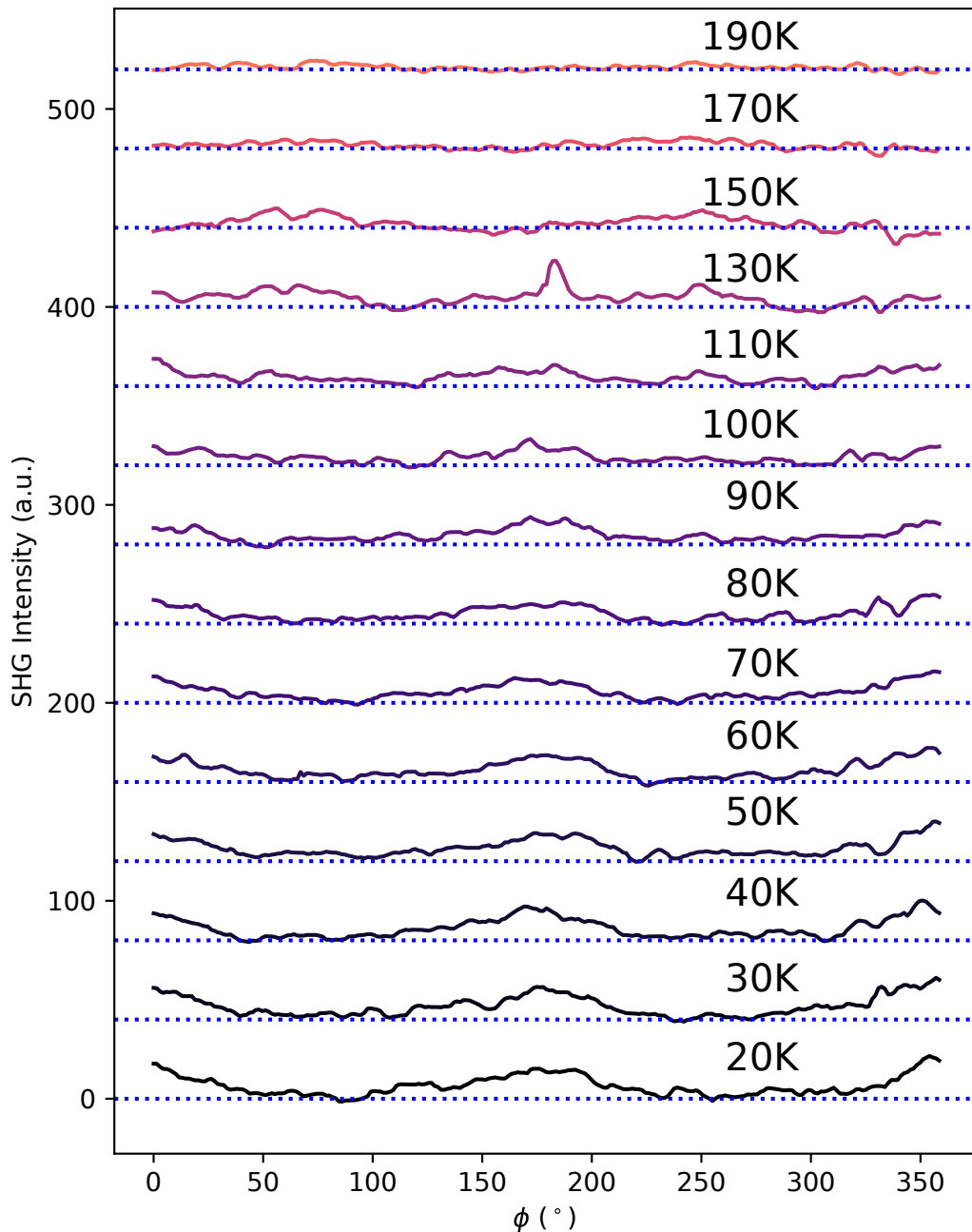


Figure 6.20: SHG intensity in the same domain as Fig. 6.2(f) as a function of temperature.

## Chapter 7

---

### *Amplitude-mode electromagnon in the spin-spiral multiferroic CuBr<sub>2</sub>*

#### **7.1 Preface**

This chapter is based on a manuscript intended for standalone publication and modified to fit the format of this thesis. It was coauthored by myself, Ajesh Kumar, and Baiqing Lv (as co-first authors), as well as Zongqi Shen, Karna Morey, Qian Song, Riccardo Comin, Todadri Senthil, and Nuh Gedik. Myself, Baiqing Lv, Zonqi Shen, and Karna Morey took the tr-SHG measurements, under the supervision of Nuh Gedik. Myself and Ajesh Kumar did the theory and analyzed the data, under the supervision of Nuh Gedik and Todadri Senthil. Qian Song grew the samples, under the supervision of Riccardo Comin. Myself and Ajesh Kumar wrote the paper, and Nuh Gedik supervised the project.

#### **7.2 Abstract**

Below a spontaneous symmetry breaking phase transition, the relevant collective excitations may be described as fluctuations in the amplitude and phase of the order parameter, referred to as amplitude and Goldstone modes, respectively. In solids, these modes may take on a different character than the equivalent excitations in particle physics due to the diverse vacuum states accessible in condensed matter. However, the amplitude mode in particular is quite difficult to observe experimentally as it decays quickly into the lower-energy Goldstone bosons and thus has a negligible lifetime in most systems. In this work, we report evidence for a novel amplitude mode in the multiferroic material CuBr<sub>2</sub>, which shows up as a coherent oscillation in the time-resolved SHG signal upon excitation with a femtosecond light pulse. Since the spiral spin order in CuBr<sub>2</sub> in-

duces a nonzero electric dipole moment in equilibrium, the amplitude mode—which is due to fluctuations in the amplitude of the on-site spin expectation value—is an electromagnon, and thus acquires an inversion quantum number of  $-1$ . This is in stark contrast to the amplitude boson of particle physics, which has even parity. Moreover, the excitation described here represents an entirely new type of electromagnon, distinct from the traditional electromagnon in linear spin wave theory which is due to the Goldstone mode. We argue that the amplitude mode in CuBr<sub>2</sub> acquires a nontrivial lifetime due to the combination of two features: (i) the quasi-1D nature of the material, and (ii) proximity at zero temperature to a quantum critical point separating the multiferroic ground state from a topological Haldane dimer phase.

### 7.3 Introduction

When the ground state of a given theory fails to respect one of its symmetries, that symmetry is said to have been broken spontaneously[? ? ]. The low-energy excitations of this ground state may then be described as excitations of the order parameter either within the subspace of degenerate ground states, or perpendicular to it; these excitations are referred to as Goldstone and amplitude modes, respectively[? ] (see Fig. 7.1(a)). This paradigm describes many fundamental phenomena in both particle physics and condensed matter, and the study of these modes has thus emerged as an essential pursuit in both contexts.

A rich interplay exists between these two fields due to the fact that in particle physics we are limited to a single theory (the standard model), but in condensed matter, the theory is determined by the particular system of interest and may differ dramatically from one material to another. Thus, various exotic species of amplitude modes may be studied simply by exploring different material systems with spontaneous symmetry breaking. An important example is in multiferroics, where it has been predicted[? ? ] that the amplitude mode of the magnetic order (corresponding to modulations in the amplitude of the on-site spin excitation value, see Fig. 7.1(b)) should couple to the macroscopic polarization as an electromagnon, and thus acquire a negative parity eigenvalue. This is not the case for the Higgs boson of the standard model, which is of even parity[? ]. In addition to its connection to particle physics, the excitation described

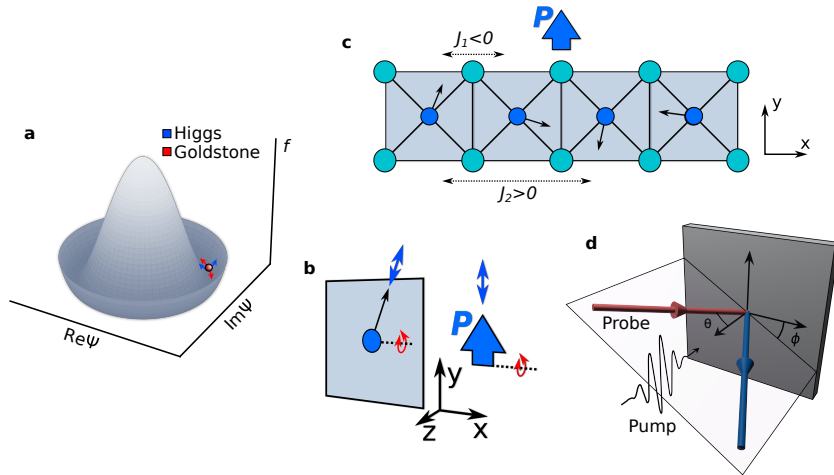


Figure 7.1: (a) Mexican hat potential with amplitude and Goldstone modes indicated. (b)  $q = 0$  electromagnons in the quasi-1D spin-spiral in the spin (left) and charge (right) sectors. The amplitude and Goldstone modes are shown in blue and red, respectively. A second Goldstone mode, corresponding to uniform rotations of the spins about the  $z$  axis (which does not affect the polarization  $\vec{P}$ ), is not shown. (c) Magnetic ground state of  $\text{CuBr}_2$ . The macroscopic polarization due to the spin order is depicted with a blue arrow. The axis labelled  $x$  is parallel to the nominal  $b$  axis of the crystal structure. (d) Schematic of the tr-SHG experimental geometry.

here is also fundamentally different from the traditional electromagnon in multiferroics (which is due to the (pseudo-)Goldstone mode[?]), and is thus of great interest for magnetoelectric device applications. Unfortunately, like in particle physics, the amplitude mode in condensed matter is difficult to observe since it may quickly decay into Goldstone bosons upon excitation[?], and the existence of this mode in real multiferroic systems has thus remained an important open question.

In this work, we report evidence for this mode in  $\text{CuBr}_2$  (a quasi-1D, spin-spiral multiferroic, see Fig. 7.1(c)), observed by launching a coherent oscillation of this mode with a near-infrared light pulse and measuring the induced modulations in the electric polarization using a

delayed SHG probe pulse (Fig. 7.1(d)). We find, as expected, that the mode modulates the macroscopic polarization only along the static ordering direction, and that the frequency of the mode decreases on approaching the critical temperature of the multiferroic order. These results provide conclusive evidence for the existence of this electromagnon in CuBr<sub>2</sub>, solving a decade-old puzzle and paving the way for future study of the amplitude mode in novel condensed-matter contexts.

## 7.4 Results

### 7.4.1 Equilibrium

The low-energy spin Hamiltonian of CuBr<sub>2</sub> is well approximated by the so-called frustrated 1D XXZ spin chain, where localized spin-1/2 electrons interact ferromagnetically ( $J_1 < 0$ ) with nearest neighbors but antiferromagnetically ( $J_2 > 0$ ) with next-nearest neighbors (see Fig. 7.1(c)). When these interaction strengths are of comparable magnitude, the ground state is an incommensurate magnetic spiral, where the ordering wavevector is directed along the chain direction and has the appropriate magnitude so as to balance the two competing interaction terms. According to theory developed by Katsura, Nagaosa, and Balatsky[?], when spin-orbit coupling is strong this ground state induces an electric polarization at each site  $n$  given by

$$\vec{P}^n \propto \hat{x} \times (\vec{S}^n \times \vec{S}^{n+1}), \quad (7.1)$$

where we have set the chain direction to lie along  $\hat{x}$ . If the spins lie in the  $xy$  plane, then Eq. 7.1 induces a macroscopic electric polarization which is equal for each bond and directed purely along the  $\hat{y}$  direction (Fig. 7.1(c)).

According to powder neutron diffraction, this spiral magnetic phase is realized in CuBr<sub>2</sub> below  $T_c = 75$  K [? ? ? ?], with the propagation vector (in reciprocal lattice units) given by  $\vec{k} = (0, k_y, 0.5)$ , with  $k_y \sim 0.235$ [? ?]. A pyroelectric current turns on at this temperature as well, indicating a macroscopic electric polarization density  $|\vec{P}_0|$  of about  $8 \mu\text{C}/\text{m}^2$  at 10 K[? ].

In a generalized Ginzburg-Landau theory, the SHG susceptibility tensor  $\chi_{ijk}$  is linearly proportional to this polarization:

$$\chi_{ijk}(T < T_c) = \chi_{ijkl}(T > T_c)P_{0l} = \chi_{ijk}y(T > T_c)P_0, \quad (7.2)$$

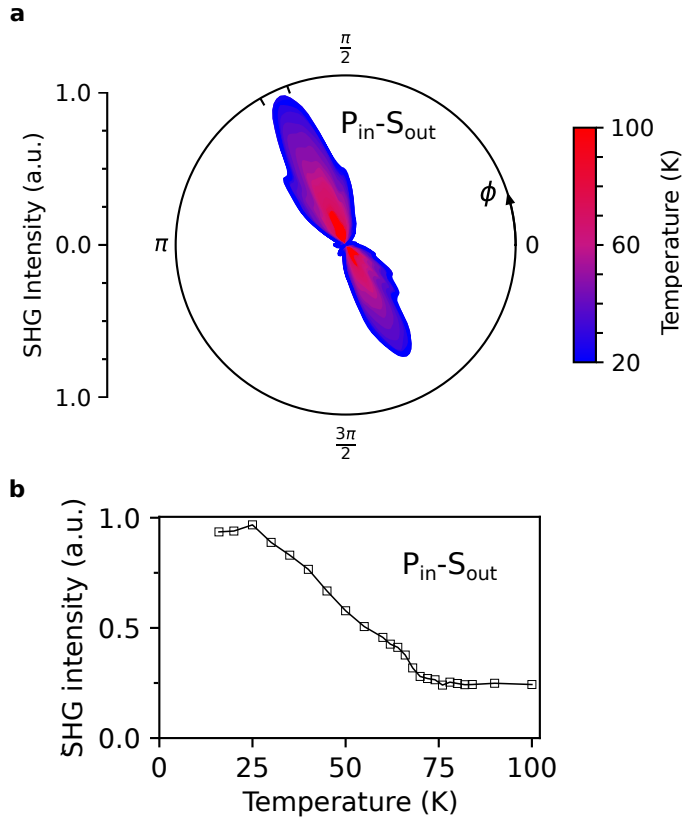


Figure 7.2: (a) SHG intensity as a function of temperature in the  $P_{in}S_{out}$  polarization channel. (b) Integrated SHG intensity in the region near  $\pi/2$  of 7.2(a) marked by the tick marks.

where  $\chi_{ijkl}$  is some unknown tensor with the symmetry of the high temperature phase[? ], and we have used that  $\vec{P}_0 \parallel \hat{y}$ . Fig. 7.2 shows the temperature dependence of the SHG intensity in CuBr<sub>2</sub>, indicating a pronounced, order parameter-like enhancement of the SHG intensity at  $T_c$  due to Eq. 7.2. Note that other contributions to the SHG intensity due to e.g. magnetic dipole, surface electric dipole, and electric quadrupole terms are allowed above and below  $T_c$  and thus cannot explain the intensity increase below  $T_c$ . In addition, the *c*-type electric dipole term purely due to the magnetic order[? ] is also not allowed by the magnetic point group of the incommensurate spin spiral (see Supplementary material,

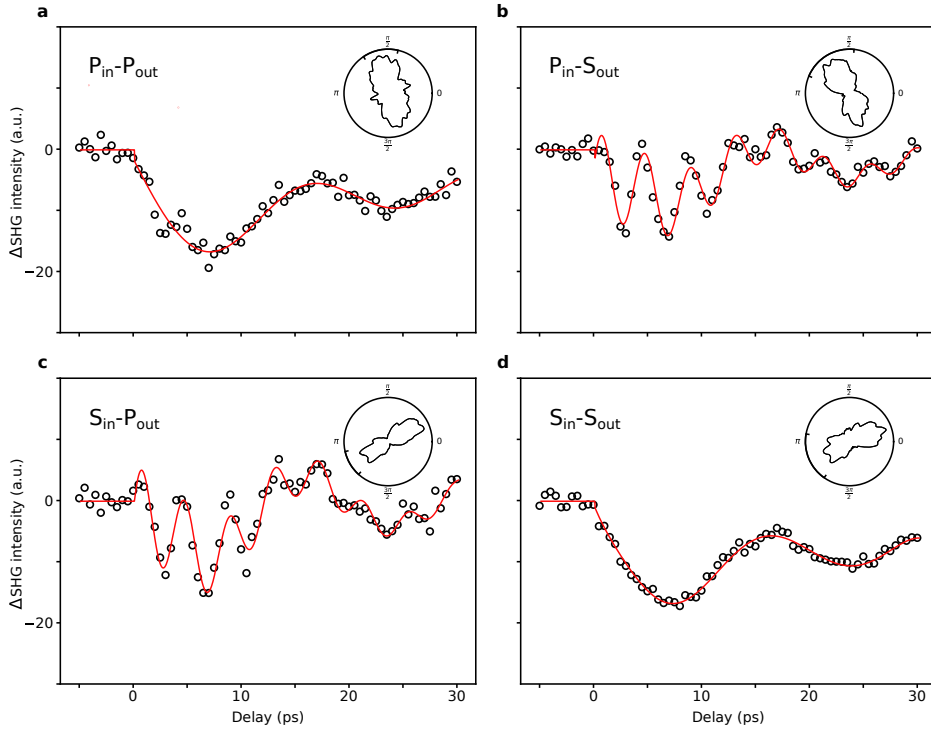


Figure 7.3: Pump-induced change in the SHG intensity at 15 K in the four polarization channels (a)  $P_{\text{in}}P_{\text{out}}$  (b)  $P_{\text{in}}S_{\text{out}}$  (c)  $S_{\text{in}}P_{\text{out}}$ , and (d)  $S_{\text{in}}S_{\text{out}}$ . Insets depict the static SHG intensity in each polarization channel. The time-domain signals are computed by performing an azimuthal integration at each delay of the full SHG pattern over the angles specified by the additional tick marks in each inset.

Section 7.8.6.3).

## 7.4.2 Nonequilibrium

Having thus demonstrated that the SHG intensity is a direct probe of the electric polarization in CuBr<sub>2</sub>, we proceed to investigate the low-energy collective excitations in this phase. To do so, we excite the sample with a 150 fs near-infrared pump pulse, and then probe the SHG intensity with a second pulse delayed in time by an amount  $\Delta t$ . We carry out

this procedure in each of four independent polarization channels ( $P_{\text{in}}P_{\text{out}}$ ,  $P_{\text{in}}S_{\text{out}}$ ,  $S_{\text{in}}P_{\text{out}}$ , and  $S_{\text{in}}S_{\text{out}}$ , see Section 7.7), where each channel probes a different linear combination of the tensor elements  $\chi_{ijk}$ . The results are shown in Fig. 7.3. Two oscillations, with different dependencies on the SHG polarization channel, may be observed: one high-frequency mode ( $\nu \sim 0.23 \text{ THz}, \hbar\omega \sim 1.0 \text{ meV}$ ), which is only observed in the crossed polarization channels  $P_{\text{in}}S_{\text{out}}$  and  $S_{\text{in}}P_{\text{out}}$ , and one low-frequency mode ( $\nu \sim 0.05 \text{ THz}, \hbar\omega \sim 0.20 \text{ meV}$ ), which occurs in all polarization channels equally. Both of these are too low to be observed with typical THz or neutron spectroscopies, yet they are readily apparent in the tr-SHG data due to the pump-probe nature of the experiment.

To show that these two modes are directly related to the multiferroic transition at  $T_c$ , we measure the pump-induced change in the SHG intensity as a function of  $\Delta t$  for a series of temperatures approaching  $T_c$  Fig. 7.4. By fitting the respective time-domain traces to damped harmonic oscillators (see Supplementary material, Section 7.8.3), we can extract the natural frequency of each collective mode as a function of temperature (Fig. 7.4). Both modes exhibit a pronounced softening on approaching  $T_c$ , confirming their direct involvement in the multiferroic transition. We also note that both modes disappear above  $T_c$ , which is sensible given that the macroscopic polarization  $\vec{P}_0$  also disappears above this temperature.

To clarify the microscopic origin of these polarization oscillations, we begin by performing density functional theory (DFT)+U and finite-displacement lattice dynamics calculations (see Supplementary material, Section 7.8.6.2) to compare their energies with those of the zone-center phonon modes. The lowest zone-center optical phonon in this calculation appears at 7.4 meV, in excellent agreement with Raman spectroscopy[?], and the calculated acoustic phonon branches (which agree with inelastic neutron scattering (INS)[?]) disperse too rapidly to form a zone-folded acoustic phonon mode at the  $\Gamma$  point with an energy low enough to match the frequencies observed in the tr-SHG experiment. Thus, the modes observed in Figs. 7.3 and 7.4 are not phonons. The only remaining possibility is that these modes are magnons of the incommensurate spin spiral, which imprint themselves on the polarization via Eq. 7.1; i.e., they are electromagnons.

In linear spin wave theory (LSWT), there is only one spin boson which couples to the polarization in the spiral magnetic phase of CuBr<sub>2</sub> (see Sup-

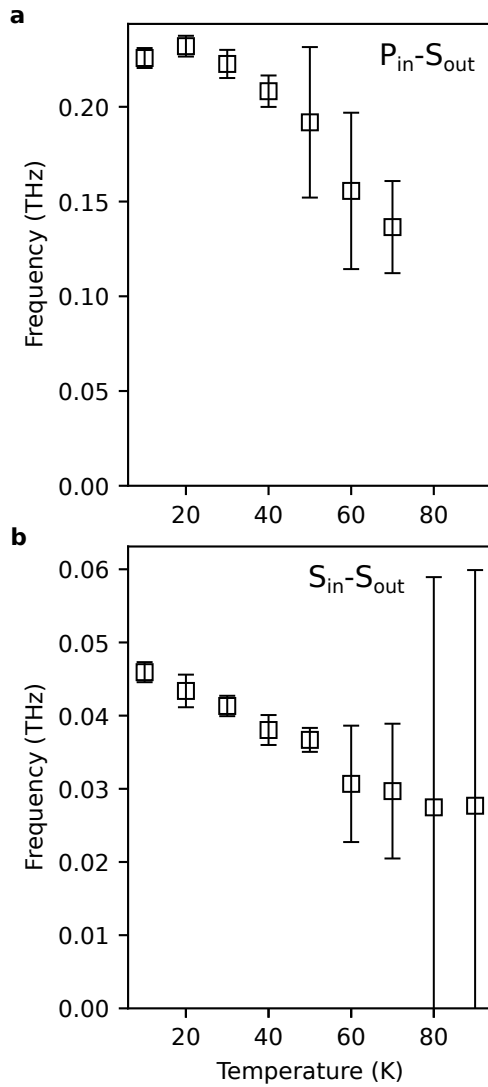


Figure 7.4: Temperature dependence of the frequencies extracted from the (a)  $P_{\text{in}}S_{\text{out}}$  and (b)  $S_{\text{in}}S_{\text{out}}$  time-domain signals (Supplementary material, Section 7.8.3) in a damped harmonic oscillator model. Error bars denote 95% confidence intervals estimated within a parametric bootstrap (see Supplementary material, Section 7.8.4).

plementary material, Section 7.8.1); it is the so-called pseudo-goldstone mode of the magnetic order[?], which corresponds to a rotation of the spin plane about the chain direction (Fig. 7.1(b)). This mode has zero energy if the system is isotropic about the chain axis, but in the presence of an anisotropy term it acquires a finite energy. In CuBr<sub>2</sub>, this energy is expected to lie around 1.25 meV (see Supplementary material, Section 7.8.2), which is close to the value observed for our high-frequency oscillation (1.0 meV). Additionally, since this mode involves a rotation of the spin plane about the chain direction, the effect of this mode (from Eq. 7.1) on the polarization is to tilt the vector  $\vec{P}_0$  into the  $\hat{z}$  direction (Fig. 7.1(b)). Since the equilibrium polarization lies along  $\hat{y}$ , Eq. 7.2 implies that a canting of the polarization  $\delta\vec{P}||\hat{z}$  involves new elements of the tensor  $\chi_{ijkz}(T > T_c)$  which are not present in equilibrium. The result is that this mode may appear in different polarization channels with different magnitudes; we thus identify the fast, 0.23 Thz oscillation in Fig. 7.3 with this mode.

The observation of a *second* mode in the tr-SHG, however, is impossible to explain in LSWT, and represents the most striking aspect of this work. To understand the origin of this second mode, we note that there are only three normal modes of the polarization which occur at the  $\Gamma$  point in the Brillouin zone, corresponding to polarization oscillations  $\delta\vec{P}$  along  $\hat{x}$ ,  $\hat{y}$ , and  $\hat{z}$ . Since the  $\delta\vec{P}||\hat{z}$  mode is already accounted for by the pseudo-goldstone mode, that leaves only  $\delta\vec{P}||\hat{x}$  and  $\delta\vec{P}||\hat{y}$  as possibilities. The  $\delta\vec{P}||\hat{x}$  mode does not couple to the spin order in this compound[?], and in any case is not observable in the geometry of our experiment (see Supplementary material, Section 7.8.6.1). Thus, the only polarization oscillation which is consistent with the observation of a second mode is an oscillation with  $\delta\vec{P}||\hat{y}$ . Since the equilibrium polarization is also directed along  $\hat{y}$ , this mode simply corresponds to an oscillation in the total amplitude of the polarization, and is thus expected to modulate the overall SHG intensity irrespective of the polarization channel – in excellent agreement with Fig. 7.3, which shows the low-frequency oscillation appearing in all four polarization channels with equal magnitude.

Naively, electromagnons with  $\delta\vec{P}||\hat{y}$  do not exist in LSWT. The key insight, however, is that LSWT neglects dynamics associated with the magnitude of the onsite spin expectation value. By Eq. 7.1, such dynamics change the magnitude of the induced polarization only, not its direction; i.e., they induce oscillations  $\delta\vec{P}||\hat{y}$ . In fact, it is possible to show (see

Supplementary material, Section 7.8.1) that oscillations along  $\hat{y}$  of the induced polarization *necessarily* involve modulations in the amplitude of the onsite spin expectation value; that is, the only mode which couples to  $\delta\vec{P}||\hat{y}$  is the amplitude mode of the magnetic spiral. Naturally, this mode should soften on approaching  $T_c$ , in agreement with Fig. 7.4. The 0.05 THz oscillation observed in our experiment (which is of similar energy to the amplitude mode in non-ferroelectric quantum magnets? []) is therefore direct evidence for this mode in CuBr<sub>2</sub>, with the additional information that it couples to the electric polarization (i.e., it is an electromagnon) via Eq. 7.1.

## 7.5 Discussion

Let us make two important remarks about this mode in CuBr<sub>2</sub>. First, we note that this mode is fundamentally distinct from the amplitude mode in non-multiferroic magnets – since the multiferroic order breaks inversion symmetry, the amplitude mode of this phase has a parity quantum number  $l = -1$  rather than  $+1$ . The static polarization  $\vec{P}_0$  which appears at  $T_c$  can thus be viewed as arising from the odd-parity nature of its amplitude mode. Second, we remark that the amplitude mode in CuBr<sub>2</sub> can in principle decay – as in non-multiferroic magnets – quite rapidly into the Goldstone modes of the magnetic order (which in the spin-spiral phase of Fig. 7.1(c) are gapless and correspond to uniform rotations of each spin about the  $\hat{z}$  direction), and thus should not exist as a well-defined quasiparticle unless these decay channels are quenched by some mechanism.

In non-multiferroic magnets, two such mechanisms have been identified. First, the amplitude mode may be stabilized by bringing the system close to a quantum critical point (QCP)[????], which suppresses the Goldstone bosons and thus stabilizes the amplitude mode. A second option is to lower the dimensionality[????]; in 1D, enhanced fluctuations weaken the long range magnetic order and also reduce the spectral weight of the Goldstone bosons[?]. In CuBr<sub>2</sub>, not only is the system fundamentally one-dimensional, but is thought also to lie in close proximity to a zero-temperature QCP[?] separating the spiral phase considered here and a paraelectric Haldane dimer phase. Both of these mechanisms thus likely contribute to stabilizing the amplitude electromagnon in CuBr<sub>2</sub>.

## 7.6 Conclusion

To summarize, we have presented evidence of a novel electromagnon arising from the amplitude mode of the spiral magnetic order in CuBr<sub>2</sub>. This mode appears alongside the pseudo-Goldstone mode in the tr-SHG data as a low-frequency oscillation in the longitudinal component of the electric polarization, which softens on warming close to  $T_c$ . Looking forward, we note that the two mechanisms we identified for stabilizing this mode in CuBr<sub>2</sub> – low dimensionality and potential proximity to a QCP – are not necessarily unique to this material. Thus, the amplitude electromagnon presented here may in fact be a common feature of 1D multiferroics, and its observation could indicate a wealth of new opportunities to explore the amplitude mode of particle physics in novel condensed-matter contexts.

## 7.7 Methods

Tr-SHG measurements were carried out using a fast-rotating optical grating setup described previously[? ? ? ]. 100 fs ultrashort pulses from a regeneratively amplified 5 kHz Ti:Sapphire laser were used to pump an OPA, producing 1300 nm (Fig. 7.3) or 1650 nm (Fig. 7.4) pump pulses which were delayed with an optical delay line and focused at normal incidence to a 300  $\mu\text{m}$ -diameter spot on the sample. The pump fluence was  $\sim 1 \text{ mJ} \cdot \text{cm}^{-2}$  for all measurements. A small portion of the Ti:Sapphire output was used for the SHG probe experiment, the output of which was spectrally filtered with a 400 nm bandpass filter, collected by a photomultiplier tube, filtered with a lock-in amplifier, and correlated with the plane of incidence angle using an optical rotary encoder. To measure the pump-induced change in the SHG signal, the pump pulses were chopped at a frequency of 2.5 kHz, and the lock-in amplifier was set to that frequency so as to measure  $I_{\text{pump+probe}} - I_{\text{probe}}$ . For the pump-probe RA-SHG measurements, the plane of incidence was rotated while the delay stage was moved and the polarizers were controlled automatically using homebuilt polarization rotators described in ? ]. For the single-angle tr-SHG measurements, the plane of incidence was parked at the angle which maximized the static SHG intensity in the respective polarization channel.

## 7.8 Supplementary material

### 7.8.1 Electromagnons in CuBr<sub>2</sub>

The observed co-existence of spiral magnetic order and ferroelectricity is due to the spin-orbit coupling enabled interaction term between the spins  $\vec{S}$  and the electronic polarization  $\vec{P}$  [? ]:

$$H_{s-P} = \lambda \sum_i \vec{P}_i \cdot (\hat{x} \times \vec{S}_i \times \vec{S}_{i+1}) \quad (7.3)$$

The ordered state for  $T < T_N$  is a multiferroic with spontaneous polarization

$$\langle \vec{P}_i \rangle = P_0 \hat{y} \quad (7.4)$$

and spiral spin ordering

$$\langle \vec{S}_i \rangle \equiv \vec{S}_{0,i} = S_0 \left( \cos(\vec{Q} \cdot \vec{R}_i) \hat{x} + \sin(\vec{Q} \cdot \vec{R}_i) \hat{y} \right), \quad (7.5)$$

where  $\vec{Q}$  is the spin-ordering wavevector and  $\vec{R}_i$  are the spatial coordinates of the Cu atoms. Let us consider fluctuations about this ordered state and ask which fluctuations are detectable via SHG. Representing fluctuations in the polarization by  $\delta \vec{P}_i$  and spin by  $\delta \vec{S}_i$ , we get the following fluctuation Hamiltonian:

$$H_{s-P}^f = \lambda \sum_i \delta \vec{P}_i \cdot (\hat{x} \times \delta \vec{S}_i \times \vec{S}_{0,i+1} + \hat{x} \times \vec{S}_{0,i} \times \delta \vec{S}_{i+1}) + \mathcal{O}(\delta \vec{P}^2, \delta \vec{S}^2). \quad (7.6)$$

Expanding the spin fluctuations along all directions, we find that they couple only to polarization fluctuations along  $\hat{y}$  and  $\hat{z}$ . Focusing on zero-momentum polarization fluctuations (since they are sensitive to SHG),

$$\begin{aligned} H_{s-P}^f = & i \sin(\vec{Q} \cdot \vec{a}) \delta P_z(\vec{q} = 0) \left( \delta S_z(-\vec{Q}) - \delta S_z(\vec{Q}) \right) \\ & + \sin(\vec{Q} \cdot \vec{a}) \delta P_y(\vec{q} = 0) \left( -\delta S_x(-\vec{Q}) + i \delta S_y(-\vec{Q}) - \delta S_x(\vec{Q}) - i \delta S_y(\vec{Q}) \right) \\ & + \mathcal{O}(\delta \vec{P}^2, \delta \vec{S}^2) \end{aligned} \quad (7.7)$$

where  $\vec{a}$  is the lattice vector along the chain. Transverse polarization fluctuations  $\delta P \sim \hat{z}$  couple to a uniform rotation of the spin-plane about the  $x$  axis. These are the electromagnons discussed in ? ]. The longitudinal fluctuations, on the other hand, couple to longitudinal fluctuations of the magnetization on each site.

### 7.8.2 Energy of the pseudo-Goldstone mode

An expression for the frequency of the pseudo-Goldstone mode in the presence of an easy-plane anisotropy is given by [? ] as

$$\omega_- = \sqrt{A(Q)B(Q)}, \quad (7.8)$$

where

$$A(q) = 2S \left[ \frac{2J(Q) - J(Q+q) - J(Q-q)}{2} \right], \quad (7.9)$$

$$B(q) = 2S [J(Q) - J(q) + D], \quad (7.10)$$

$$J(q) = 2 [J_1 \cos(qa) + J_2 \cos(2qa)], \quad (7.11)$$

$D$  is the anisotropy energy, and  $2S$  is the amplitude of the spin in units of  $\mu_B$ .

Using  $Q = 0.235 \text{ rlu}$ ,  $J_1 = 8.8 \text{ meV}$ ,  $J_2 = -22.2 \text{ meV}$ ,  $D = 0.15 \text{ meV/Cu}$ , and  $2S = 0.38$ , we have

$$\omega_- = 1.3 \text{ meV} \quad (7.12)$$

in good agreement with the experiment.

### 7.8.3 Fits of time domain signals

Time-domain plots corresponding to the frequencies in Fig. 7.4 are illustrated in Fig. 7.5. Each plot is a least-squares fit of the data to a damped harmonic oscillator model

$$I_p^{\text{SHG}}(t, \theta) = P_p^0 \delta P_p(t, \theta) + [\delta P_p(t)]^2, \quad (7.13)$$

where

$$\delta P_p = A_p e^{-\gamma_p t} \cos \left( \sqrt{(2\pi\nu_p)^2 - \gamma_p^2} t + \psi_p \right), \quad (7.14)$$

$p \in \{P_{\text{in}} S_{\text{out}}, S_{\text{in}} S_{\text{out}}\}$ , and  $\theta$  denotes the set of free parameters to be estimated.

The main conclusion of these fits is that the frequency of the two modes (most notably, the low-frequency  $S_{\text{in}} S_{\text{out}}$  mode) soften on approaching  $T_c$ . This may also be seen heuristically from the time-domain signals without doing any fits. Fig. 7.6 shows an enlarged (i.e., scaled to account for the

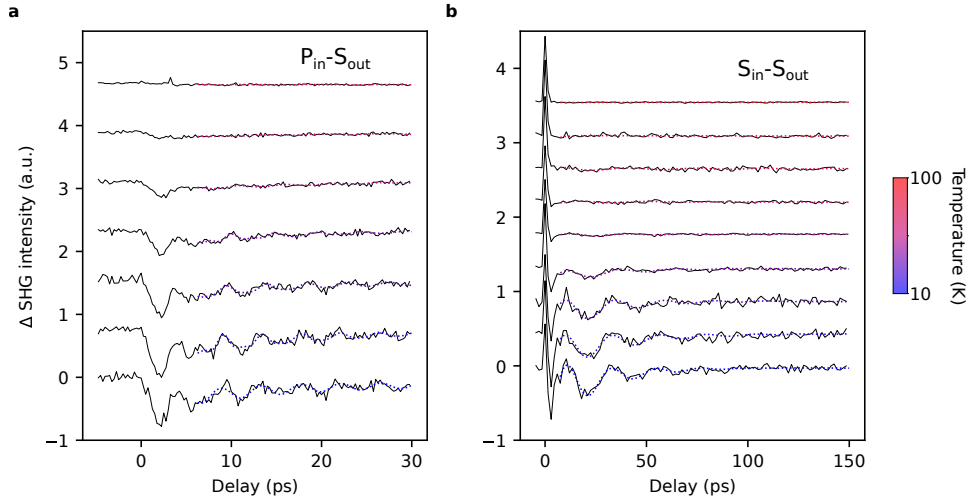


Figure 7.5: Time-domain signals corresponding to (a) Fig. 7.4(a) and (b) Fig. 7.4(b). Dashed lines depict least-squares fits to the data in a damped harmonic oscillator model, see Supplementary material, Section 7.8.3.

decrease in signal amplitude) view of the  $S_{in}S_{out}$  signal for three temperatures below  $T_c$ , showing a clear decrease in the oscillation frequency at high temperature. Fig. 7.7 shows an alternative fit where the frequency parameter  $\nu_{SS}$  is constrained to be constant as a function of temperature, showing that our data is not consistent with a hypothetical model where the frequency shift with temperature in Eq. 7.14 is only attributed to the damping term  $\gamma_{SS}$ .

#### 7.8.4 Error bars in Fig. 7.4

In this section, we describe how the uncertainties in the least square estimates of the frequency parameter  $\nu$  of Eq. 7.14, which are depicted as a function of temperature in Fig. 7.4, were calculated from the time-domain signals in Fig. 7.5. For each temperature and polarization channel, a LM algorithm was used to find the minimum  $\theta_0$  of the objective

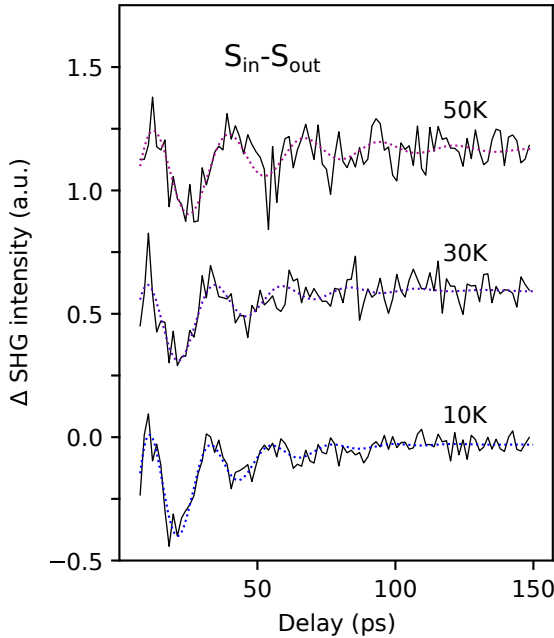


Figure 7.6: Rescaled  $S_{\text{in}}S_{\text{out}}$  time-domain signals (see Fig. 7.5(b)) for select temperatures below  $T_c$ .

function

$$f_p(\theta) \propto \sum_{n=0}^{N-1} (I_p^{\text{SHG}}(t_n, \theta) - I_{p,n}^{\text{SHG}})^2, \quad (7.15)$$

where  $\{(t_n, I_{p,n}^{\text{SHG}}), n \in (0, 1, \dots, N-1)\}$  are the data points in Fig. 7.5, and we have assumed the noise level is independent of delay. The uncertainty in each parameter is estimated within a parametric bootstrap[?]: for each temperature, 1000 bootstrap samples are generated by adding noise (normally distributed, with variance given by the variance of data points at long times where the signal is constant) to the LM estimate  $I_p^{\text{SHG}}(t_n, \theta_0)$ . For each bootstrap sample  $s$ , an estimate  $\theta_s$  is computed by minimizing Eq. 7.15 as above, and the 95 % confidence interval reported in Fig. 7.4 is taken to be 1.96 times the standard deviation of the distribution  $\{\theta_s - \theta_0\}$ .

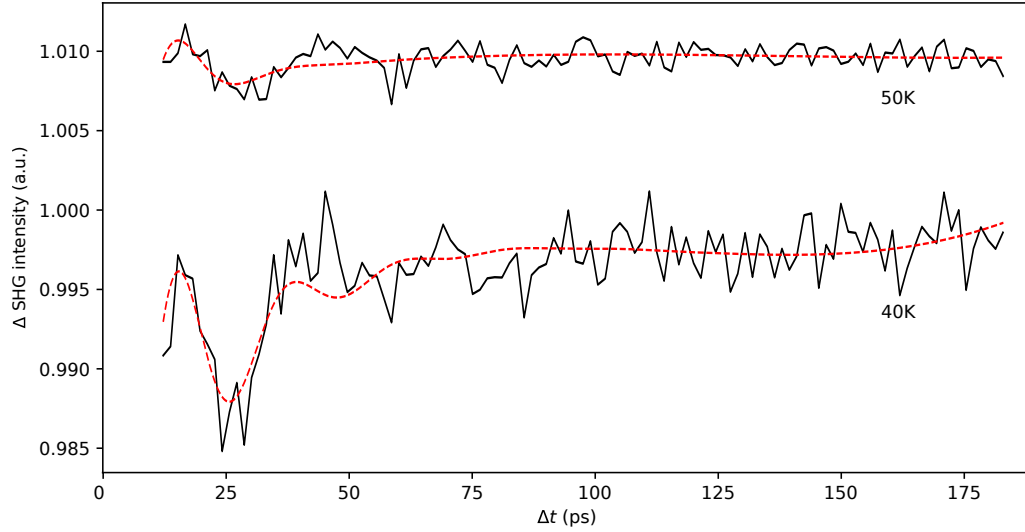


Figure 7.7:  $S_{\text{in}}S_{\text{out}}$  time-domain signals (see Fig. 7.5(b)) for select temperatures approaching  $T_c$ . Dashed lines depict least-squares fits to the data in a variant of Eq. 7.14 where  $\nu_{\text{SS}}$  is constrained not to vary with temperature.

### 7.8.5 Fits to static RASHG data

The static SHG intensity was fit by Eq. 7.18. The susceptibility tensor was taken to be the form Eq. 7.19, plus an additional  $C_1$  component (likely due to surface adsorbates). The result is shown in Fig. 7.8.

### 7.8.6 Excluded possibilities for observed results

#### 7.8.6.1 $\delta \vec{P} \parallel \hat{x}$ oscillation

Without loss of generality, let the maximum of the SHG in  $S_{\text{in}}P_{\text{out}}$  occur when the incoming electric field is along  $\hat{x}$ . Then, we have:

$$\Delta I_{\text{SP}}^{\text{SHG}} \propto |\hat{e}_i^{\text{out}} \chi_{ijkl} \hat{e}_j^{\text{in}} \hat{e}_k^{\text{in}} [P_{0l} + \delta P_l]|^2 - |\hat{e}_i^{\text{out}} \chi_{ijkl} \hat{e}_j^{\text{in}} \hat{e}_k^{\text{in}} P_{0l}|^2 \quad (7.16)$$

with  $\hat{e}_i^{\text{in}} \parallel x$  and  $P_{0l} \parallel y$ , we have

$$\Delta I_{\text{SHG}} \propto 2\hat{e}_i^{\text{out}} \hat{e}_j^{\text{out}} \chi_{ixxy} \chi_{jxxx} P_{0y} \delta P_x + \hat{e}_i^{\text{out}} \hat{e}_j^{\text{out}} \chi_{ixxx} \chi_{jxxx} \delta P_x \delta P_x \quad (7.17)$$

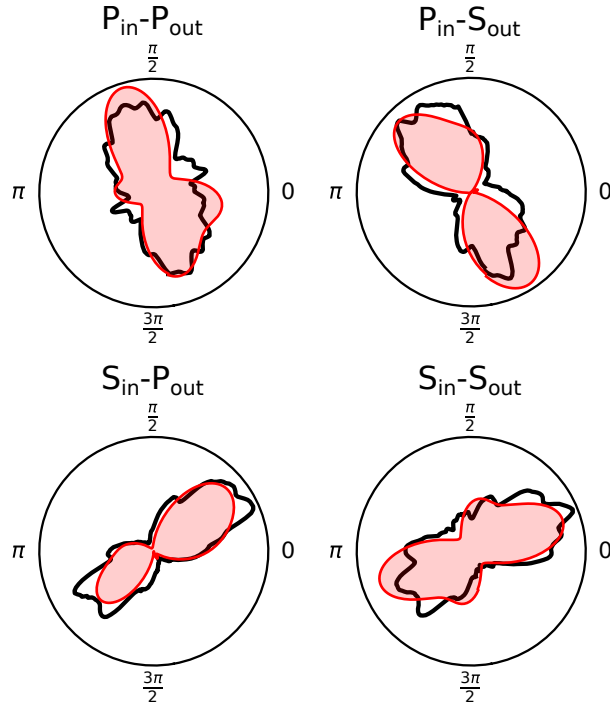


Figure 7.8: Fits (red) to static RA-SHG data (black) depicted in Fig. 7.3.

Since we are in  $S_{in}P_{out}$ ,  $\hat{e}_i^{out} \perp x$ ; thus, Eq. 7.17 involves the tensor elements  $\chi_{yxxx}$  and  $\chi_{xxxx}$ . Both of these elements are zero due to the  $x \rightarrow -x$  mirror symmetry. Thus, the  $\delta\vec{P}||\hat{x}$  oscillation is not visible in our experiment.

Additionally, since the  $\delta\vec{P}||\hat{x}$  mode does not couple to the spin order in this compound[?], its frequency should be far above the frequencies observed in our experiment (which are determined by the energy scales of the spin Hamiltonian).

### 7.8.6.2 Zone-folded acoustic phonons

Phonon band structure calculations were carried out using the finite displacement method[?] with a distance of 0.01 Å within a  $3 \times 3 \times 3$  supercell. Forces were calculated via the DFT-D2 method[?] and LDA+U method[?] ( $U_{Cu} = 3$  eV) using a  $7 \times 7 \times 5$   $k$ -mesh with 122 irreducible  $k$ -points and a plane-wave cutoff energy of 100 eV. The result is shown in Fig. 7.9. The acoustic phonons in Fig. 7.9 all disperse too rapidly for the

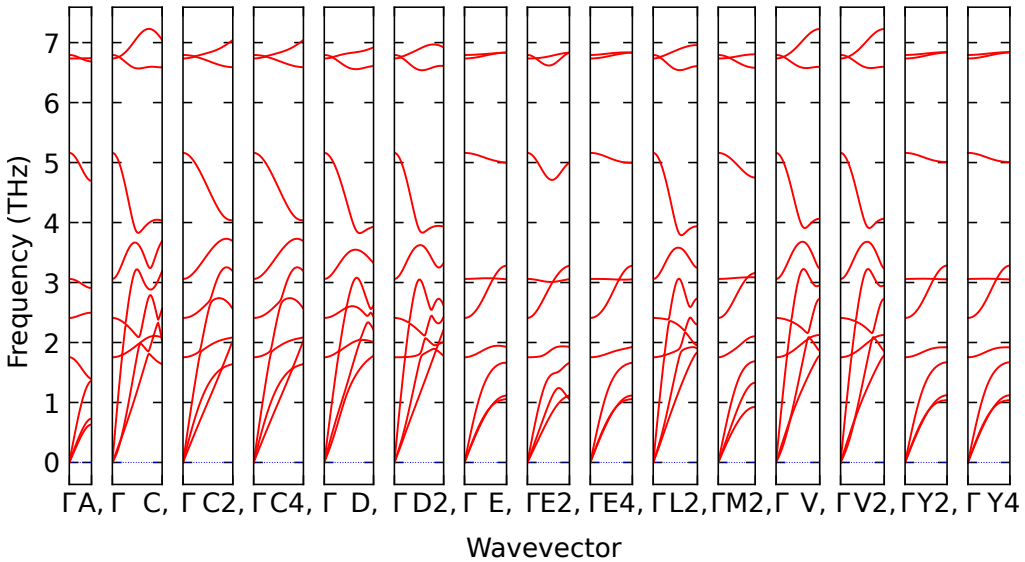


Figure 7.9: Phonon band structure of CuBr<sub>2</sub> within a finite displacement calculation.

0.05 THz oscillation in the tr-SHG to be consistent with a zone-folded (at  $k = (0, 0.235, 0.5)$ ) acoustic phonon.

#### 7.8.6.3 Magnetic SHG

In principle, magnetic systems with broken inversion symmetry may generate electric-dipole SHG with or without a static electric dipole moment. In this section, we wish to show that this is not the case in CuBr<sub>2</sub>; i.e., in CuBr<sub>2</sub>, the SHG intensity is a direct measure of the macroscopic electric dipole moment.

Indeed, in the presence of such a static electric dipole moment  $\vec{P}_0$ , we typically expect the SHG response to be directly proportional to it; i.e.

$$I(2\omega) \propto |\hat{e}_i^{\text{out}} \chi_{ijk} \hat{e}_j^{\text{in}} \hat{e}_k^{\text{in}}|^2, \quad (7.18)$$

where

$$\chi_{ijk} = \chi_{ijkl} P_{0l}, \quad (7.19)$$

and  $\hat{e}^{\text{in}}, \hat{e}^{\text{out}}$  are unit vectors in the direction of the incoming and outgoing

electric fields, respectively. In CuBr<sub>2</sub>, we have

$$\vec{P}_0 = \sum_{\langle i,j \rangle} \hat{x} \times \vec{S}_i \times \vec{S}_j, \quad (7.20)$$

i.e., the static polarization is quadratic in the spin degree of freedom.

The question, then, is whether there exists some additional term

$$\chi'_{ijk} = \chi_{ijkl} G_{0l}, \quad (7.21)$$

where  $\vec{G}_0$  is either (a) linear in spin, or (b) quadratic in the spins but not of the form  $\sum_{\langle ij \rangle} \vec{S}_i \times \vec{S}_j$ . For case (b), note that the term  $\sum_{\langle ij \rangle} \vec{S}_i \times \vec{S}_j$  is the only quadratic form which is simultaneously antisymmetric in the bond direction and  $\vec{q} = 0$  (i.e. each bond has the same coefficient).

For case (a), we argue here that any such term is weak due to the approximate time-reversal symmetry of the spiral magnetic order. Consider first a four-site commensurate approximant of the incommensurate spin spiral. This phase has a symmetry element consisting of the time-reversal operation followed by a translation by half of the magnetic supercell. Thus, the point group contains time-reversal symmetry. Since  $\vec{G}_0$  is linear in spin, time-reversal takes  $\vec{G}_0 \rightarrow -\vec{G}_0$ ; but since time-reversal is a symmetry, it must also take  $\chi'_{ijk} \rightarrow \chi'_{ijk}$  and  $\chi_{ijkl} \rightarrow \chi_{ijkl}$ . Thus,  $\chi'_{ijk} = 0$  in the commensurate approximation.

In the incommensurate case, note that the magnetic point group of an incommensurate magnetic phase is defined as the set of point-group operations present in the operations belonging to the superspace group. Thus, for a single-k incommensurate magnetic structure, time-reversal is always an element of the magnetic point group. This is due to the fact that the lattice constant in the chain direction is 3.51 Å, so lengthscales associated with translations in the space group are much smaller than the probe wavelength ( $\sim 800$  nm). The symmetry group “seen” by the probe thus contains time reversal to a very good approximation.

#### 7.8.6.4 Multi-phason excitation

While the amplitude mode of the spin spiral in CuBr<sub>2</sub> is the only single-particle excitation which couples to  $\delta P_y$  (see Eq. 7.7), in principle multiparticle excitations consisting of, e.g., two phasons with opposite momenta are also allowed. However, note that the relevant energy scale which

defines the phason sound velocity depends on the intra-chain coupling terms, which are  $\mathcal{O}(10\text{ meV})$ ; the peak in the phason joint density of states thus occurs at this high energy scale, which is much larger than the 0.2 meV energy of our low-frequency oscillation. Multi-phason excitations are thus not consistent with the long-lived oscillation observed in our experiment.

## Chapter 8

---

### *Concluding remarks*

We began this thesis by discussing how strong interactions may invalidate the Fermi liquid model and result in novel quantum ground states which are not possible to understand within a single-particle picture. The result is a situation where there is no general theory at present capable of predicting, *a priori*, the ground state and low-energy excitations of an arbitrary correlated quantum material. We have obviously not come any closer to such a theory over the course of this research—although, in truth, that was never really the goal. What we have done instead is to enlarge our inventory of novel phenomena which can occur in quantum materials (acknowledging, of course, that specifying such an inventory is essential for solving the correlated electron problem), and in this sense we have met some success. Using a novel experimental technique (tr-SHG), we showed that antiferromagnets may be manipulated nonthermally by quenching the equilibrium order on ultrafast timescales, in a fashion which is similar in spirit to previous works on CDW systems [? ? ]. We also showed that spin-spiral multiferroic materials may host novel electromagnon excitations which are due not to the pseudo-Goldstone mode, but to the amplitude mode of the magnetic order. Both of these discoveries were quite unexpected, and each of them *required* measuring the full RA-SHG signal at each time delay—a technology that was developed (partially by us) only over the course of the last 10–15 years. The story, then, is that a new technique was developed, and then that technique led us to new physics that we didn’t previously know existed.

This story is quite common in condensed matter physics. Consider, for example, the discovery of antiferromagnetism, which is no doubt more common in solids than ferromagnetism. Nevertheless, ferromagnetism induces a net magnetic dipole moment, and the resulting macroscopic magnetic properties are thought to have been understood by humans as early as the fourth millennium B.C. [? ]. Antiferromagnets, in contrast, took

until the 20<sup>th</sup> century to be predicted [? ] and experimentally discovered [? ]—the latter required the development of neutron scattering. Thus, new techniques which are sensitive to different order parameters or excitations very often lead to new discoveries in condensed matter physics.

In light of this history, in my view there is no reason to think that the technology we have at present is sufficient to solve the correlated electron problem. This is a perspective which is often voiced in the context of  $\text{URu}_2\text{Si}_2$ , a heavy-fermion material with a phase transition at 17.5 K to an ordered state whose order parameter and low-energy excitations remain unknown despite nearly thirty years of investigation [? ]. It is thought [? ] that the puzzle has remained unsolved simply because we do not, at present, have an experimental probe which couples to the order in this compound. Going forward, I thus predict that technique development will be the fundamental driving force for progress in strongly correlated electron physics. A large part of this will involve *improving* techniques that we already have (using, for example, machine learning, or 4<sup>th</sup>-generation synchrotron sources) to increase signal-to-noise, ease of data processing, etc. A parallel effort will be to imagine totally different experimental probes (such as, for example, scattering of entangled particles[? ]), although this is obviously more difficult.

There is potentially some criticism to be made of the *approach* we take to the correlated electron problem in present era of modern science. At the time of writing, a large portion of the research which is published in high-impact factor journals in this field is of the type pursued in this thesis—systematic research is largely *avoided* in favor of surprising or unexpected results, which are, in the most pessimistic view, easier for journals to shape into a headline. My feelings on this issue are somewhat mixed. In the worst case, the current research climate deters researchers from pursuing systematic research, on the basis that it is more difficult to publish. At the same time, the field is still somewhat in its infancy, and I do think that there are a large number of fundamental phenomena in quantum materials that simply have yet to be discovered. Perhaps, then, the right research to be doing is indeed more exploratory right now than would otherwise feel comfortable.

In either case, I am sure that there is *absolutely no reason* to be publishing in for-profit journals! Perhaps this would be understandable if the for-profit journals offered a monetary incentive to authors who elect to publish there. But the reality is the opposite—in the publishing industry,

the *suppliers* pay for the goods that they provide, and then pay again to consume those goods. This bizarre circumstance is possible only because of a valuation heuristic (which occurs at all levels of academic discourse—from faculty hiring decisions to grad lounge chit-chat) that ranks papers on the basis of which journal they are published in. This results in a situation where the publishing industry itself holds all of the power in directing what scientists decide to study; thus the conventional wisdom that one should avoid manganites and cuprates since these are not of interest to editors of high-impact factor journals. This is, in my opinion, the biggest impediment to progress right now in correlated electron physics.

One immediate solution would be the adoption of, for example, a “journal of null or uninteresting results”, where authors could receive citations for research which is not flashy but may nevertheless be useful. In the long term, however, the field must transition away from the for-profit publication industry, which may involve the difficult task of redefining our research valuation methodology. To some extent I think this is already happening; many of the graduate students and postdocs I talk to share a similar point of view, and after all, those are the people that will eventually be making decisions about who gets tenure at academic institutions.

In any case, the idea that the correlated electron problem is important—something which I hope to have reinforced through the research conducted in this thesis—is certainly not something that will go away. There is thus a bright future ahead for this field, and I am quite confident in the condensed matter community to help make that future a reality.



---

*Bibliography*